Dynamics of nanoscale systems probed by time-resolved STM-induced luminescence

Thèse N° 9325

Présentée le 4 juin 2019

à la Faculté des sciences de base
Laboratoire de science à l’échelle nanométrique
Programme doctoral en physique

pour l’obtention du grade de Docteur ès Sciences

par

Anna Maria ROSŁAWSKA

Acceptée sur proposition du jury

Prof. O. Schneider, président du jury
Prof. K. Kern, directeur de thèse
Prof. E. Meyer, rapporteur
Prof. S. Loth, rapporteur
Prof. M. Chergui, rapporteur

2019

ÉCOLE POLYTECHNIQUE
FÉDÉRALE DE LAUSANNE

Inspiration is not the exclusive privilege of poets or artists generally. There is, has been, and will always be a certain group of people whom inspiration visits. It's made up of all those who've consciously chosen their calling and do their job with love and imagination. It may include doctors, teachers, gardeners – and I could list a hundred more professions. Their work becomes one continuous adventure as long as they manage to keep discovering new challenges in it. Difficulties and setbacks never quell their curiosity. A swarm of new questions emerges from every problem they solve. Whatever inspiration is, it's born from a continuous "I don't know."

— Wisława Szymborska, Nobel Lecture, 1996

Abstract

The efficiency and peculiarities of processes such as surface adsorption or electron-to-photon energy conversion in organic and inorganic structures are determined by the dynamics at the scale of individual molecules, atoms and charges. The timescales of such effects reach down to the ps regime, which can be routinely probed using ultrafast optics methods. However, these far-field techniques suffer from ensemble-averaging that obscures the information encoded at the atomic level. These limits can be overcome by combining scanning tunnelling microscopy (STM) with time-resolved light detection so that pm and ps scales can be reached simultaneously. STM-induced luminescence (STML) methodologies are employed in this thesis to explore the nanoscale dynamics of different systems: light emitting defects in C_{60} thin films, H_2 molecules weakly physisorbed on Au(111), metal-metal tunnel junctions and single atom contacts.

First, we study the dynamics associated with the radiative decay of single excitons at defect-related emission centres localized in the C_{60} molecular film. Such emission centres serve as the smallest possible model of an organic light emitting diode where a single electron and hole recombine producing a photon. Using time-resolved STML (TR-STML) excited by voltage pulses, we follow the formation of an individual exciton and map this process in real space with ns resolution. Besides the excitonic emission, on C_{60} thin films we observe luminescence due to the radiative decay of plasmons. We study the interplay of these two processes and create a nanoscale bimodal source whose emission can be dynamically tuned by controlling the charge injection rate. A kinetic model is employed to thoroughly describe the charge and exciton dynamics in this system.

The developed kinetic model can be also used to analyse the motion of hydrogen molecules adsorbed on an Au(111) crystal. The weak interaction with the metal and the continuous charge injection by the tip leads to recurrent excursions of the molecule inside and outside from the tunnelling junction, which chop the plasmonic luminescence intensity. These dynamical changes in the light intensity can be followed by correlation spectroscopy and allow extraction of the molecule's residence and excursion times.

In the next step, we probe the dynamics of a generic metal-metal tunnel junction. Interestingly, when a high bias is applied, the emission from the junction exhibits photon bunching on a time scale below 50 ps as evidenced by Hanbury Brown-Twiss interferometry. Such a process is a result of a distribution of the energy of one electron between two photons, which may possibly be entangled. The opposite process may occur as well, under conditions where two electrons interact supplying energy to one photon. This overbias emission is a feature of single atom contacts and is used here to probe the fluctuations of plasmonic enhancement driven by the motion of single atoms in the vicinity of such a contact.

Keywords: STM-induced luminescence, time-resolved STM, nanoscale dynamics, C_{60}, hydrogen, tunnel junction, single atom contacts, plasmonics, plasmonic enhancement, photon correlations, photon bunching

Zusammenfassung

Effizienz und Besonderheiten von Prozessen, wie der Adsorption auf Oberflächen oder dem Energieübertrag zwischen Elektronen und Photonen in organischen und inorganischen Strukturen, werden von der Dynamik einzelner Moleküle, Atome und Ladungen bestimmt. Die Zeitskalen solcher Prozesse reichen bis hinunter in den Pikosekundenbereich, für dessen Untersuchung sich ultraschnelle optische Methoden etabliert haben. Solche Fernfeldmethoden leiden jedoch darunter, dass sie über Ensembles mitteln und damit die von der atomaren Ebene stammende Information abschwächen. Diese Einschränkung kann überwunden werden indem man Rastertunnelmikroskopie (STM) mit zeitaufgelöster Lichtdetektion kombiniert, so dass gleichzeitig Pikometer- und Pikosekundenskalen erreichbar sind. In dieser Doktorarbeit wird mittels Rastertunnelmikroskopie erzeugte Lumineszenz (STML) eingesetzt um die Dynamik verschiedener Systeme auf der Nanoskala zu erforschen: leuchtende Defekte in dünnen C_{60}-Filmen, schwach physisorbierte Moleküle auf Au(111), Tunnelkontakte zwischen Metallen sowie Einzelatomkontakte.

Zuerst untersuchen wir die Emissionsdynamik einzelner Exzitonen an defektinduzierten Emissionszentren eines C_{60}-Molekülfilms. Solche Emissionszentren dienen als kleinstmögliches Modell einer organischen Leuchtdiode, in der ein einzelnes Elektron und ein Loch unter Abstrahlung eines Photons rekombinieren. Mit zeitaufgelöstem STML (TR-STML) verfolgen wir die durch Spannungspulse hervorgerufene Bildung einzelner Exzitonen und erhalten Bilder von der Oberfläche, die den Prozess mit Nanosekundenauflösung zeigen. Neben der exzitonischen Emission von C_{60}-Filmen beobachten wir auch Lumineszenz von zerfallenden Plasmonen. Wir untersuchen den Zusammenhang dieser beiden Lumineszenzprozesse indem wir eine kombinierte Lichtquelle erzeugen, deren Emission dynamisch über die Ladungsinjektionsrate verändert werden kann. Ladungs- und Exzitonendynamik werden dabei vollständig mit einem kinetischen Modell beschrieben.

Mit dem entwickelten kinetische Modell kann auch die Bewegung von Wasserstoffmolekülen auf einem Au(111)-Kristall analysiert werden. Die schwache Wechselwirkung mit dem Metall und die andauernde Ladungsinjektion der Spitze führen dazu, dass die Moleküle wiederholt den Tunnelkontakt verlassen und somit die plasmonische Lumineszenz zerhackt wird. Die variierende Lichtintensität kann mittels Korrelationsspektroskopie aufgezeichnet werden, so dass die Verweilzeit des Moleküls im Kontakt und die Dauer seiner Abwesenheit abgeleitet werden können.

Im nächsten Schritt untersuchen wir den Emissionsvorgang in einem unspezifischen Kontakt zwischen zwei Metallen. Wie Hanbury-Brown Twiss Interferometrie zeigt, werden Photonen interessanterweise in Gruppen mit weniger als 50 Pikosekunden Länge abgestrahlt (Photon-Bunching) sobald eine erhöhte Spannung an den Kontakt gelegt wird. Diese Tatsache resultiert aus der Aufteilung der Elektronenenergie auf zwei Photonen, die möglicherweise untereinander verschränkt sind. Unter Bedingungen, unter denen zwei Elektronen wechselwirken und ihre Energie an ein einziges Photon übertragen, tritt auch der umgekehrte Vorgang auf. In dem Fall liegt die Emissionsenergie oberhalb der an den Kontakt angelegten Potentialdifferenz. Wir benutzen den Mechanismus in dieser Arbeit um Fluktuationen der plasmonischen Verstärkung zu untersuchen, die von der Bewegung einzelner Atome nahe des Kontakts verursacht werden.

Stichwörter: durch Rastertunnelmikroskopie erzeugte Lumineszenz, zeitaufgelöste STM, Dynamik im Nanobereich, C_{60}, Wasserstoff, Tunnelkontakte, Einzelatomkontakte, Plasmon, plasmonische Verstärkung, Photonen-Korrelationen, Photon-Bunching

Contents

List of Figures

List of Acronyms

AFM	Atomic Force Microscopy
AIMD	*ab initio* molecular dynamics
AWG	arbitrary wave generator
CCD	charge-coupled device
DFT	density functional theory
DOS	density of states
FER	field emission resonance
FIFO	first-in first-out
FWHM	full width at half-maximum
HBT	Hanbury Brown-Twiss
HOMO	highest occupied molecular orbital
LHe	liquid helium
LN_2	liquid nitrogen
LUMO	lowest unoccupied molecular orbital
MCBJ	mechanically controlled break junction
ML	monolayer
NMR	nuclear magnetic resonance
OLED	organic light emitting diode
SERS	surface-enhanced Raman spectroscopy
SPAD	single-photon avalanche photodiode
SPM	Scanning Probe Microscopy
STM	Scanning Tunnelling Microscopy
STML	STM-induced luminescence
STS	scanning tunnelling spectroscopy
TCSPC	time-correlated single photon counting
TERS	tip-enhanced Raman spectroscopy
TIBB	tip-induced band bending
TIP	tip-induced plasmon
TR-STML	time-resolved STML
UHV	ultra-high vacuum

1 Introduction

Motion is one of the most fundamental concepts of physics. It can be seen not only as a change of a position of an object over time but also be perceived in a more general way: an evolution of the configuration of a physical system. In this broader perspective, apart from considering the motion of atoms or galaxies, the propagation of a wave or an evolution of quantum states can be studied. Laws that describe this time-dependent configuration of the system constitute *dynamics*.

Dynamics of the processes and objects reachable by a human eye is studied since ancient times. Studies of smaller objects have been enabled only along with the invention of the optical microscope. One of the remarkable achievements of early optical microscopy is the discovery of the random Brownian motion [1], which can be followed in the sub-second time scale. Going even further towards processes occurring on smaller and smaller scales with optical microscopy, one reaches the dynamics of movable proteins (kinesin, myosin) [2, 3], growth of nanoparticle monolayers [4], quantum emitters [5] or luminescence from organic materials [6]. In terms of time-resolution, optical methods have developed so far that the dynamics can be studied on the scale of few tens of *attoseconds* [7–9], constituting an improvement over 16 orders of magnitude as compared to the original Brown's experiments.

Importantly, the optics-based methods suffer from a fundamental constraint - the diffraction limit, which states that two objects cannot be resolved if their separation is less than half of the wavelength used to image them. This limit can be overcome using super-resolution microscopy, however only objects as big as few tens of nm can be resolved using these methods [10]. Therefore, the excellent time-resolution provided by laser-based spectroscopies can be employed only for low-resolution studies that inherently are spatial-averaging and lose the critical information related to molecular and atomic structure.

One of the workarounds to this problem is the usage of an electron beam with the wavelength on the order of a few pm as in the transmission electron microscopy (TEM), which enables imaging with atomic resolution [11]. Efforts to combine it with ultrafast optics are in progress, however, the atomic resolution is not yet reached [12]. Additionally, the high energy beam destroys molecules, limiting the materials that can be studied [13].

On the contrary, scanning tunnelling microscopy (STM) enables studies of surfaces with atomic resolution and is not limited to inorganic systems, but organic or even biological samples can be investigated [14, 15]. Although the intrinsic time-resolution is defined by the current amplifier, which restricts it to the sub-ms regime, this limit can be circumvented by either electrical or optical means to study atomic-scale dynamics down to the sub-ps resolution [16–20]. One of the methods reaching ps dynamics is STM-induced luminescence (STML), which is based on local luminescence excitation and plasmonic enhancement, such that the light emission from a single molecule can be studied [21, 22]. Its time-resolution is defined by the state-of-the-art detectors (ps regime) [23]. Time-resolved STML constitutes the core of this thesis.

Such a tool provides access to a variety of dynamical processes taking place at the nanoscale, with the most evident one being the motion of atoms and molecules. This fundamental transport of mass plays a crucial role in heterogeneous catalysis, adsorption and desorption properties [24] or the plasmonic enhancement of spectroscopic signals [25]. In the simplest case, a Brownian random walk is expected. However, it is the directed motion that is more fascinating, because it offers the perspective of being manipulated. Such control requires a proper understanding of the fundamental processes driving the motion of single atoms and molecules. Having done that, it is possible to design devices and systems that can, for example, guide the reactant into the place where the reaction efficiency is the highest.

The intrinsic strength of STML is the direct access to the electron-to-photon conversion efficiency at the ultimate scale. Probing the fundamental laws driving these processes is key for the optimization of modern optoelectronic devices, such as organic light emitting diodes (OLEDs), which play an essential role in everyday life. Their principle of operation is based on radiative recombination of electron-hole pairs (excitons) that are created in an organic thin film. So far, the dynamics of OLED electroluminescence, which is driven by the motion of individual charges and diffusion of excitons have been studied only in ensemble measurements [26] calling for time-resolved studies at the smallest possible device: an individual molecular emitter. This is a possibility that STML offers.

Electron-to-photon energy conversion is critical also for sophisticated light sources that are based on the time-dependent interactions within a quantum system. One possible structure comprises molecular emitters interacting with the neighbouring metallic architectures characterized by their plasmonic modes [27]. Even more advanced light sources and their applications are based on purely quantum mechanical interactions, which occur on ultrashort time-scales, such as single photon emission and formation of entangled photon pairs.

This thesis explores these three aspects of dynamics at the nanoscale: the motion of mass or charge and time-dependent interactions within a quantum system. Chapter 2 briefly reviews the research field and describes the instrumentation necessary for studies of time-resolved light emission with atomic precision. Chapter 3 presents the theoretical basis for the analysis of time-dependent processes at the nanoscale. This modelling scheme is used in Chapters 4 and 5, which present studies on C_{60} thin films. In this system, we probe the formation of an individual exciton in four nanosecond-nanometre dimensions and dynamically control the ratio of excitonic and plasmonic light (*i. e.* its colour). In Chapter 6 we continue employing the toolbox from Chapter 3 and show studies of motion of a single hydrogen molecule on a Au(111) surface. In Chapter 7 we report on a non-linear process in which one electron distributes its energy to two photons emitted as a possibly entangled pair within less than 50 ps. Chapter 8 discusses another non-linearity relying on the interaction between two electrons that leads to an emission of a photon. We employ this effect to study the motion of single atoms in the vicinity of a single atom contact.

2 Principles of STM and STM-induced luminescence (STML)

2.1 Scanning tunnelling microscopy

The concept of using a local probe to investigate surfaces beyond the possibilities offered by the optical microscopy was introduced for the first time by Young, Ward and Scire in the early 1970s [28], when the authors presented a successful realization of a device they called *The Topografiner.* It operated in the field emission regime and was capable of imaging surfaces with lateral resolution down to 400 nm and vertical down to 3 nm, which was approaching but did not yet reach the atomic scale. This ultimate goal was achieved in the next decade along with the invention of a Scanning Tunnelling Microscope (STM) [29, 30], which earned G. Binnig and H. Rohrer the Nobel Prize in Physics in 1986[1].

The development of STM and the subsequent construction of an Atomic Force Microscope (AFM) allowed routine imaging of surfaces with atomic resolution and revealing chemical bonds within an individual molecule [31, 32]. Importantly, Scanning Probe Microscopies (SPMs) should not only be viewed as imaging tools but as powerful methodologies allowing manipulation [33, 34] and investigation of fundamental processes at the atomic scale. Such studies include: magnetism [35–38], chemical reactions [39–41], catalysis [42, 43], friction [44, 45] as well as luminescence and dynamics. The latter ones will be the main scope of this thesis and will be reviewed in Sections 2.2 and 2.3, after a brief introduction of the basic STM concepts. For a more extended discussion about the STM fundamentals, we refer the reader to the textbooks by Chen [46] and Voigtländer [47].

Quantum tunnelling

In classical physics, an object travelling towards a potential barrier of energy higher than the one of the object will not be able to penetrate the barrier, which will appear as a *wall.* However, in quantum physics, an object can penetrate such a *wall* in a phenomenon called tunnelling. Examples of its presence can be found outside physics laboratory and include nuclear fusion

---

[1] Together with E. Ruska for the construction of an electron microscope.

in the Sun [48], DNA mutations [49] or the common problem in the semiconducting industry - the leakage current [50].

The tunnelling process can be described by solving the one-dimensional Schrödinger equation with a potential barrier of height V. A particle of energy $E < V$ will have the following decaying wavefunction within the classically forbidden region:

$$\psi(z) = \psi(0)e^{-\kappa z} \tag{2.1}$$

with the decay constant $\kappa = \sqrt{2m(V-E)}/\hbar$, where m is the mass of the particle and $\hbar$ is the reduced Planck constant.

When a voltage bias is applied, the tunnelling current flows. For bias voltages that are small compared to the work function ϕ (which defines the barrier) the tunnelling will occur from states close to the Fermi energy of the electrode and the barrier height can be approximated as ϕ. The tunnelling current is then:

$$I \propto e^{-2\kappa z} \tag{2.2}$$

With the decay constant $\kappa = \sqrt{2m\phi}/\hbar$. Typical values of work functions for materials studied with STM are close to $\phi = 5$ eV. Thus $\kappa \approx 10\ nm^{-1}$ meaning that the tunnelling current changes by an order of magnitude when the distance between the electrodes changes by 1 Å. This value is reproduced in the experiment and the sensitivity of the current on the distance between the electrodes is crucial for the atomic resolution that STM offers.

STM working principle

The tunnelling junction of an STM comprises two elements: an extremely sharp metallic tip (preferably terminated with a single atom) and the investigated conducting sample. The tip is brought towards the surface using a piezoelectric motor and once the tunnelling regime is reached (< 1 nm from the sample) the tunnelling current can be detected. The surface is then raster scanned by the tip, which is usually located on a piezoelectric tube that allows positioning with pm precision. There are two main modes of scanning: constant current and constant height. In the former, the tunnelling current is kept constant by a feedback loop that changes the relative tip-sample distance, which is recorded as a function of the lateral position. In the latter mode, the feedback loop is disabled and the tunnelling current is recorded as a function of the position. In the everyday operation, the constant current mode is used, which provides safer operation because the risk of an accidental indentation with the tip into the sample is reduced as compared to the constant height mode (see the current dependence on the distance discussed above). Moreover, because of the extreme sensitivity of the STM, special care has to be taken to mechanically isolate the instrument from the environment.

Imaging and spectroscopy

The tunnelling problem can be treated by the means of time dependent perturbation theory, by applying Fermi's golden rule. Using Bardeen's approach the tunnelling current in the limit of low temperature can be written as [46, 51, 52]:

$$I = \frac{4\pi e}{\hbar} \int_0^{eV} \rho_A(E_F - eV + \epsilon)\rho_B(E_F + \epsilon)|M|^2 d\epsilon \tag{2.3}$$

where ρ_A and ρ_B are the density of states of both electrodes (A, B), E_F is the Fermi energy, V is the applied bias, and M are tunnelling matrix elements (depending on the wavefunctions of the electrodes). One has to note that this equation describes elastic tunnelling: a state in one electrode can tunnel only to a state in the other electrode that has the same energy. Inelastic tunnelling will be introduced in Section 2.2.

Assuming that the tunnelling matrix elements are independent of the bias, one obtains that the tunnelling current depends on the convolution of the densities of states of both tip and the sample, which is the basis of STM imaging. This concept was further expanded by Tersoff and Hamann [53] who modelled the tip wavefunction as spherically symmetric (s-wave) and were able to show that in this case, the tunnelling current depends only on the local density of states of the sample with the differential conductance described as:

$$\frac{dI}{dV} \propto \rho_{sample}(eV) \tag{2.4}$$

This dependence constitutes the principle of Scanning Tunnelling Spectroscopy (STS) as a probe of the local density of states. One has to note here that for a successful experiment the tip has to be prepared in such a way that its density of states is constant in the desired bias regime. Otherwise, artefacts are expected.

2.2 STM-induced luminescence

The history of STM-induced luminescence (STML) traces back to 1971 when the constructor of *The Topografiner*, R. Young, suggested that the photons emitted upon field emission from this device can be collected to produce an image [54]. 5 years before the first STM construction, Lambe and McCarthy [55] reported light emission from planar metal-insulator-metal tunnel junctions. This effect was explained in terms of surface plasmon mode excitation (and their subsequent radiative decay) by inelastic tunnelling. After the invention of the STM, the efforts devoted into developing a microscope with an optical detection system that resulted in the first observation of STML from polycrystalline tantalum and Si(111) surface as shown from IBM Zürich by Gimzewski *et al.* in 1988 [56]. Subsequent research focused on STML from metal and semiconductor surfaces, as well as organic adsorbate layers, which were reported by Berndt *et al.* [57–59].

Another breakthrough came in 2003 with the first observation of intrinsic emission from an insulated fluorescent molecule that was reported by Qiu, Nazin and Ho [21]. This experiment opened new avenues in STML research and enabled studies of fundamentally and technologically relevant organic molecules at the ultimate scale of one isolated emitter on a surface. Recent notable advances include single photon emission from defects [19] and individual molecules [60], dipole-dipole coupling [61] or resonant energy transfer [62] between two adjacent molecules, and luminescence from a molecular ion [63].

In general, there are two modes of emission observed in STML: plasmonic (*e. g.* from metals) and excitonic (*e. g.* from molecules), which will be briefly discussed in the following. For a more detailed overview of the field, an interested reader is referred to excellent reviews [22, 64–66] with the most recent one prepared by Kuhnke *et al.* [22].

2.2.1 Plasmonic electroluminescence

Plasmons are collective (quantized) oscillations of the electron density that occur at optical frequencies in metals. At the interface between the metal and dielectric (vacuum) they can interact with the electromagnetic field, which leads to surface plasmon polaritons (SPPs, also called surface plasmons SPs). As it can be shown by solving Maxwell equations, these modes propagate along the metal-dielectric interface and have an associated momentum that is higher than the free-space photons having the same energy. Therefore, for a radiative decay of an SPP to occur, this momentum mismatch has to be overcome, which can be achieved by the use of a prism, scattering from the imperfections of the surface or from a grating [22, 27, 66, 67].

These SPPs can be localized by introducing a metallic nanoparticle close to the metal-dielectric interface described above (and forming a nanocavity in this way). Such plasmonic modes are referred to as localized surface plasmons or, specifically to SPM, tip-induced plasmons (TIPs). For simplicity throughout this thesis, we will refer to TIPs as simply "plasmons". Plasmonic modes in an STM-like geometry (nanoparticle close to a flat surface) have been studied theoretically by Rendell *et al.* who showed that the broadband modes are highly localized in the narrowest constriction (right at the tip apex), the resulting dipole is aligned normal to the surface (defining the major polarization of the radiation) and that the maximum of emission intensity can be observed at approx. 60° to the surface normal [68, 69].

An important consequence of the presence of localized plasmons is the local electromagnetic field enhancement. Together with the intrinsic nature of the metallic STM tip that concentrates the electric field at its apex, we obtain an extremely strong lightning-rod effect [22, 27]. It enhances the near-to-far-field coupling (and reversed) setting the basics of nanooptics. One prominent example of an application of this effect is surface or tip-enhanced Raman spectroscopy (SERS, TERS), which are sensitive to a single molecule [70, 71]. The same en-

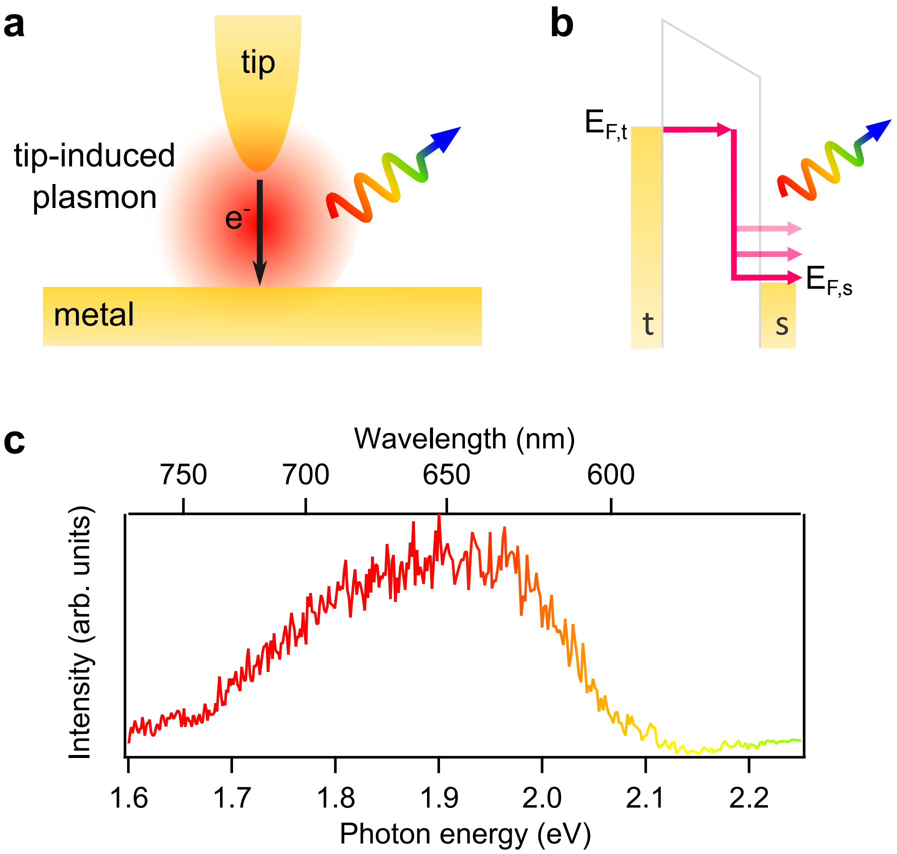

Figure 2.1 – Plasmonic electroluminescence. a) A scheme of a tunnel junction emitting light due to the radiative decay of plasmons. b) Energy diagram of the plasmon excitation due to inelastic tunnelling. c) Typical broadband spectrum of plasmonic electroluminescence of an Au-Au junction. The colour scale of the trace reflects the human visual perception of different photon energies.

hancement and high localization is utilized in STML and enables observing emission from an isolated molecule [21] as well as plasmonic decay with the resolution of few nm [72]. Additionally, the resolution is enhanced by the basic STM principle - atomically precise charge injection, which leads to highly localized light excitation [21, 73–76].

To profit the most from this enhancement, for both coupling the light in and out, the materials have to be chosen appropriately. The strongest plasmonic oscillations, and thus the enhancement, occur for noble metals, such as Ag, Au or Cu, because of low losses (a small imaginary component of the dielectric function) [77], which are thus the desired electrode materials to perform STML studies. Among these metals, Ag has the highest enhancement, Au and Cu exhibit 30 % and 10 % of Ag enhancement, respectively [77]. Au and Cu exhibit also interband transitions[2] that limit the plasmonic response for wavelengths shorter than 550 and 600 nm, respectively [27, 78].

---

[2] These transitions are also responsible for the colour of these metals.

The plasmonic modes in the STM junction are excited by the tunnelling current [3] (Fig. 2.1a). As mentioned earlier, apart from the elastic tunnelling described by eq. 2.3, inelastic tunnelling may occur. During such a process an electron within the potential barrier loses a fraction of its available energy eU defined by the applied bias U to vibrations of a molecule [79], a spin system [80] or a plasmon (Fig. 2.1b) [81]. The rate of this process can be defined similarly to elastic tunnelling by employing Fermi's golden rule:

$$\Gamma_{inel} = \frac{2\pi}{\hbar} \int_{E_F - eU + \hbar\omega}^{E_F} \rho_s(\epsilon + eU)\rho_t(\epsilon)|M_{inel}|^2 d\epsilon \tag{2.5}$$

which was evaluated by Persson and Baratoff [82]. The authors calculated the branching ratio between elastic and inelastic tunnelling and obtained that the plasmons are excited by less than 1 % of tunnelling electrons, which can then emit a photon with a probability close to 10 %. Therefore the total efficiency of the electron-to-photon conversion was estimated to be in the range of 10^{-3}. Another approach to the description of plasmon excitation in an STM involves current fluctuations due to charge granularity *i. e.* shot noise [69, 83, 84]. As it was shown by Lü, Christensen and Brandbyge these two approaches are consistent with each other and the shot noise can be written in terms of inelastic tunnelling [85]. Shot noise and its importance for STML will be discussed in more detail in Chapter 8.

As expected from the broadband spectrum of plasmons and electrons being able to lose energy to a continuum of states during inelastic tunnelling, the emitted STML plasmonic spectrum spans over a few hundred meV for both bias polarities. This was shown experimentally for the first time by Berndt *et al.* [57]. A spectrum obtained from an Au-Au(111) junction is presented in Fig. 2.1c. Similar spectra have been observed from nanoparticles [86]. Plasmonic emission is known to have a quantum cutoff defined by the applied bias: only modes of an energy that is equal or less the applied energy can be excited ($h\nu \leq eU$) [22]. However, this rule does not strictly apply and the exceptions will be discussed in Chapter 8. The general shape of the spectrum (for bias that is high enough to excite all the modes) is defined by the nanoscale structure of the tip and can be altered in the process of tip preparation. The plasmonic electroluminescence can be modified by the presence of adsorbates affecting both the intensity (change of the branching ratio) [87–89] and the spectrum (change of the dielectric constant) [90]. We will use this effect in Chapter 6 to probe the motion of an adsorbate on the surface and extract its dynamics.

Excited plasmons can be analysed also in the time domain. Their lifetimes have been shown to lie in the femtosecond regime [91, 92], which is beyond the time-resolution of the experimental set-up used in this thesis. Therefore, the plasmonic decay can be considered as instantaneous and used to probe the response of the set-up in the GHz regime [93], which will be discussed in more detail in Section 2.4.3.

---

[3] Plasmons can be excited also by the incoming light.

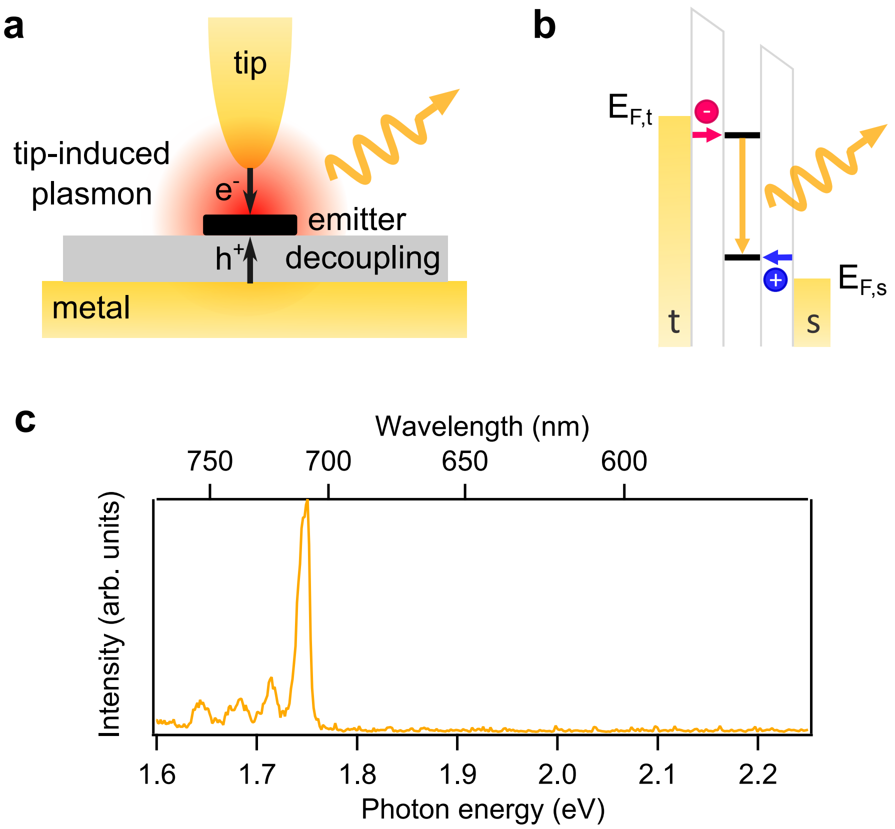

Figure 2.2 – Excitonic electroluminescence. a) A scheme of a tunnel junction emitting light due to the radiative decay of excitons. b) Energy diagram of the exciton formation in a direct injection process. c) A typical spectrum of an excitonic emitter. Here, emission from a C_{60} defect is shown. Note the same horizontal scale as in Fig. 2.1c.

2.2.2 Excitonic electroluminescence

Molecules directly adsorbed on a metal surface only modify the plasmonic luminescence and do not exhibit intrinsic electron-hole (exciton) recombination. This absence of molecular emission is due to the coupling between the molecule and the supporting metal. When the electronic wave functions of a molecule and a metal overlap, the exciton or charge can rapidly decay to the metal. In the case of weaker interaction, the luminescence quenching occurs via electromagnetic dipolar coupling [94–96]. These interactions decay quickly with increasing separation between the emitter and substrate so that decoupling by already few Å is sufficient to observe intrinsic luminescence [60].

So far a number of approaches have been developed to decouple the emitter from the metal [22]. One of them involves a thin insulating layer such as Al_2O_3 [21] or NaCl [60–62, 97] grown on the substrate. Molecular layers have been used as well [19, 87, 98], also in a combination with an insulating layer [99–101]. Another successful approach is based on suspending the emitter between the tip and sample [102–105]. In Chapter 4 of this thesis we will use molecular decoupling, in which lower C_{60} layers decouple the upper ones and serve as a matrix for the emission from individual defects [19, 76, 106–108].

Molecular luminescence requires the creation of an exciton at the emitter. Such an excitation can be achieved in two steps, by populating a high energy level (lowest unoccupied molecular orbital, LUMO) with an electron and a low energy level (highest occupied molecular orbital, HOMO) with a hole. The third step of the process is the radiative decay of the bound electron-hole pair. Importantly, for an exciton to arise, these two states have to spatially overlap and be populated at the same time, which emphasises the need for an efficient decoupling mechanism. Another important prerequisite is the energy level alignment: both states have to be located between the Fermi levels of the tip and the substrate for a given bias voltage (see Fig. 2.2b). An important consequence of this requirement is that the energy level difference between the tip and sample necessary for the photon emission will be higher than the energy of the photon ($h\nu < eU$). Additionally, the effective level position will be modified by the Coulomb attraction and effects related to the voltage drop in the tunnel junction, such as tip-induced band bending [76]. Because of different alignments for both polarities, the voltage threshold will differ and in the extreme case, the luminescence will be possible for only one of the polarities. So far intrinsic STML excited by direct charge injection has been reported in a number of studies on single molecules, molecular layers and semiconductors [22]. Electroluminescence up-conversion effects have been observed as well [98].

Intrinsic STML can be also excited by the plasmon in the junction in an absorption-like process. First, a plasmon is excited upon inelastic tunnelling, which then interacts with a molecule and transfers its energy creating an exciton (similarly to photoluminescence, it occurs in one step), which can subsequently decay and emit a photon. In such a mechanism the voltage threshold is defined by the plasmon excitation: $h\nu \le eU$. An evidence of this energy exchange has been shown recently in spectra exhibiting a Fano-like feature characteristic for the plasmon-exciton interaction [109–111]. The interaction of an exciton with the plasmonic cavity additionally enhances the radiative decay rate, which is described by the Purcell factor. Moreover, the enhancement of the near-to-far-field coupling of the photon emitted due to the exciton decay still plays a crucial role allowing for successful detection of photons emitted from a single molecule (Fig. 2.2a). [22].

An emission spectrum resulting from an individual exciton recombination exhibits a sharp main line (Fig. 2.2c), whose energy is defined by the intrinsic transition of the emitter. It can be followed by a vibrational progression, which can be used to chemically identify the emitting entity. The observed vibronic peaks depend on the respective electronic-vibrational coupling mechanism, which can be influenced by for example the presence of other molecules [97].

Occasionally, the number of active modes will be large and the resulting spectrum will be broad causing the distinction between plasmonic and excitonic luminescence difficult. As shown by Lutz *et al.* [112], the orbitals involved in the transport leading to light emission (inelastic tunnelling channel) can be imaged by light and may differ from the main elastic channel for the given bias. This method of correlating the electronic and luminescence channels will be employed in Chapter 5 to distinguish the plasmonic and excitonic electroluminescence.

Another method of distinguishing both mechanisms relies on their different dynamics, which can be already accessed by probing luminescence vs. current (Chapter 5). Moreover, as mentioned above, the lifetime of a plasmon is extremely short (fs), whereas exciton lifetimes are relatively long, ns for singlets, reaching µs for triplets. These timescales are in the range available for direct time-resolved light detection. As it will be shown in Chapter 4, not only the radiative lifetimes can be probed [19, 60], but also the formation of a single exciton in real-space and real-time.

2.3 Time-resolved STM

STM allows three-dimensional studies of surfaces with atomic precision. Given these possibilities, it was tantalizing to develop the technique towards studies in the time-domain, *the fourth dimension*, in order to follow in real time physical and chemical processes at the sub-nanometre scale. In general, the term time-domain in the STM can be understood in two ways, the first one refers to the time between acquiring subsequent images of the same region, the second one to spectroscopic-like local studies, where the tip position is fixed and only dynamical information is gathered. A standard STM set-up is limited in its speed to the low ms-high µs regime, mostly because of the low bandwidths (kHz range) of tunnelling current amplifiers. However, many interesting processes occur on time-scales that are much faster, therefore a set of techniques has been developed to overcome these limits, especially in recent years. They will be briefly reviewed in the following.

A typical STM image is recorded within a few minutes, depending on the expected quality, which is defined by the integration time per pixel and the number of them in the scan. This time can be reduced (at the expense of quality and size) to a few ms in the so-called *Video-STM* technique [113–115], which can be used for instance to image the growth of a graphene layer in real-time [116]. This time-resolution can be pushed forward, however, it is limited by the possibilities of piezoelectric scanners, the feedback loop and the current amplifier [113, 114].

In order to probe dynamics faster than a few tens of µs, the local approach with an immobilized tip has to be employed. The first successful experiments in the ps regime were presented already in the early 1990s [117], however, this and later studies [118–120] did not demonstrate measurements at the atomic scale. This was achieved by Loth *et al.*, who used an all-electronic pump-probe method to study the ns spin relaxation of few atom magnets [17]. In this approach, the spin system is excited by a pump pulse of amplitude higher than the excitation energy and followed by a probe pulse of an amplitude lower than the excitation energy to sense the spin-polarized current. The delay between the pump and probe pulse is scanned and the signal is obtained by time-integrating the current over many measurements (pulse pairs are applied as a train). This averaged current can be sensed by a slow (kHz bandwidth) current amplifier with a time resolution defined by the width of the pump and probe pulse, and eventually the rise and fall times of the pulses. These properties are limited by the STM wiring, which will be discussed in more detail in Section 2.4.3. This all-electronic pump-probe method has been used to study dynamics of other magnetic systems [121–124] and dopants in inorganic semiconductors [125–127].

Another method of accessing dynamics at the nanoscale using STM is based on coupling the microscope with an ultrafast laser system. One approach involves sending a pair of optical, or near-IR pulses in a pump-probe scheme [16, 20, 120, 128–130], with pulse lengths reaching femtosecond regime. Another recently developed technique, THz-STM [18, 131–133], is based on applying terahertz radiation, which was employed to transiently excite and probe the vibrations of a single molecule [133]. Both of these approaches are based on detecting the time-averaged current signal, as in all-electronic pump-probe methods, therefore requiring a dynamical process that will strongly affect the local density of states (thus the current), a situation that is not always given.

However, time-resolved light detection is not bound by this condition and can resolve processes that are not dominating the tunnelling current as long as they result in photon emission. Additionally, the perturbations by the probe pulse are removed, because a once excited system can freely evolve emitting light, which is detected outside of the tunnelling junction. The fact that STML is based on driving the luminescence with current helps to answer technologically relevant questions about electron-to-photon energy conversion at the ultimate ps-pm scale, which concern for instance OLEDs or quantum technologies. The latter is enabled by the intrinsic access to photon statistics due to the use of single-photon detectors. Indeed, so far time-resolved STML studies mostly focused on studying the statistics of emitted light in the nanosecond regime, first by measuring fluctuations in the tunnel junction in the pioneering studies by the group of F. Charra [134–136]. Recently, a proof of single photon emission in STM from defects in C_{60} has been reported by Merino *et al.* [19], followed by a study of a single photon emitting molecule by Zhang *et al.* [60]. A second approach to probing nanoscale dynamics is based on applying voltage pump pulse and detecting time-resolved luminescence, which was demonstrated by Große *et al.* [93]. In the scope of this thesis, we continue developing time-resolved STM-induced luminescence techniques and apply them to follow dynamics in nanoscale systems. In the next section, we focus on the experimental set-up necessary for probing STML with ps resolution.

2.4 Experimental set-up and techniques

2.4.1 STM

All measurements presented in this thesis were performed using a home-built low temperature (4 K) UHV STM. The set-up consists of 3 vacuum chambers: load-lock, preparation and STM chambers. The load-lock is used for transferring tips and samples between ambient and UHV environment. The preparation chamber is equipped with a sputter gun, sample heating and

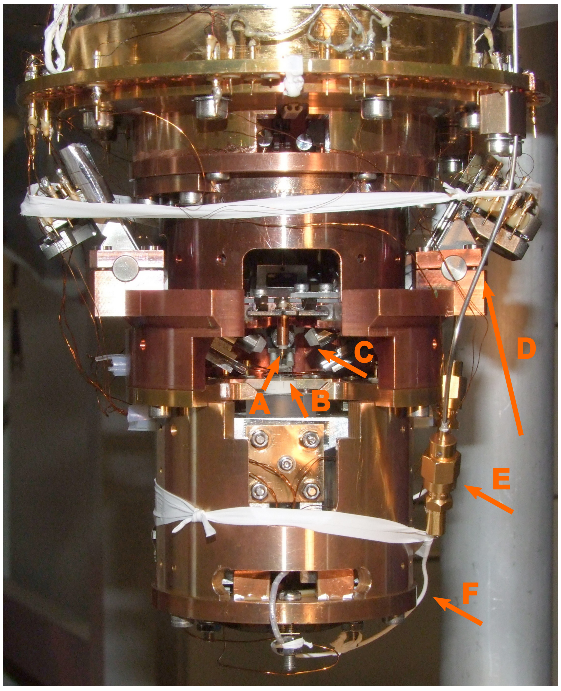

Figure 2.3 – The STM head. Description of the marked elements can be found in the main text.

evaporation stages, two evaporators (for deposition of molecules), metal evaporator, mass spectrometer, vacuum pumps (turbomolecular, ion and getter), manipulator and wobblestick for tip and sample transfers. The chamber maintains a pressure in the 10^{-10} mbar range. The measurement chamber reaches pressures in the 10^{-11} mbar range and is equipped with an ion pump, wobblestick, liquid nitrogen cryostat (40 l) that acts as a thermal shield for a liquid helium cryostat (10 l). The standing time of the instrument is limited by the capacity of the liquid nitrogen cryostat to 48 h - 60 h. The STM head is rigidly attached to the helium bath cryostat so that good thermal contact is provided. The head is protected by two shields, at liquid nitrogen and helium temperatures, respectively. The shields can be opened to transfer tips or samples.

Fig. 2.3 shows a picture of the STM head mounted on the liquid helium cryostat. In this set-up, the tip (marked A) is mounted on a transfer plate, which is placed in the head. The sample stage (marked B) comprises a magnet used to hold the sample in place. To enable magnetic coupling, the sample holder is build using magnetizable steel components. The sample stage is mounted on a piezoelectric tube (fine scanner) that is located on a slip-stick motor (Pan design [137]) used for the coarse approach with a range of a few mm. Since usually in the STM set-ups the sample is immobile, for consistency with typical set-ups where the tip is mounted on a piezo-scanner, we will use the same notation through this thesis when discussing the relative tip-sample motion.

The voltage is applied to the sample, the tip is grounded. The control of the instrument

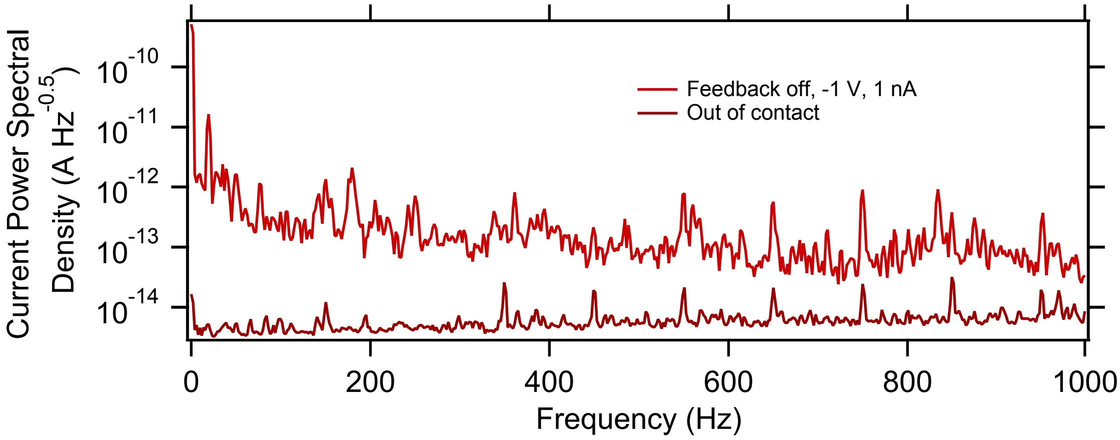

Figure 2.4 – Fourier transform of the tunnelling current. Two spectra show curves recorded in and out of contact.

and data acquisition is performed using *Nanonis* (SPECS Zürich) electronics and software. The software used includes WSXM [138] for image processing, Igor Pro and Matlab for data analysis.

Stability of the instrument

The instrument is located in the Precision Laboratory of Max Planck Institute for Solid State Research in Stuttgart, Germany, which provides excellent stability for performing sensitive STM measurements. Such conditions are achieved by placing the microscope on an air-spring-supported concrete block (120 t) that provides extremely efficient vibrational insulation in addition to acoustical and electromagnetic shielding. The microscope is located in a *box* that serves also as a darkroom and the measurements are controlled from the outside.

To further improve the stability during the measurement, the liquid nitrogen cryostat is pumped below 50 mbar, which results in solidification of nitrogen, thus avoiding vibrations arising from boiling. The noise spectrum obtained by calculating the Fourier transform of the tunnelling current in and out of contact is shown in Fig. 2.4. This stability enables recording images, as presented in this thesis, that do not require any filtering.

2.4.2 Optical access to the tunnel junction

The STM head presented in Fig. 2.3 is equipped with a set of 3 independent aspheric lenses (NA = 0.42) located in the 4 K environment. The lenses enable efficient collection of light emitted from the tunnel junction. One of them is marked as C in Fig. 2.3. Each of these lenses is located on a piezo stage that enables *in situ* adjustment over a distance of ±3 mm along and ±1 mm perpendicular to the beam direction so that the focal points of the lenses can be adjusted to coincide with the immobile tip apex. The lenses are located at an angle of 60° with respect to the surface normal to maximize the collection efficiency (see Section 2.2.1). After passing through the lens, the light is reflected from a mirror, guided through two small (to minimize the heat input) apertures in LHe and LN_2 shields. In between the apertures, there is an intermediate focus of the beam to minimize the cut-off losses. Further, the beam is guided towards a UHV viewport where it leaves the UHV environment. There are three independent paths, one for each lens. In ambient conditions, the light in the three paths is guided (free propagation) towards either one of the two single-photon avalanche photodiodes (SPADs) or an optical spectrometer. Two models of SPADs were used in this thesis: PerkinElmer SPCM-AQRH-15 and MPD-PDM-R, with the latter one offering better time resolution (<50 ps). There is a lens in front of each of the SPADs to focus the beam on the detection chip and the possibility of placing an optical filter (F in Fig. 2.5) on a dedicated holder. The spectrometer consists of a spectrograph (Acton SP 300i, 150 lines/inch blazed grating) coupled to a Peltier-cooled CCD camera (PI-MAX or PI-MAX 4). The intensities of the spectra plotted in the eV scale are corrected for the varying bin size upon conversion from nm scale. More details on the set-up can be found elsewhere [139, 140].

The adjustment of the optical system is performed in two steps. The first one regards the lenses located in the STM head and is performed using a webcam located in the ambient, close to the viewport with an external illumination of the junction. The lens is properly adjusted when the apex and the apertures in the shields are in focus simultaneously and chromatic aberrations become visible. The second step of the adjustment is performed directly on the STML beam (in tunnelling conditions). The SPADs are located on stepping motors that can be controlled from the outside of the *box* and moved until the intensity maximum is found. The motion of the motors does slightly perturb the stability of the junction, however still allows a well-controlled adjustment on metal surfaces. The spectrometer is aligned in an iterative way by adjusting the mirrors guiding the beam until a satisfying intensity is achieved. The total collection efficiency of the set up is estimated to be in the range of 20-30 % [139].

2.4.3 Time-resolved electroluminescence

The time resolution of the SPADs (50 ps) allows studies of time-resolved electroluminescence from the tunnel junction, which can be realized in different experimental schemes. In the scope of this thesis, two set-ups were used (Fig. 2.5), namely Hanbury Brown-Twiss STM (HBT-STM) and time-resolved STML (TR-STML), both of them relying on a time-correlated single photon counting PC card (TCSPC, Becker and Hickl, SPC-130). However, the versatility of the microscope and its optical set-up provides the possibility of creating other detection schemes outside the vacuum chamber.

Time-resolved STML

TR-STML is based on applying fast voltage pulses to the STM (Fig. 2.6). The pulses are provided by an arbitrary wave generator (AWG, Agilent M8190A), attenuated by 6 dB (half of the voltage

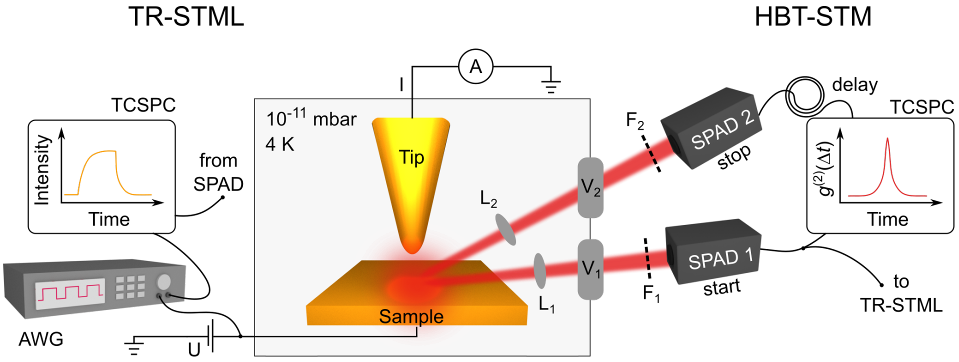

Figure 2.5 – Experimental set-up for time-resolved electroluminescence measurements. L - lens, V - viewport, F - filter. Details are described in the main text. The spectrometer path is not shown.

amplitude) and send to the tunnel junction via a bias tee (Picosecond Pulse Laboratories, 5550B), which allows adding a DC offset. The DC voltage is provided by the *Nanonis* controller and allows convenient operation of the set-up, without the risk of disconnecting voltage supply, because no additional switches are needed. The change of bias in the junction leads to a change in the luminescence that is recorded with ps time resolution. The TCSPC card is synchronized with the AWG that sends a trigger pulse along with every pulse sent to the junction. Such a synchronisation scheme allows recording a histogram of counts that in the limit of low intensity (a typical case for molecular systems) results in an electroluminescence transient. An important issue for such a measurement is the distortion of the pulse shape due to the imperfections of the wiring. We will now discuss strategies for optimization and correction of these effects in order to achieve a well-controlled time-dependent voltage in the tunnel junction.

Every electrical circuit can be characterized by its transfer function, which describes the fraction of the applied signal at a defined frequency that is transmitted over the circuit. In the STM set-up, this transfer function is limited by the quality of the cables used to connect the head and the presence of a tunnel junction with GΩ resistance. These imperfections lead to reflection and absorption of the signal and therefore a complicated transfer function in the MHz regime and beyond. The practical result of this perturbed transmission is the distortion of every signal that has Fourier components in the range of varying transmission. The transmission can be measured by STML using the approach developed by Große *et al.* [93]. This method relies on the fact that the lifetime of the plasmon is in the femtosecond regime and its intensity $\mathscr{P}(U)$ increases monotonically (such that $\mathscr{P}^{-1}$ exists) with voltage. Because of that relation and the practically instantaneous luminescence response, a light detector with ps resolution is able to probe the transient voltage of the system up to the MHz and GHz regime. The obtained light transient $P(t)$ can be converted to a voltage transient in the junction $U_{junction}(t)$ using the previously measured light intensity vs voltage, $\mathscr{P}(U)$, curve. By applying a known voltage transient U_0(t) and recording $U_{junction}(t) = \mathscr{P}^{-1}(P(t))$,

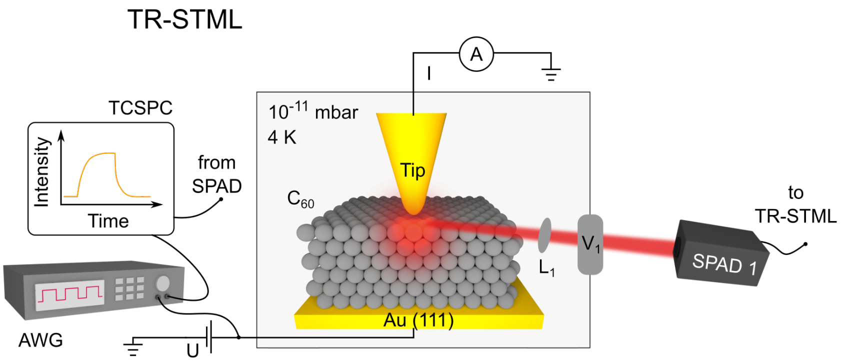

Figure 2.6 – Experimental set-up for TR-STML. The arbitrary wave generator (AWG) provides pulses that are sent to the tunnel junction and synchronized with the time-resolved light detection (TCSPC).

the transfer function is then calculated from the Fourier transforms of the applied and probed voltage:

$$T(\nu) = \frac{\mathscr{F}[U_{junction}(t)]}{\mathscr{F}[U_0(t)]} \tag{2.6}$$

For instance, when we apply a rectangular pulse (Fig 2.7b, black trace), record the light intensity and convert it to the bias (Fig 2.7b, magenta trace) we observe that the voltage in the junction is distorted. The edges of the pulse are not sharp and there is a reflection appearing with a delay of 130 ns. The transfer function calculated from this measurement is presented in Fig. 2.7a in black. We can compare it with a measurement done externally, using a network analyser (Keysight Technologies, N9912A). This evaluation was performed at room temperature by crashing a tip into the sample stage and connecting the network analyser to the STM input (voltage) and output (current) at the UHV feedthrough. Both approaches reproduce similar features, the transmission decreases in the few hundred MHz regime, with a dip around 200 MHz and is low in frequencies approaching 1 GHz.

The transmission has been improved significantly as compared to measurements presented in [93], which were performed using standard low-temperature STM wiring. The section of the wire from the UHV feedthrough to the STM head is made of a semi-rigid wire (see D in Fig. 2.3), which transmits the signal well until few tens of GHz. At the head, there is an SMA connector (E in Fig. 2.3, also specified for GHz frequencies), which links the semi-rigid wire to a shielded and flexible coaxial wire (F in Fig. 2.3). Fig. 2.3 shows the wire leading to the sample (voltage contact), similar connections are done also for the tip contact (current). In the scope of this thesis, we have improved the connection from the SMA connector to the STM sample stage. Previously, the shield in the flexible coaxial wire was not connected, after the improvements, it is linked both to the SMA connector and grounded to the STM body close to the sample. This better wiring and better shielding provide an improvement in the transmission.

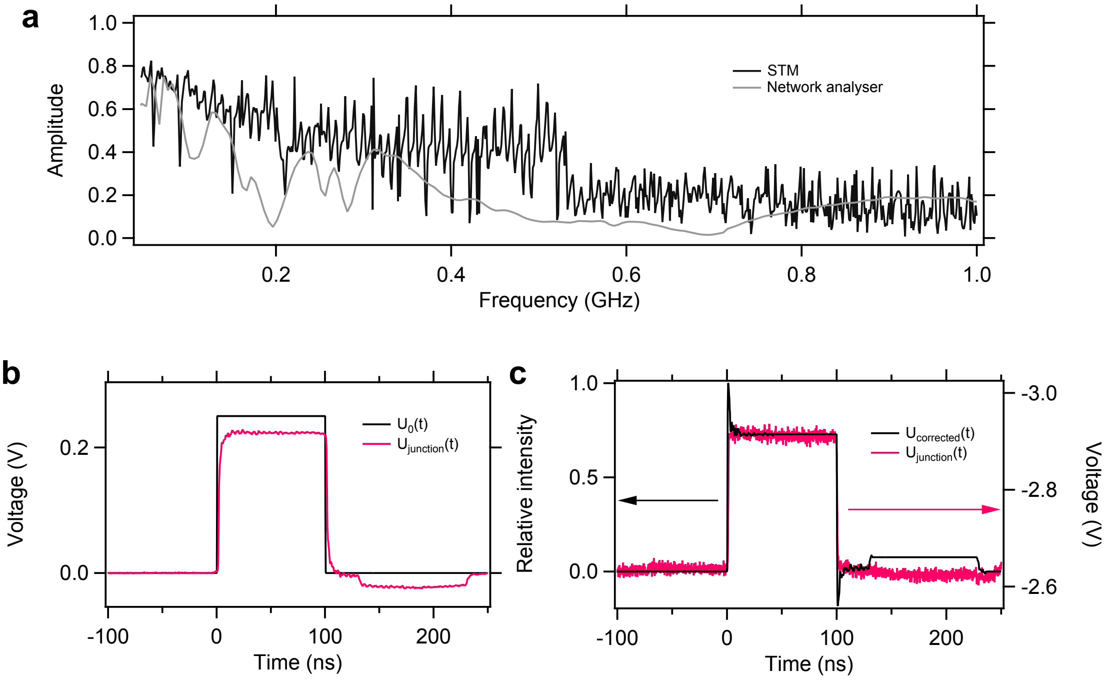

Figure 2.7 – Corrections to the rectangular pulses. a) Transfer function as measured by the STM employing eq. 2.6 (black) and transfer function obtained using a network analyser (grey) b) A rectangular pulse (black) applied to the STM and the resulting voltage in the junction (magenta), the pulses were applied over a DC offset of -1.9 V, I = 6 nA. c) The shape of the pulse after the corrections (black) and the resulting voltage in the junction (magenta) for I = 1 nA. The measurements were performed on Au(111) surface.

Even though the transmission has been improved, the pulses still have to be properly shaped in order to compensate for imperfections. Optimal strategies to do so, have been developed in the scope of a master thesis by R. Froidevaux (EPFL, 2014). First of all, the edges of the applied pulses are not step functions but are halves of a Gaussian in order to reduce high-frequency Fourier components. Next, we obtain the transfer function from eq. 2.6 and calculate the corrected pulse using:

$$U_{corrected}(t) = \mathscr{F}^{-1}\left(\frac{U_0(\nu)}{T(\nu)}\right) \tag{2.7}$$

where $\mathscr{F}^{-1}$ indicates inverse Fourier transform. The $U_{corrected}(t)$ obtained in such a way has to be smoothed to remove noise, including manually fixing the regions away from the edges to a constant value. The pulse thus obtained is applied again to the junction to check the voltage profile and if necessary corrected in an iterative manner.

After applying the corrections described above, we have achieved a pulse whose shape is presented in black in Fig. 2.7c. We test its performance on a pristine Au(111) surface and observe a well-defined rectangular voltage transient (magenta trace in Fig. 2.7c), which is not

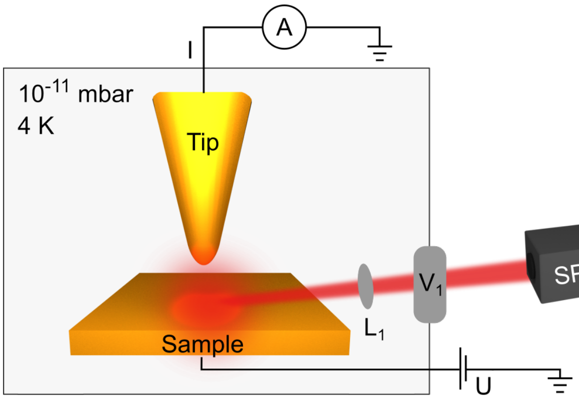

Figure 2.8 – Set-up for correlations with one detector. The photon arrival times registered by the SPAD are saved and used to compute the photon correlation function.

perturbed by reflections and oscillations. Its edges are characterized by the 10-90% voltage transition times of 1 ns. Next, we also need to take into account the offset effect. In the pure AC components (amplified output of the AWG and the bias tee), the average transmitted signal has to time-average to zero, which results in a shift of the bias offset, as compared to the one applied from the STM controller. For the 20 % duty cycle, 2 MHz repetition rate and amplitude of 300 mV used in this thesis, this correction to the voltage in the junction amounts to 70 mV. A pulse prepared in such a way is ready for probing charge and exciton dynamics as it will be shown in Chapter 4.

The advantage of the STM combined with light detection is the direct access to the transient voltage in the junction. In the set-ups without light detection scheme, the transmission can be probed utilizing non-linearities in the current-voltage curve that generate a strong signal, which can be probed as a function of frequency [93, 141, 142]. So far, the fastest time resolution using voltage pulses sent to the tunnel junction was reported by Saunus *et al.* to be 120 ps [143] using the all-electronic pump-probe method. However, no corrections for the transmission function were applied.

Correlations with one detector

The next two configurations of the detection set-up involve measuring photon correlations, whose principles and properties will be discussed in Chapter 3. In brief, photon correlations inform about photon statistics, from which dynamical information about the system can be extracted. In the first configuration, we use only one SPAD (see Fig. 2.8) and record arrival times of every photon in the so-called FIFO (first-in-first-out) mode of the TCSPC to obtain the time-dependent light intensity I(t). These data can be used to compute the autocorrelation

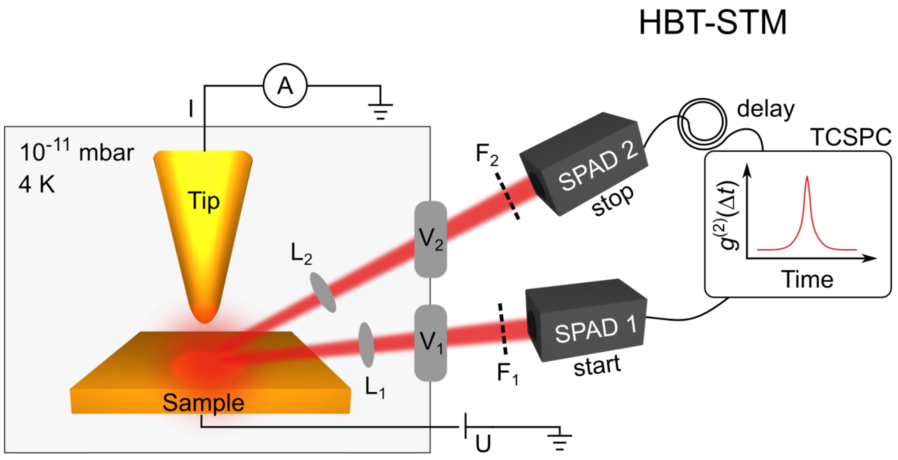

Figure 2.9 – Hanbury Brown-Twiss STM set-up.

function:

$$R(\Delta t) = \int_{-\infty}^{+\infty} I(u)I(u+\Delta t)du \tag{2.8}$$

and convert it to the correlation function, $g^{(2)}(\Delta t)$:

$$g^{(2)}(\Delta t) = \frac{R(\Delta t)}{R(\Delta t \to \infty)} \tag{2.9}$$

The useful time range of this configuration is limited to a few µs by an intrinsic artefact of the SPAD - afterpulsing. It arises from the non-zero probability of producing additional pulses (fake counts) within a few µs after the detection of a photon and results in a positive correlation. Ultimately, the time-resolution in a one-detector set-up is limited by the dead time of the detector (40-70 ns).

Hanbury Brown-Twiss STM

To overcome this limit set by the detector's dead time and fully explore the accessible time range (> 50 ps) it is necessary to use two detectors set up in a Hanbury Brown-Twiss (HBT) interferometer (see Fig. 2.9). It consists of two arms, each terminated with an SPAD. One of the detectors serves as a "start" detector that starts the timer of a TCSPC upon detection of a photon. The second SPAD is a "stop" detector that stops the timer. A histogram of these measured delay times can be plotted and is a direct measurement of the (non-normalized) $g^{(2)}(\Delta t)$ function. A delay line introduced in the "stop" cable connecting the SPAD with TCSPC allows probing events where the "stop" detector registers a photon before the "start" detector

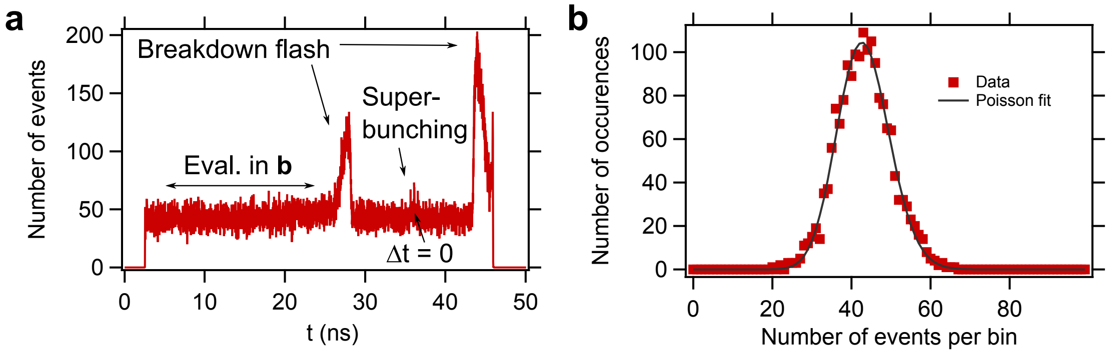

Figure 2.10 – Analysis of the HBT-STM measurement. a) Raw correlation data recorded on Ag(111) surface, U = 4 V, I = 750 pA, t = 600 s, P_{SPAD1} = 60 kcts s^{-1}, P_{SPAD2} = 80 kcts s^{-1}. b) Histogram obtained from the data indicated in a), the data is described well by a Poissonian distribution.

(negative times). In that situation and a long enough delay line, the pulse from the "start" detector arrives at the TCSPC before the "stop" pulse.

Fig 2.10a shows raw data acquired during a correlation measurement for a time bin of 12 ps. The first and last 10 % of the measurement are discarded due to the artefacts of the TCSPC. The graph shows 3 distinct features: a peak around $t = 36$ ns and two mirrored-symmetric features around $t = 28$ ns and $t = 44$ ns. The latter features can be ascribed to the breakdown flash of the SPADs. When a photon is detected, electron-hole pairs that arise during the avalanche event can radiatively recombine and emit a photon. Such a photon can travel to the STM head, reflect from the junction and be detected at the other SPAD leading to a correlation count at a time delay corresponding to the length of its light path. Even though such an effect is undesirable (and can be filtered out by optical filters), it can be used to find the *zero time delay* corresponding to the simultaneous emission of two photons from the STM. This zero time delay is located halfway between the artefacts, *i. e.* at $t = 36$ ns. At this position we find a peak, which, as it will be presented in Chapter 7, corresponds to a photon bunching (an emission of a photon pair) from a tunnel junction. The presence of this effect is another method of determining the zero time delay. We see that in this configuration time zero $\Delta t = 0$ is located at delay $t = 36$ ns, which corresponds to delay line length of ≈ 7 m (the distance from the junction to both SPADs is roughly equal). As a rule of thumb, 20 cm of the cable correspond to 1 ns delay, assuming that the signal in the cable travels with 2/3 of the speed of light in vacuum, c. For the analysis, all correlation curves presented in Chapter 7 are corrected by this value of 36 ns.

As an additional analysis, we can evaluate the statistics of the uncorrelated counts, as marked in Fig 2.10a. The calculated histogram is presented in Fig 2.10b and can be described by Poissonian statistics. The details of the photon statistics will be discussed in Chapter 3.

Measurement of the detector time response

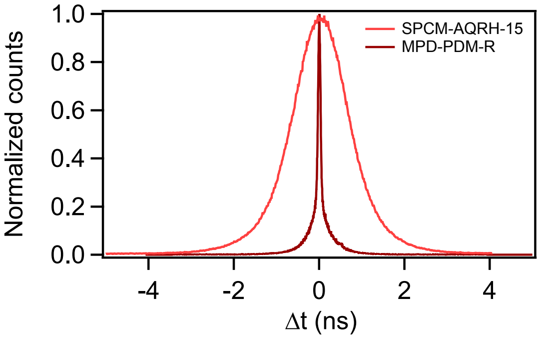

Figure 2.11 – Time resolution of the SPADs.

In the scope of this PhD thesis, the SPADs were exchanged from PerkinElmer SPCM-AQRH-15 to MPD-PDM-R model in order to improve the time resolution of photon correlation measurements and reduce the dark count rate. To characterize both new and old SPADs, detector time response measurements were performed. We use light from a pulsed super-continuum laser source (Fianium WhiteLase, WL-SC-400-40, 80 MHz repetition rate, 6 ps fundamental pulse width), which is filtered (Fianium LLTF Contrast VIS, < 2.5 nm spectral bandwidth) to obtain 690 nm optical pulses with a length of few tens of ps. Such light is attenuated and sent towards paper screens located on the optical paths leading to the SPADs. The scattered light is recorded by the detectors that operate in the HBT-STM scheme ("start"-"stop"). In this case, the light is trivially bunched due to the pulsed beam, so a positive correlation at time zero is expected. The results are shown in Fig. 2.11, the FWHM are 1.4 ns for the PerkinElmer model and 70 ps for the MPD model. For SPCM-AQRH-15 detectors the contribution of the laser peak to the FWHM is negligible, however, for MPD-PDM-R SPADs it contributes significantly and results in a deviation from the value provided by the manufacturer (30 ps). Because of this additional broadening from the laser pulse width, the real time-resolution limit can be probed by an effect that occurs on a faster time scale, such as the photon pair production shown in Chapter 7.

2.4.4 Sample preparation

The Au(111), Ag(111) and Cu(111) single crystals are prepared in the UHV by repeated cycles of Ar^+ ion sputtering (0.9 kV) and annealing up to 850, 830, 920 K for Au, Ag, Cu, respectively. C_{60} thin films are grown on previously cleaned Au(111) surface by thermal evaporation of molecules from a Knudsen cell heated up to temperatures in the range 820-840 K with evaporation times in the range between 40 and 60 minutes. The substrate is kept at room temperature. After preparation, the sample is *in-situ* transferred into the liquid helium cooled STM. Cooling of the sample during evaporation results in a growth of rougher film structure. During growth half of the sample is covered by a shutter located 2 mm from the sample. This side without adsorbates allows performing tip preparation on the same crystal.

2.4.5 Tip preparation

The tips used for the experiments presented in this thesis are prepared from a pure (99,999%) Au wire. In order to obtain the desired shape, the tips are electrochemically etched in HClethanol solution following the recipe from Ren *et al.* [144]. Afterwards, the tips are inspected with an optical microscope in order to select ones that are sharp and not contaminated. Prior to introducing the tips into the UHV chamber, they are pre-aligned in the tip holder. It is necessary due to the limited range of motion of the lenses located in the STM head.

Gold tips prepared in the described way do not require additional sputtering or annealing and can be inserted directly to the STM via the load-lock chamber. Before the measurements, the tip is prepared on a pristine metal surface (Au(111), Ag(111) or Cu(111)) by voltage pulses and controlled indentation. A tip is considered good for measurements on C_{60} thin films (Chapter 4 and 5), which is the most demanding system studied in the scope of this thesis when the following conditions are met:

- The tip sharply resolves atomic steps and does not show any multiple tip features.
- The measured dI/dV spectroscopy is smooth in the desired range (0 V → -3 V), does not exhibit unexpected features (peaks) and well resolves the surface state.
- The intensity recorded by at least one SPAD exceeds 20 kcts s^{-1} for -3 V, 100 pA.
- The maximum of the optical spectrum of the plasmonic electroluminescence (maximum enhancement) is located around 700 nm (the excitonic emission of C_{60}).

The sharpness of the tip can be verified by measuring the dz/dV spectrum [145]. Gold tips are occasionally found to be non-conductive, which is evident by crashes during approach procedure and the observation of an extremely tilted surface plane - the tip either loses contact or crashes into the surface (the motion range of the scanner is exceeded). Such a tip can be improved by voltage pulses, deep indentations (in the order of 1 μm) or field emission. Interestingly, performing field emission of an Au tip over Ag(111) surface was found to improve the plasmonic enhancement by a factor of 2, probably by efficient covering the apex with silver.

3 Modelling nanoscale dynamics on surfaces

This chapter will define the mathematical basis and the analytical toolbox used throughout this thesis. First, we will discuss different types of photon statistics and show how photon correlations carry information about dynamics at the nanoscale. Later, we will show how to model these correlations using kinetic rate models, which, due to their generality, can be applied to different physical systems studied during this thesis and used to extract their respective dynamics.

3.1 Photon statistics

Many of the properties of the electromagnetic radiation can be described by the classical wave approach. However, for some processes such as black-body radiation or the photoelectric effect, the classical picture is insufficient and it has to be combined with a particle approach to fully explain the observed effects. This concept known as the wave-particle duality lies in the core of quantum mechanics and applies both to light and matter. Considering light as a stream of particles arriving at a detector, one important question immediately arises: what is the temporal distribution of photons in such a train? An answer to this question is obtained by analysing the fluctuations in the number of photons (photon statistics) and the properties of the light source.

First, we shall consider the most stable light - a perfectly coherent beam, a good approximation of which is a beam from a single-mode laser. The intensity of such a beam is constant as well as the average photon flux. However, even though the flux is constant, there are fluctuations on a short time-scale due to the discrete nature of photons. These fluctuations have a Poissonian distribution characteristic for a discrete random process, for instance, a number of decay events in a given time interval from a radioactive source [146]. The fluctuations in the photon number n within a given time interval around the mean value $\overline{n} = \sum_n nP(n)$ can be characterized by the variance:

$$Var(n) = (\Delta n)^2 = \sum_n (n - \overline{n})^2 P(n) \tag{3.1}$$

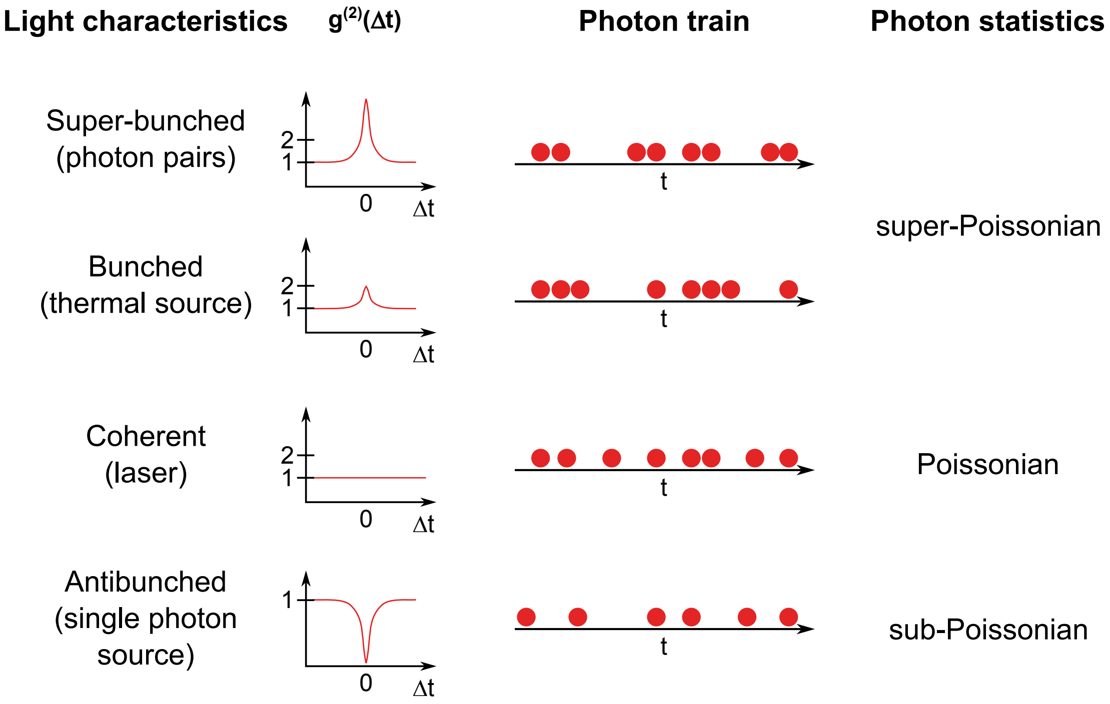

Figure 3.1 – Overview of different photon statistics.

Where Δn is the standard deviation and $P(n)$ the probability of finding n photons within a defined time slot.

For Poissonian statistics, the variance is equal to the mean value thus:

$$\Delta n = \sqrt{\bar{n}} \tag{3.2}$$

In the classical picture, the intensity ($I(t)$) fluctuations can be quantified using the second-order correlation function defined as:

$$g^{(2)}(\Delta t) = \frac{\langle I(t)I(t+\Delta t)\rangle}{\langle I(t)\rangle\langle I(t+\Delta t)\rangle} \tag{3.3}$$

Where Δt is the time delay and the $\langle\ldots\rangle$ indicate time average over a long time period. The first-order correlation function describes the time-dependent fluctuations of the electric field. For the coherent source (with Poissonian statistics), the intensity is constant $\langle I(t)\rangle = \langle I(t+\Delta t)\rangle = I$ and thus:

$$g^{(2)}(\Delta t) = 1 \tag{3.4}$$

for all possible values of Δt. The unity value of the correlation function states that the analysed light is uncorrelated.

It is useful here to define the $g^{(2)}(\Delta t)$ function also for the modern light detection scheme, which is based on counting individual photons. As the number of counts n is proportional to the light intensity impinging on the detector, we can write that:

$$g^{(2)}(\Delta t) = \frac{\langle n(t)n(t+\Delta t)\rangle}{\langle n(t)\rangle\langle n(t+\Delta t)\rangle} \tag{3.5}$$

In the subsequent part of this section, we will discuss different types of photon statistics (super-Poissonian and sub-Poissonian), and the correlation functions obtained from respective photon trains, which exhibit correlations. These are summarized in Fig. 3.1.

3.1.1 Photon bunching

As discussed above, the perfectly coherent source emits uncorrelated photons. However, a partially coherent source (like chaotic light from a discharge lamp) will show intensity fluctuations ($\Delta I(t) \neq 0$) if we measure a photon train for a time interval comparable or less than the coherence time. We can write the light intensity as: $I(t) = \langle I\rangle + \Delta I(t)$. From eq. 3.3 with $\Delta I(t) \neq 0$ it can be then derived that:

$$g^{(2)}(0) \geq 1 \tag{3.6}$$

And for long delay times (much longer than the coherence time of the source) $g^{(2)}(\Delta t \to \infty) = 1$. Additionally, for collision or Doppler-broadened (due to the random thermal motion) chaotic light $g^{(2)}(0) = 2$ [147], as presented in Fig. 3.1. This characteristic value of $g^{(2)}(0) = 2$ is valid also for black-body radiation as it can be shown using second quantization description [146]. In this way, the correlation function provides information about the nature of the emitter.

A value $g^{(2)}(0) > 1$ is an indicative that the light in the photon train is bunched. It means that there is a higher probability of recording a photon shortly after another one was detected than after a longer time. In the classical picture, it can be also understood by looking at the intensity fluctuations - during the time when intensity is above the average value there will be more photons than during the time when the intensity is below the average value, leading to a formation of photon bunches (see also Fig. 3.1).

We can analyse the photon statistics of such chaotic and thermal sources and find that [147]:

$$\Delta n = \sqrt{\overline{n} + \overline{n}^2} \tag{3.7}$$

Which shows that these sources have super-Poissonian statistics ($\Delta n > \sqrt{\overline{n}}$). One important remark has to be noted here: for thermal light, this relation applies only to light emitted from a single mode and for chaotic sources only for times shorter than the coherence time. For different conditions (multimode light, long time delays) the statistics revert to a Poissonian case ($g^{(2)}(0) = 1$), which makes the observation of bunching challenging. The demonstration of this effect was done for the first time by Hanbury Brown and Twiss who designed an intensity interferometer [148] and used it to show photon bunching in the light emitted from Sirius [149], which due to the distance from the source can be approximated as light emitted from a single mode of a thermal source. Even though this experiment was performed on the extremely large scales of stars, Hanbury Brown-Twiss (HBT) interferometry has become an indispensable tool of quantum optics used for studying light emission on the extremely small scales of atoms, molecules and quantum structures [150].

We shall remark that the value of $g^{(2)}(0)$ is not limited to a maximum of 2. Sources that emit multiple photons at the same time also exhibit bunching [151], whose index ($g^{(2)}(0)$) can take arbitrarily high values. This effect is normally referred to as super-bunching. Chapter 7 will show such an effect from a tunnel junction, which arises due to an emission of photon pairs.

Photon bunching, in a way, can be also artificially introduced to the system (not directly reflect the properties of the source), by for example chopping the photon stream by some external mechanism. In the scope of this thesis, we use voltage pulses to correlate the time-resolved light emission with an external excitation in Chapter 4 and 5, and probe the dynamics of a single hydrogen molecule, which alters light emission (leading to bunching) when placed in the tunnel junction as it will be shown in Chapter 6. The timescale of bunching informs about the dynamics of the system.

3.1.2 Photon antibunching

So far we have discussed Poissonian and super-Poissonian statistics. The third type of photon statistics, sub-Poissonian statistics follows the relation:

$$\Delta n < \sqrt{\bar{n}} \tag{3.8}$$

Which means that the photon distribution is narrower than for the Poissonian statistics. In the classical wave picture of light, it is not possible to find a wave that would exhibit such a property. On the contrary to bunching, only in the quantum picture of light is it possible to discuss a system that exhibits sub-Poissonian statistics - for example, a single photon source. Such a device emits photons one by one, always separated by a time, which is needed to produce another photon. For a single atom or a molecule, this time delay often corresponds to the radiative lifetime of an excited state (τ_{ex}).

A photon train as described above exhibits antibunching - the photons are separated in time, as presented in Fig. 3.1. Using the definition of correlation function presented in eq. 3.5 we see that for a perfect single photon source we have:

$$g^{(2)}(0) = 0 \tag{3.9}$$

The correlation function increases in time (in principle with a time constant τ_{ex}) and reaches the asymptotic value of 1 for large values of Δt. Remarkably, $g^{(2)}(\Delta t) < 1$ can be observed also for systems such a two-photon source, with its minimal value $g^{(2)}(0) = 0.5$, therefore only $g^{(2)}(0) < 0.5$ proves single photon emission. As the radiative lifetime is embedded in the correlation curve, measuring $g^{(2)}(\Delta t)$ provides access to this dynamical property of the system.

3.1.3 Measurement of $g^{(2)}(\Delta t)$

In simple words, the $g^{(2)}(\Delta t)$ function describes how likely it is to detect one photon after time Δt under the condition that the previous detection occurred at $\Delta t = 0$, which can be used to probe the dynamics of a system. Therefore the experimental setup comprising STM and the Hanbury Brown-Twiss interferometer described in the previous Chapter (Section 2.4.3) allows us to measure the $g^{(2)}(\Delta t)$ function. However, a result obtained this way is not normalized (a number of event occurrence is measured), thus normalization has to be performed in the data analysis step. As shown above, for long delay times, $g^{(2)}(\Delta t)$ naturally approaches 1, which can be used to calculate $g^{(2)}(\Delta t)$ from the number of events at respective time delays $p(\Delta t)$:

$$g^{(2)}(\Delta t) = \frac{p(\Delta t)}{p(\Delta t \to \infty)} \tag{3.10}$$

Where infinity is defined as a time delay at which the dynamics of the system is no longer observed and $p(\Delta t)$ is constant. An alternative approach to the normalization would include a measurement with a single-mode laser (a Poissonian source) with the same average intensity as the one measured for the probed system.

The correlation function may be also measured in a configuration with only one detector (see Section 2.4.3) by recording time-dependent light intensity $I(t)$ and calculating its autocorrelation:

$$R(\Delta t) = \int_{-\infty}^{+\infty} I(u)I(u+\Delta t)du \tag{3.11}$$

Which can be normalized to infinity using eq. 3.10 to achieve $g^{(2)}(\Delta t)$.

For a more detailed discussion on photon correlations and statistics, an interested reader is referred to the classical quantum optics textbooks by Loudon [147] and Fox [146].

3.2 Two state model

Having discussed the principles of photon statistics and photon correlations, we will now show how we can model processes leading to photon bunching and antibunching. For that purpose,

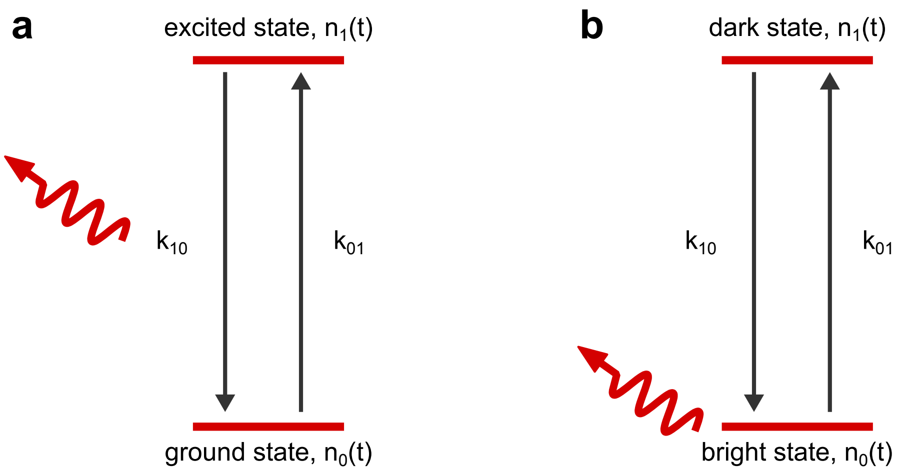

Figure 3.2 – A two state system. a) The photon emission occurs during the transition from the excited to the ground state. b) The system emits while in one of the two states (labelled as bright).

we will use rate equations. They are commonly used in modelling optical processes like the spontaneous/stimulated emission and absorption (employing the Einstein coefficients), as well as for modelling the photo- and electroluminescence from nitrogen-vacancy (NV) [152–154] and silicon-vacancy (SiV) [155] centres in diamond, which are single photon emitters.

We will begin with the most simple two (ground and excited) state system with the respective time-dependent populations $n_0(t)$ and $n_1(t)$. There are two possible transitions for such a system, from the ground to the excited state and back with the rates k_{01} and k_{10} respectively, which are illustrated in Fig. 3.2. Such two-state description can be used to describe for example photoluminescence, a process in which the excitation occurs in one step (absorption of a photon) and is followed by a radiative decay (see Fig. 3.2a). The rate constants and the respective time constants are bound by the reciprocal relation:

$$k_{01} = \frac{1}{\tau_{01}} \tag{3.12}$$

The master equation of a two level system can be written as follows:

$$\frac{d}{dt}\begin{bmatrix} n_0 \\ n_1 \end{bmatrix} = \begin{bmatrix} -k_{01} & k_{10} \\ k_{01} & -k_{10} \end{bmatrix} \begin{bmatrix} n_0 \\ n_1 \end{bmatrix} \tag{3.13}$$

Assuming that we consider an individual quantum system (not an ensemble) and at $t = 0$ the system is in the ground state, we have the following boundary conditions:

$$\begin{aligned} n_0(0) &= 1 \\ n_1(0) &= 0 \end{aligned} \tag{3.14}$$

Solving eq. 3.13 yields:

$$n_0(t) = \frac{1}{k_{01} + k_{10}} \left(k_{10} + k_{01} e^{-(k_{01}+k_{10})t} \right) \tag{3.15}$$

And:

$$n_1(t) = \frac{1}{k_{01} + k_{10}} \left(k_{01} - k_{01} e^{-(k_{01}+k_{10})t} \right) \tag{3.16}$$

For a photoluminescence process (with k_{10} being the radiative transition) the time-dependent intensity will depend on the population of the excited state and the radiative rate: $k_{10} n_1(\tau)$ and the correlation function can be calculated using [152]:

$$g^{(2)}(\Delta t) = \frac{k_{10} n_1(\Delta t)}{k_{10} n_1(\Delta t \to \infty)} = 1 - e^{-(k_{01}+k_{10})\Delta t} \tag{3.17}$$

With a normalization to infinity as discussed above. The value of correlation function at $\Delta t = 0$ is zero showing that an individual photoexcited two-state system is a single photon emitter. In the weak excitation regime [156] $k_{01} \to 0$ and eq. 3.17 reduces to:

$$g^{(2)}(\Delta t) = 1 - e^{-k_{10}\Delta t} \tag{3.18}$$

this shows that measuring $g^{(2)}(\Delta t)$ provides access to the radiative lifetime of the excitation ($\tau_{10} = k_{10}^{-1}$).

In the scope of this thesis we will be interested in analysing the correlation function for a bright-dark two state system (Chapter 6). In such a case, the light is emitted while the system is in the bright state and the emission is suppressed in the dark state, as shown schematically in Fig. 3.2b. The probability of detecting a photon after an event at $\Delta t = 0$ will be proportional to $n_0(t)$ (how likely it is for the system to be in the bright state) and the correlation function can be calculated similarly to eq. 3.17:

$$g^{(2)}(\Delta t) = \frac{n_0(\Delta t)}{n_0(\Delta t \to \infty)} = 1 + \frac{k_{01}}{k_{10}} e^{-(k_{01}+k_{10})\Delta t} \tag{3.19}$$

From this equation we see that:

$$g^{(2)}(0) = 1 + \frac{k_{01}}{k_{10}} > 1 \tag{3.20}$$

Showing that luminescence from a bright-dark system exhibits photon bunching.

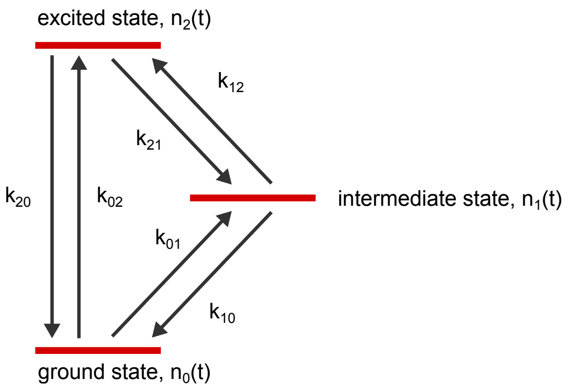

Figure 3.3 – A general three state model.

3.3 Three state model

In contrary to photoluminescence, electroluminescence due to the radiative decay from an excited state is a three-state process. It requires an injection of two opposite charges (electron and hole) into the system and thus has to be modelled using a three state system, as for example used by Khramtsov *et al.* to describe electrically driven NV centres. [154]. A general model with all possible transitions is presented in Fig. 3.3. The master equation of such a system can be written as:

$$\frac{d}{dt}\begin{bmatrix} n_0 \\ n_1 \\ n_2 \end{bmatrix} = \begin{bmatrix} -k_{01}-k_{02} & k_{10} & k_{20} \\ k_{01} & -k_{10}-k_{12} & k_{21} \\ k_{02} & k_{12} & -k_{20}-k_{21} \end{bmatrix} \begin{bmatrix} n_0 \\ n_1 \\ n_2 \end{bmatrix} \tag{3.21}$$

In this thesis we will be interested in a reduced three state model in which some of the transitions do not occur. Modelling a continuous electroluminescence requires only a set of three rates, as shown in Fig. 3.4a, which can be physically interpreted as subsequent injection of a hole and an electron followed by an electron-hole pair (exciton) recombination. The general master equation (eq. 3.21) reduces then to:

$$\frac{d}{dt}\begin{bmatrix} n_0 \\ n_1 \\ n_2 \end{bmatrix} = \begin{bmatrix} -k_{01} & 0 & k_{20} \\ k_{01} & -k_{12} & 0 \\ 0 & k_{12} & -k_{20} \end{bmatrix} \begin{bmatrix} n_0 \\ n_1 \\ n_2 \end{bmatrix} \tag{3.22}$$

For an individual system, assuming that at the beginning it is in the ground state we have the following boundary conditions:

$$\begin{aligned} n_0(0) &= 1 \\ n_1(0) &= 0 \\ n_2(0) &= 0 \end{aligned} \tag{3.23}$$

This system can be solved analytically as well, with solutions that have the form of weighted exponentials:

$$n(t) = Ae^{\lambda_1 t} + Be^{\lambda_2 t} + Ce^{\lambda_3 t} \tag{3.24}$$

For clarity we will show here only the relevant expressions. The methods used in this thesis are based on detecting photons emitted upon a radiative transition. For a three state system, k_{20} is the rate responsible for the radiative transition (exciton recombination), which will be often referred to as k_{ex}. The detected luminescence intensity ($P(t)$) then depends on this rate, the time-dependent population of the excited state $n_2(t)$ and the detection efficiency η:

$$P(t) = \eta k_{20} n_2(t) \tag{3.25}$$

The population of the excited state equals:

$$n_2(t) = \frac{k_{01}k_{12}}{R}\left(1 + \frac{S-Q}{2Q}e^{-\frac{S+Q}{2}t} - \frac{S+Q}{2Q}e^{-\frac{S-Q}{2}t}\right) \tag{3.26}$$

With the following substitutions:

$$\begin{gathered} S = k_{01} + k_{12} + k_{20} \\ R = k_{01}k_{12} + k_{12}k_{20} + k_{20}k_{01} \\ Q = \sqrt{S^2 - 4R} \end{gathered} \tag{3.27}$$

And:

$$P(t) = \eta\frac{k_{01}k_{12}k_{20}}{R}\left(1 + \frac{S-Q}{2Q}e^{-\frac{S+Q}{2}t} - \frac{S+Q}{2Q}e^{-\frac{S-Q}{2}t}\right) \tag{3.28}$$

Light intensity as a function of tunnelling current

Equation 3.28 describes a general time-dependent light intensity from an electrically pumped three state system. We will now focus on specific applications and extensions of this equation that will be critical for the description of mechanisms occurring in the investigated molecular systems.

First of all, we will be interested in the steady-state electroluminescence (under continuous excitation) as a function of the tunnelling current. As it will be shown in Chapters 4 and 5, the

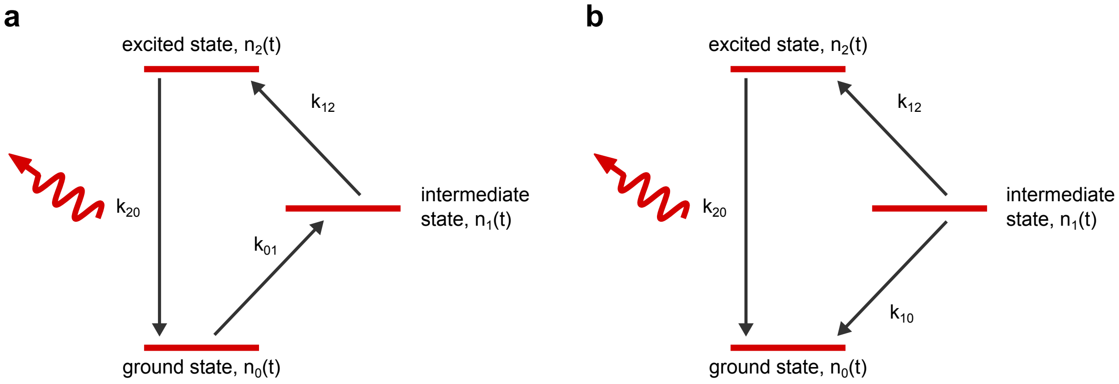

Figure 3.4 – Variations of the three state model. a) A continuous excitation b) A decay from the intermediate state.

tunnelling current (I) and the k_{01} rate are bound by the following dependency:

$$k_{01} = \frac{I}{\alpha e} = \frac{1}{\alpha \tau_{tunnel}} \tag{3.29}$$

Where α is a dimensionless parameter describing the efficiency of electrical pumping, e is the elementary charge and τ_{tunnel} is the average time between charges in the tunnelling current. The steady-state electroluminescence can be then obtained in the following way:

$$P(I) = lim_{t\to\infty} P(t) = \eta \frac{k_{01}k_{12}k_{20}}{k_{01}k_{12} + k_{12}k_{20} + k_{20}k_{01}} = \eta \frac{\frac{I}{\alpha e} k_{12}k_{20}}{\frac{I}{\alpha e}(k_{12} + k_{20}) + k_{12}k_{20}} \tag{3.30}$$

As we will see in Chapters 4 and 5, the experimental observations request the presence of a non-radiative quenching mechanism parallel to the k_{20} process that we label k'_{20}. In the denominator of eq. 3.30 we shall replace k_{20} by $k_{20} + k'_{20}$:

$$P(I) = \eta \frac{\frac{I}{\alpha e} k_{12}k_{20}}{\frac{I}{\alpha e}\left(k_{12} + k_{20} + k'_{20}\right) + k_{12}\left(k_{20} + k'_{20}\right)} \tag{3.31}$$

For a quenching mechanism that depends linearly on the tunnelling current we have (with β being the quenching efficiency):

$$k'_{20} = \frac{I}{\beta e} = \frac{1}{\beta \tau_{tunnel}} \tag{3.32}$$

We can simplify eq. 3.31 when assuming that the injection of the second charge (k_{12}) is very fast ($k_{12} \to \infty$), which results in a simple formula (replacing the tunnelling current with the

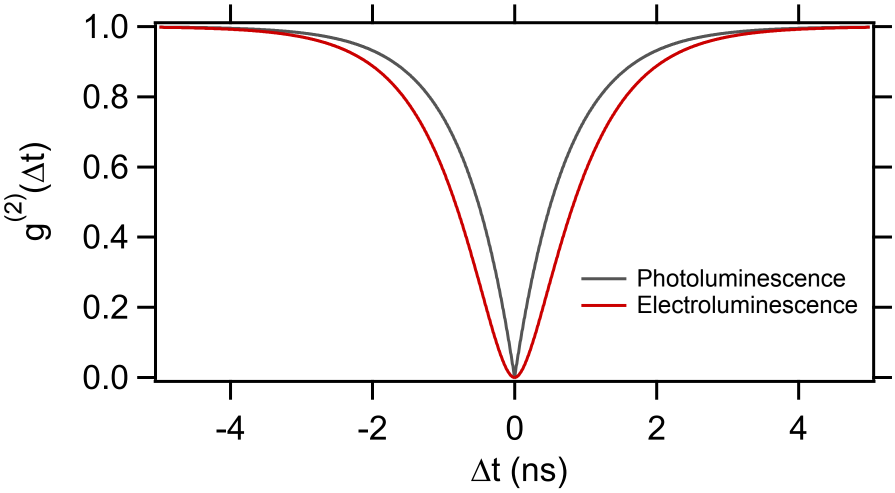

Figure 3.5 – Comparison of correlation functions for photo and electroluminescence. The values used to calculate the presented curves are discussed in the main text.

average time between consecutive charges as in eq. 3.29 und using eq. 3.32):

$$P(\tau_{tunnel}) = \eta \frac{\alpha}{\tau_{tunnel} + \beta\tau_{20}} \tag{3.33}$$

This equation describes the emission for low currents, *i. e.* when $\tau_{tunnel} \gg \tau_{12}$. When these two time constants become comparable, eq. 3.31 should be used, which describes a decrease of light intensity as a function of current due to highly efficient quenching (see Section 5.3). One has to note that here we assume that k_{12} is current (or tip-sample distance) independent which, as will be shown in Section 4.4, is only an approximation.

Photon correlations

Similarly to the two state model case, we can calculate the photon correlation function using eq. 3.19 and 3.28, which yields:

$$g^{(2)}(\Delta t) = 1 + \frac{S-Q}{2Q} e^{-\frac{S+Q}{2}\Delta t} - \frac{S+Q}{2Q} e^{-\frac{S-Q}{2}\Delta t} \tag{3.34}$$

We can now compare the correlation function obtained from the radiative decay, but excited either by light (two-state model, eq. 3.17) or by charge carriers (three-state model, eq. 3.34). We take realistic physical values: a low injection rate (τ_{01} = 100 ns), and an exciton lifetime of 0.75 ns [19] (τ_{10}, τ_{20}) for both models. For electroluminescence, we additionally need the injection rate of the second charge carrier τ_{12}, which we assume to be on the order of few hundred picoseconds (see Chapter 4), here τ_{12} = 0.3 ns. Fig. 3.5 shows $g^{(2)}(\Delta t)$ for these two cases calculated for the indicated parameters. It is clearly visible that in the case of electroluminescence, the obtained curve is broadened by the injection of the second charge being on the timescale comparative with the radiative lifetime, meaning that by measuring photon correlations in electroluminescence it is possible to obtain access to this process. Such an effect has been observed experimentally for single photon emitters in SiC [157]. For very fast τ_{12} (on the order of single picoseconds in this case) the electroluminescence curve converges to the photoluminescence curve.

Electroluminescence transients

The kinetic models can be used also to model electroluminescence transients - a measurement in which the rates of the processes can by dynamically changed by an external parameter (for instance by applying voltage pulses as in the set-up discussed in Section 2.4.3). Such dynamical changes require a proper adjustment of the boundary conditions:

$$\begin{aligned} n_0^b(t_{a\to b}) &= n_0^a(t_{a\to b}) \\ n_1^b(t_{a\to b}) &= n_1^a(t_{a\to b}) \\ n_2^b(t_{a\to b}) &= n_2^a(t_{a\to b}) \end{aligned} \tag{3.35}$$

Where $t_{a\to b}$ indicates the time at which the pulse ends and n_i^a are the populations of states i during the pulse (scheme in Fig. 3.4a). For clarity we will label respective populations and rates with ^{a} and ^{b}, as referring to Fig. 3.4. The measurements presented in Chapter 4 will show that the intrinsic dynamics of the system may toggle upon voltage pulsing between two schemes shown in Fig. 3.4a and b. For solving system presented in Fig. 3.4a we assume a full relaxation and thus the boundary conditions as described earlier in eq. 3.23. The master equation for the system in Fig. 3.4b is:

$$\frac{d}{dt}\begin{bmatrix} n_0^b \\ n_1^b \\ n_2^b \end{bmatrix} = \begin{bmatrix} 0 & k_{10}^b & k_{20}^b \\ 0 & -k_{10}^b - k_{12}^b & 0 \\ 0 & k_{12}^b & -k_{20}^b \end{bmatrix} \begin{bmatrix} n_0^b \\ n_1^b \\ n_2^b \end{bmatrix} \tag{3.36}$$

With the boundary conditions as above. Importantly, the three-state model in this configuration describes a decay to the ground state $n_0^b(t)$. Again, for the time-dependent light intensity (eq. 3.25), we are interested in the population of the excited state $n_2^b(t)$:

$$n_2^b(t) = \frac{n_1^a(t_{a\to b})k_{12}^b}{k_{20}^b - k_{12}^b - k_{10}^b} e^{-(k_{12}^b + k_{10}^b)t} + \left(n_2^a(t_{a\to b)} - \frac{n_1^a(t_{a\to b})k_{12}^b}{k_{20}^b - k_{12}^b - k_{10}^b} \right) e^{-k_{20}^b t} \tag{3.37}$$

With the following substitutions:

$$\begin{aligned}
\Omega &= k^a_{01} k^a_{12} k^a_{20} \\
S &= k^a_{01} + k^a_{12} + k^a_{20} \\
R &= k^a_{01} k^a_{12} + k^a_{12} k^a_{20} + k^a_{20} k^a_{01} \\
Q &= \sqrt{S^2 - 4R} \\
G &= \tfrac{k^a_{20} k^a_{01}}{R} \\
H &= -\tfrac{1}{2RQ^2} k^a_{01} \big(-2\Omega + {k^a_{20}}^3 - {k^a_{01}}^2 k^a_{12} - k^a_{01} {k^a_{12}}^2 - Q^2 {k^a_{20}}^2 + Q k^a_{01} k^a_{12} + \\
&\quad + R(-2k^a_{20} + k^a_{12} + k^a_{01} + Q) \big) \\
J &= \tfrac{1}{2RQ^2} \big(2R^2 + \Omega(k^a_{20} - k^a_{12} + k^a_{01} + Q) + k^a_{12}({k^a_{20}}^3 + Q {k^a_{20}}^2 + {k^a_{01}}^2 (k^a_{01} + Q)) + \\
&\quad - R({k^a_{20}}^2 + k^a_{01}(k^a_{01} + 2k^a_{12} - Q) + k^a_{20}(2k^a_{12} + Q)) \big)
\end{aligned} \tag{3.38}$$

One obtains:

$$\begin{aligned}
n^a_1(t_{a\to b}) &= G + H e^{\frac{-(S+Q)}{2} t_{a\to b}} + J e^{\frac{-(S-Q)}{2} t_{a\to b}} \\
n^a_2(t_{a\to b}) &= \frac{k^a_{01} k^a_{12}}{R} \left(1 + \frac{S-Q}{2Q} e^{-\frac{S+Q}{2} t_{a\to b}} - \frac{S+Q}{2Q} e^{-\frac{S-Q}{2} t_{a\to b}} \right)
\end{aligned} \tag{3.39}$$

We will employ this equations in Section 4.4. Similar analysis can be performed also for the case when just the values of the rate constants are changing and not the direction of transitions. In such a case the master equation 3.23, has to be solved using the boundary conditions shown in eq. 3.35. For long enough transition times ($t_{a\to b} \to \infty$) the steady-state conditions are reached and the boundary conditions can be simplified to:

$$\begin{aligned}
n^b_0(t_{a\to b}) &= n^a_0(t_{a\to b}) = \tfrac{k^a_{12} k^a_{20}}{R} \\
n^b_1(t_{a\to b}) &= n^a_1(t_{a\to b}) = \tfrac{k^a_{01} k^a_{20}}{R} \\
n^b_2(t_{a\to b}) &= n^a_2(t_{a\to b}) = \tfrac{k^a_{01} k^a_{12}}{R}
\end{aligned} \tag{3.40}$$

The solution has again the form of weighted exponentials (eq. 3.24). A system showing an evolution of that type will be presented in Section 4.4.1.

3.4 Conclusions

The analysis presented in this chapter shows that relatively simple models can efficiently capture the dynamics of individual nanoscale systems. First, we introduced the concept of photon statistics and the intensity correlation function. Subsequently, we showed that the correlation function may be analytically calculated using two and three state kinetic models. Apart from photon correlations, the solutions of these models allow the modelling of time-dependent and averaged luminescence intensity. The physical parameters that can be extracted using this approach include radiative and non-radiative transition lifetimes (exciton and charge dynamics) and time constants related to the motion of a molecule on the surface.

This kinetic analysis is not limited to the systems presented in this thesis but can be easily extended to processes such as alteration of emission modes, charging, exciton-plasmon correlations and intersystem crossing. However, for more complicated systems (with more degrees of freedom) numerical simulations of time-dependent luminescence can be of use since the resulting formulas become relatively complicated. Also, for a proper analysis of more complex effects such as interaction of an exciton with the plasmonic cavity, one has to employ proper quantum mechanical calculations, as for example time-dependent density functional theory [158].

4 Charge and exciton dynamics in C_{60} thin films[1]

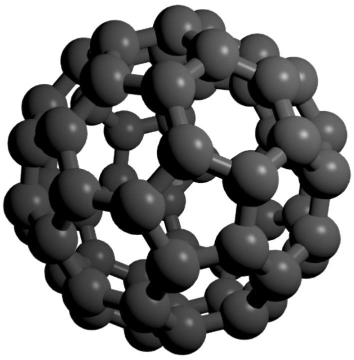

Figure 4.1 – C_{60} molecule

The family of carbon allotropes contains graphite, diamond, nanotubes and graphene as well as spherical forms such as C_{60}. This molecule contains 60 carbon atoms linked together into hexagons and pentagons forming a truncated icosahedron as presented in Fig. 4.1. Usually, C_{60} and other carbon cages, like C_{70} are referred to as buckminsterfullerenes or simply fullerenes due to their resemblance to geodesic domes designed by Richard Buckminster Fuller [159]. Since its discovery in 1985 [160], which led to a Nobel Prize in Chemistry for Harold Kroto, Robert Curl and Richard Smalley in 1996, the properties, structure and potential applications of C_{60} and its derivatives have been intensively studied. C_{60} is the most stable fullerene and can be easily chemically functionalized either by attaching different organic groups (exofullerenes) or by trapping atoms and molecules inside the cage (endofullerenes) [161]. Some of these compounds exhibit fascinating physical properties like ferromagnetism [162], superconductivity [163–165] and possible light-induced superconductivity [166].

Fullerenes and their derivatives play an important role in the field of organic electronics due to their robustness and established production process. They are used as electron acceptors in organic solar cells [167, 168] and in hole transporting materials [169] for organic light emitting diodes (OLEDs). Apart from applications in devices, structures based on C_{60} are excellent model systems for investigating fundamental processes occurring in organic materials, due to the symmetric arrangement and only one element involved (carbon). In this chapter, we will use C_{60} layers as a model system to study light-matter interactions at the nanoscale. We profit from electroluminescent defects appearing in C_{60} thin films to study the formation and recombination of a single exciton upon controlled injection of single charges revealing the real-space dynamics of charging.

---

[1] This chapter is based on a publication #6 from the publication list

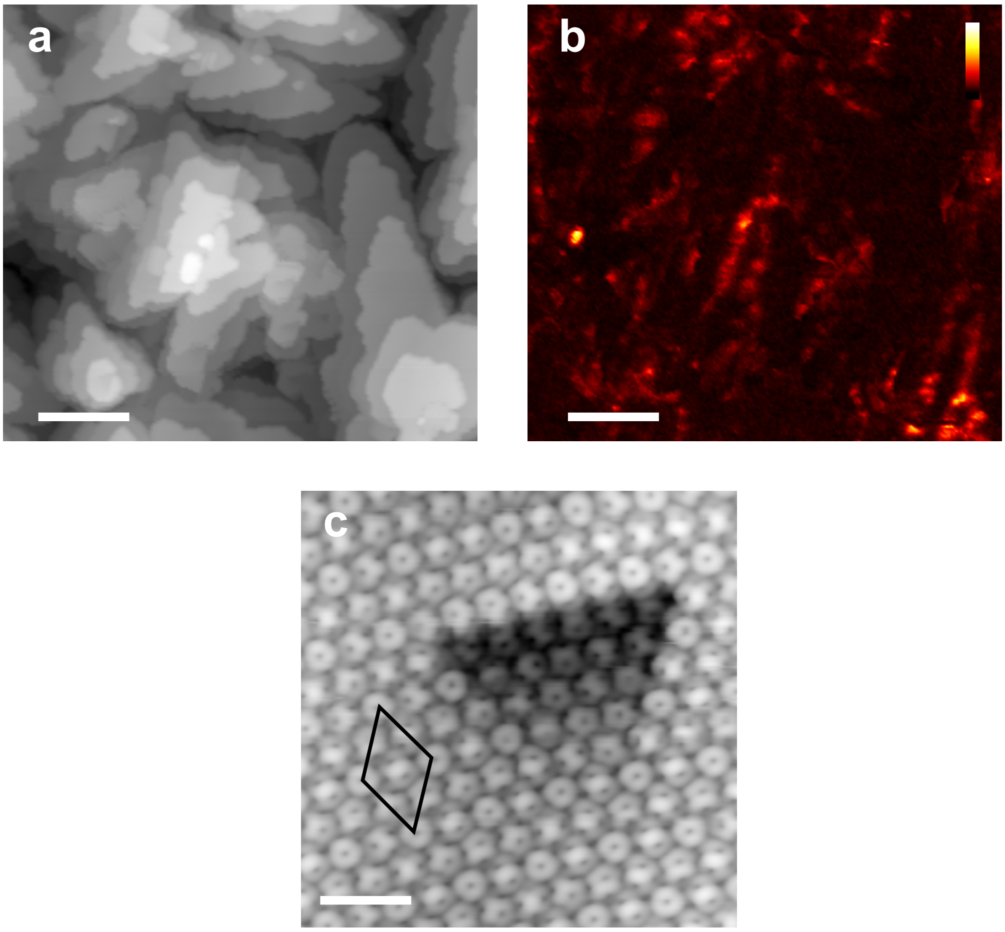

Figure 4.2 – Characterization of C_{60} multilayers. a) Constant current STM image of C_{60} grown on Au(111). b) Simultaneously recorded photon map. The false colour scale represents the light intensity 0 - 1.2 kcounts s^{-1}. Scale bars 40 nm. U = -3 V, I = 30 pA. c) Small scale image of a C_{60} thin film. The rhombus marks the elemental cell of the (2 × 2) superstructure. Scale bar 2 nm, U = -3.15 V, I = 50 pA.

4.1 Morphology and electronic properties of C_{60} thin films

C_{60} can be easily evaporated under UHV conditions and deposited on clean surfaces suitable for STM studies, due to its thermal stability. Soon after the synthesis of these molecules was developed enough to produce sufficient amounts, fullerenes were imaged with STM by Wilson *et al.*[170]. This study, along with the NMR, infrared and Raman spectroscopies, confirmed the predicted cage structure of C_{60}.

The structure and electronic properties of adsorbed C_{60} were studied on numerous metallic surfaces, for instance: Cu(111) [171–175], Pd(110) [176, 177], Ag(111) [178, 179] and Au(111) [170, 174, 178, 180–185]. As STM is capable of resolving orientations of individual C_{60} molecules, many of these studies focused on the adsorption configuration of C_{60} superstructures on surfaces. From bulk studies, it is known that solid C_{60} undergoes 2 phase transitions occurring at 260 K and 90 K [186]. At temperatures above 260 K, the molecules rotate freely within the crystal, whereas below 90 K the rotations are completely frozen and C_{60} resides in one of two possible orientations. In the case of sub-monolayers imaged with STM at liquid helium temperatures, even more orientations can be observed due to the interaction with the substrate [183]. For multilayers at low temperatures, the upper layers are sufficiently decoupled from the substrate and retain the hexagonal (2 × 2) superstructure of the bulk crystal (face-centred cubic structure) [106, 187, 188]. A constant-current image of such multilayers grown on an Au(111) substrate is shown in Fig. 4.2a. During growth, the substrate is first covered by a full monolayer, on top of which the next layers nucleate and grow independently leading to a formation of pyramid-like structures. Fig. 4.2c shows a small scale image of the thin film. The molecular orientations are clearly visible with the "doughnut"-like molecules being C_{60} cages rotated such that the hexagon ring is pointing upwards and the titled molecules with the hexagon-hexagon bond pointing upwards. The (2 × 2) superstructure is marked with a rhombus and has vortices in the positions of the "doughnut"-like molecules.

C_{60} in the gas phase has a HOMO-LUMO gap of 4.9 eV as defined by the difference of the experimental ionization energy and electronic affinity [189]. In the solid, due to the screening by the charge carriers located on the neighbouring molecules [185], this value is reduced to 3.7 eV as obtained by photoemission spectroscopy and inverse photoemission spectroscopy [190] and for monolayers on metallic substrates it can decrease to 2.1 eV for Au(111) and 1.2 eV for Ag(111) as found with STS measurements [178]. Monolayers on those substrates are subject to a charge transfer from the metal to the molecule, which is stronger for Ag(111) [191]. Additionally, the LUMO-derived band is located closer to the Fermi level than in the case of Au(111). However, some studies report that the charge transfer in the case of Au(111) is not significant [192]. In general, the monolayers on Au(111) and Ag(111) have a metallic character due to the hybridization with the supporting substrate (or direct tunnelling through the layer) and thus there is a measurable density of states between the HOMO and LUMO-derived bands [191].

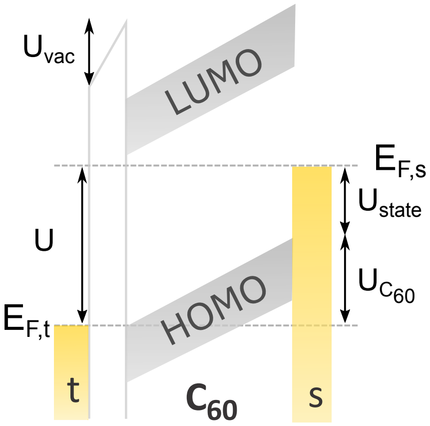

Figure 4.3 – Diagram of the electron potentials and states between tip and sample for the applied bias voltage U.

For thicker films grown on metal surfaces, the upper layers are sufficiently decoupled from the substrate and retain the electronic structure of the bulk. In the case of STM studies, one has to note that positions of HOMO and LUMO-derived bands measured by STS are affected by tip-induced band bending (TIBB). This effect is similar to the band bending in heterojunctions, with the difference that the electric field (in this case within the C_{60} layers) originates from the applied bias and is not due to space charge. Considering the STM junction as a voltage divider, U_{vac} as the voltage drop in the vacuum barrier, $U_{C_{60}}$ as the voltage drop in the fullerene layer, it must hold that the applied bias U = U_{vac} + $U_{C_{60}}$. The thicker the layer, the higher the relative voltage drop in the C_{60} layer. During an STS measurement, the respective HOMO and LUMO features appear when the bias compensates for the band bending in the film and the voltage drop in the vacuum barrier corresponds to the energy of the state: U = U_{state} + $U_{C_{60}}$, as illustrated in Fig. 4.3 [193]. Although the assumption of a linear potential (and thus constant electric field) in the C_{60} layer during STM measurement is not entirely correct, as it will be shown in section 4.2.3, it is sufficient for a first approximation analysis.

4.2 Radiative recombination of excitons at structural defects

4.2.1 Origin of C_{60} luminescence

Along with the topography presented in Fig. 4.2a we recorded a photon map (Fig. 4.2b). Most of the surface area is dark with few regions that exhibit detectable light intensity, usually around 1 kcts s^{-1} for tunnelling conditions of U = -3 V, I = 30 pA. In general, luminescence due to the radiative decay of excitons in C_{60} is very weak in both solution and bulk [194]. The reason for such weak luminescence lies in the highly symmetric structure of the isolated molecule. Its molecular character is also preserved in the bulk due to the weak van der Waals forces that bind the molecules together. When such crystals are excited (for instance by light), radiative transitions may occur if the selection rules are fulfilled. One important selection rule, known as Laporte rule [195] states that in centrosymmetric molecules (such as C_{60}) a radiative transition may take place only if the parity of the initial and final state is different. For C_{60}, both the first excited and ground state have gerade symmetry and thus the transition is forbidden [196]. However, this symmetry may be perturbed due to the Jahn-Teller effect [197], which leads to a local change of symmetry and a relaxation of the selection rule. Obviously, this interaction will be the strongest in the vicinity of structural defects and will lead to luminescence in the defected regions of the sample.

4.2.2 Nanoscale characterization of electroluminescence

Historically, many research groups studied the photoluminescence from C_{60} single crystals, however, the reported width and position of the emission lines varied depending on the samples, the illumination spots and temperatures [196, 198]. Some of the features could be assigned to impurities, such as C_{70} and the remaining ones were labelled as X traps. They are local emission centres of origin related to defects that are intrinsic to C_{60} (do not involve impurities), where perturbed Frenkel excitons (as assigned from the emission energy) are trapped and can radiatively decay [76, 196].

Such a system is therefore a natural candidate for STML measurements, which allow nanoscale characterization of luminescence and identification of the defects responsible for the emission. The first studies by Berndt *et al.* reported sub-molecular resolution in the light emission from monolayers of C_{60} on Au(110) [59, 199]. Later it was suggested that since the molecules are not sufficiently decoupled from the metal substrate, the molecular electronic structure hybridizes with that of the metal and the emission has a plasmonic character [200–202]. The first clear excitonic luminescence from C_{60}, as probed by STML, was presented by Ćavar *et al.* using C_{60} nanocrystals grown on NaCl/Au(111). In this study, the salt layer is used to decouple C_{60} from the metal [99]. This study was still lacking a correlation between light emission and local topography, which was provided only recently by our group [19, 76, 106].

Fig. 4.4 shows a pseudo-3D topography of a thin film, coloured with a simultaneously recorded photon map. In this region, there is a domain boundary between two independently growing C_{60} islands. Two bright emission centres (ECs) are located directly at the boundary. The ECs can be found also at other defects present in the crystal, like screw dislocations [19], in the vicinity of impurities [76] and on flat terraces due to subsurface defects and molecular orientational disorder [106]. Because the ECs are present at the structural defects, they can be identified as X-traps. If located at the surface, the defect states can be measured by STS and appear as DOS peaks in the bandgap. They can be identified as hole and electron traps that trap excitons as well [76, 106]. Otherwise, no spectroscopic features in the band gap are observed (Fig. 4.9e). The excitonic luminescence is recorded only at ECs, on other parts of the surface there is either no emission or a weak plasmonic emission is observed that will be discussed in the next chapter.

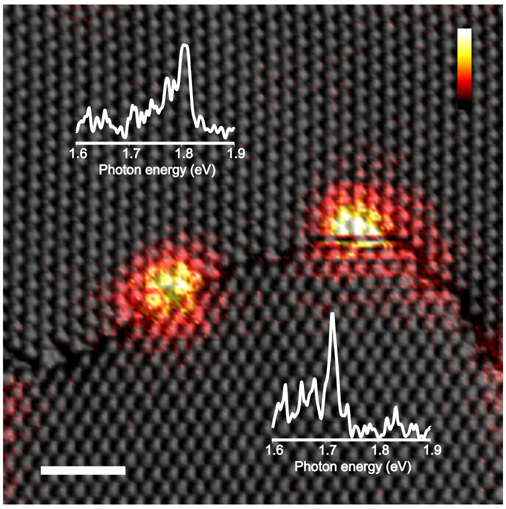

Figure 4.4 – Emission centres located at the domain boundary between two C_{60} islands. The topography is overlaid with the photon map (colour scale represents the intensity 0 - 2.1 kcounts s^{-1}). U = -3 V, I = 30 pA, scale bar 5 nm. Insets show optical spectra recorded at the two ECs, U = -3 V, I = 30 pA, integration time: 12 min for each spectrum.

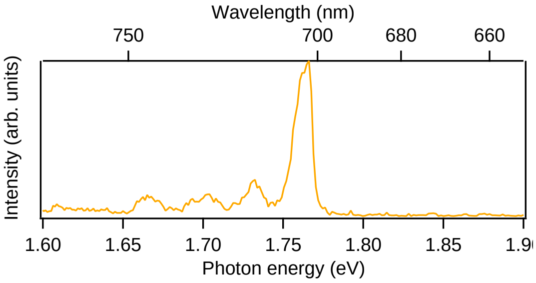

Figure 4.5 – Emission spectrum recorded on an EC. U = -3 V, I = 100 pA.

An electroluminescence spectrum recorded on one of the ECs is shown in Fig. 4.5. The main line is visible at the energy of 1.77 eV corresponding to a molecular $S_1 \rightarrow S_0$ transition of C_{60} and is accompanied by peaks with energy spacings (as measured with respect to the main line) that correspond to vibrational transitions of a single C_{60} molecule. It shows that indeed the emission is intrinsic. The energy of the main line is different for every EC (see insets in Fig. 4.4) and falls in the range between 1.66 eV and 1.81 eV (right

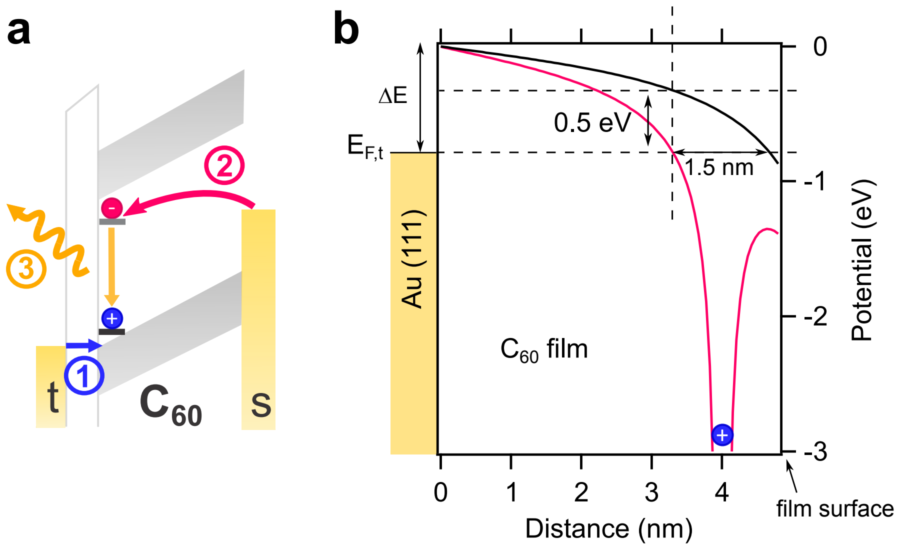

Figure 4.6 – Mechanism of the electroluminescence from the emission centres. a) Energy scheme illustrating the sequence of exciton formation and recombination: 1 - hole injection, 2 - electron injection, 3 - exciton formation and recombination. b) The electric potential within the C_{60} film calculated for bias $U = -2.93$ V with (magenta curve) and without (black curve) a trapped hole. The STM tip, approximated as a sphere, is assumed to be on the right side at a distance of 0.5 nm from the C_{60} surface. The presence of the hole lowers the potential barrier for electron injection (ΔE) within the C_{60} film by around 0.5 eV. As a result, the tunnelling distance for the electron is shortened by 1.5 nm.

below the limit of the bulk Frenkel exciton), the energies of the vibrational peaks are then shifted respectively. At a given EC, the emission energy is independent of bias, current and tip position [76]. The spatial extent of the ECs is related to charge injection to the defect state and will be further discussed in Section 4.5.

4.2.3 Electroluminescence mechanism

The electroluminescence described above can be analysed using the three-state model introduced in Section 3.3. At the ECs an exciton is formed due to injection and subsequent trapping of a hole and an electron, a mechanism shown in Fig. 4.6a. At high enough negative voltages (near -3 V) the hole injection into the HOMO-derived band becomes possible due to the TIBB (blue arrow). At this point, any shallow traps located in the bandgap of C_{60} will be populated resulting in local hole trapping. Such trapped charge strongly changes the potential in the C_{60} layer and shifts an electron trap state located close to the LUMO-derived band below the Fermi level of the substrate thus enabling electron injection. Once this occurs (magenta arrow) the exciton can be formed and may radiatively recombine (yellow arrow).

The exciton could in principle be formed in a process when the electron is injected as the first charge. However, such electron tunnelling to the LUMO-derived states would result in

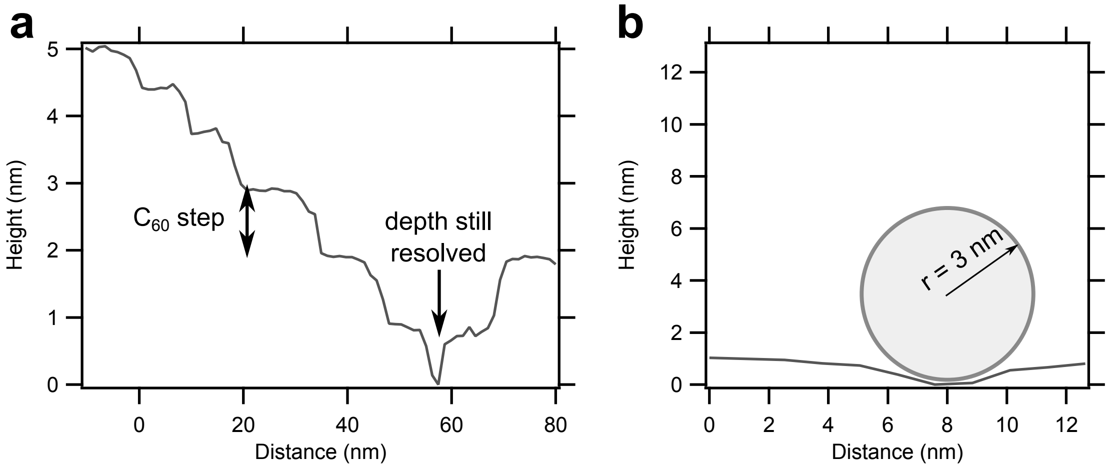

Figure 4.7 – Tip radius estimation. a) 80 nm profile of a C_{60} layer, the steps between the layers are clearly resolved (0.8 nm). b) 12 nm long profile along a C_{60} step, the circle indicates the maximum tip radius that enables resolving such a feature.

further tunnelling to the tip and may thus be identified by the appearance of an additional plasmonic photon emission channel from inelastic tunnelling. While there are cases when such plasmonic emission is observed (see Chapter 5), only ECs that do not exhibit plasmonic emission are selected for studies focusing on solely excitonic processes, as presented in this chapter.

To further confirm the mechanism presented in Fig. 4.6a, we calculated the potential within the C_{60} layer with and without a trapped hole, which is shown in Fig 4.6b. We used the image charge method treating the C_{60} thin film as a homogeneous medium with a dielectric constant $\epsilon = 4.4$ [161] located between the metallic substrate and tip (separated by a vacuum gap). The thickness of the film corresponds to six C_{60} ML (4.8 nm), the vacuum gap is assumed as 0.5 nm. The estimated tip radius (r = 3 nm) is consistent with its ability to resolve sharp steps and deep valleys. A tip with a larger radius would not allow resolving the narrow valley with precision shown in Fig. 4.7b - the C_{60} layer depth would appear shallower than the expected 0.8 nm (Fig. 4.7a). To determine the field in a self-consistent way we place image charges at the tip, in the vacuum, C_{60} layer, and metal substrate. We iterate the calculation by adding image charges of image charges until the boundary conditions (continuity of potential) at all interfaces converge. As expected for a round electrode (tip), the calculated potentials are non-linear. The geometry used here is closer to the real conditions during a measurement and shows that the plate-capacitor model (with linear potential) can be used only as in the first order analysis of the system. The position of the LUMO-derived band with respect to the Fermi level of Au(111) is 0.8 eV [203].

The calculated 1D potential shows that the presence of the hole lowers the LUMO-derived states by about 0.5 eV pulling the electron trap level below $E_{F,s}$ only in the presence of a hole. This further suppresses the reverse injection sequence. However, for Ag(111) the LUMO is located closer to the Fermi level of the metal [191, 193], which may result in band bending such that for the same conditions (voltage, current, tip) the LUMO in upper layers is located below the Fermi level even without charging the defect with a hole. In such a situation two injection sequences, electron → hole → exciton and hole → electron → exciton may be operant and compete.

4.3 Exciton recombination dynamics

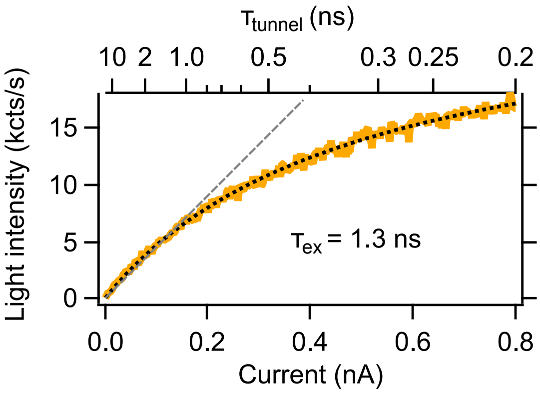

Figure 4.8 – Light intensity as a function of current. The dashed line shows the fit to the equation 4.2 yielding τ_{ex} = 1.3 ns. U = -3 V. The gray line is plotted to emphasize the sub-linear characteristics of the measured curve.

A single emitter produces photons one-by-one, such that the shortest time interval between detection of two photons is limited by the exciton lifetime. Our group showed earlier that this is the case for ECs in C_{60} thin films, which are single photon emitters [19]. Such a measurement is performed in the HBT-STM configuration (see Section 2.4.3) and the measured correlation function has a dip at zero time delay, which can be used to estimate the exciton lifetime. For ECs the radiative lifetime (τ_{ex}) is close to 1 ns. When probed as a function of current, the lifetime decreases as a result of exciton-charge annihilation, a process often observed in OLEDs [26, 204]. This annihilation becomes observable when the lifetime of the exciton is comparable to the average time between injected charges τ_{tunnel}, which can be calculated using the definition of electrical current, as in eq. 3.29:

$$\tau_{tunnel} = \frac{e}{I} \tag{4.1}$$

Where e is the elementary charge. As an example, a current of 160 pA corresponds to on average 1 ns between two injected charges. A hole can interact with the exciton within its lifetime of comparable value (1 ns) and result in a non-radiative quenching of the electron-hole pair.

Apart from the lifetime reduction, the exciton-charge annihilation also lowers the electroluminescence yield at high currents as presented in the light intensity versus current curve P(I) (Fig. 4.8). The observed characteristics deviates from linearity (constant yield) due to the annihilation effect. Such behaviour can be modelled with a kinetic rate model (Chapter 3) and in the simplified version (see eq. 3.33) renders the following dependence of the light intensity vs. the tunnelling current:

$$P(\tau_{tunnel}) = \eta \frac{\alpha}{\tau_{tunnel} + \beta\tau_{ex}} \tag{4.2}$$

Where α, β, η are hole trapping probability, annihilation probability and detection efficiency. Fitting the data in Fig. 4.8 to the equation 4.2 with $\alpha = 10\%$, $\beta = 10\%$ and $\eta = 10^{-5}$, which are values obtained from previous photon-photon correlation measurements [19], yields $\tau_{ex} = 1.3$ ns, which agrees with the value acquired by using HBT-STM (0.75 ns). Therefore, this method involving leveraging this reciprocal relation (eq. 4.1) can be used to estimate the radiative lifetime in a simple methodology, without performing challenging correlation measurements.

4.4 Exciton formation dynamics

The dynamics of processes taking place in OLEDs is obtained by measuring the time-resolved electroluminescence response to an applied short voltage pulse [169, 205–207]. Effects that can be studied using this method include: charge transport [206], singlet quenching [207] and delayed fluorescence [208]. Although this method serves as a useful tool for modern technology, it obscures the processes occurring at the scale of individual charges and excitons. Therefore, it is highly desirable to scale this technique down to the molecular regime using time-resolved STML (TR-STML). As it will be shown in this section, adapting this approach to an EC in C_{60} gives access to single exciton formation dynamics with sub-molecular precision.

TR-STML is based on applying voltage pulses with 1 ns edges (10%-90%), shaped such that all imperfections of the STM wiring are compensated and pulses arriving at the tunnel junction are rectangular. Technical details of TR-STML can be found in Section 2.4.3. Such an excitation method allows efficient toggling between the on and off state of the EC. As mentioned earlier, the luminescence appears when the voltage is close to -3 V. This onset and the unipolar emission is presented in Fig. 4.9d,f. At voltages less negative than -2.7 V the Fermi level of the tip ($E_{F,t}$) lies in the bandgap of C_{60}, making the charge injection impossible. Changing the voltage by more than 0.2 V shifts the $E_{F,t}$ into the HOMO-derived band, the tunnelling current flows and light is emitted. Therefore, to switch the luminescence on and off it is sufficient to apply a voltage pulse of amplitude higher than 0.2 V and offset at -2.7 V. In the experiment we apply -0.3 V pulses at -2.63 V offset. The time characteristics are presented in Fig. 4.9b (magenta trace). The orange trace in Fig. 4.9b shows the time-resolved luminescence response of the EC. The light intensity raises slowly, reaching steady-state conditions after 25 ns. When the pulse is over, $E_{F,t}$ lies again in the bandgap. However, the luminescence does not vanish immediately but decays in an exponential fashion with a characteristic time of 30 ns. The origin of the observed time constants will be discussed later and will be shown to arise from the processes leading to the exciton formation.

The electroluminescence transients presented in Fig. 4.10 are measured on the brightest

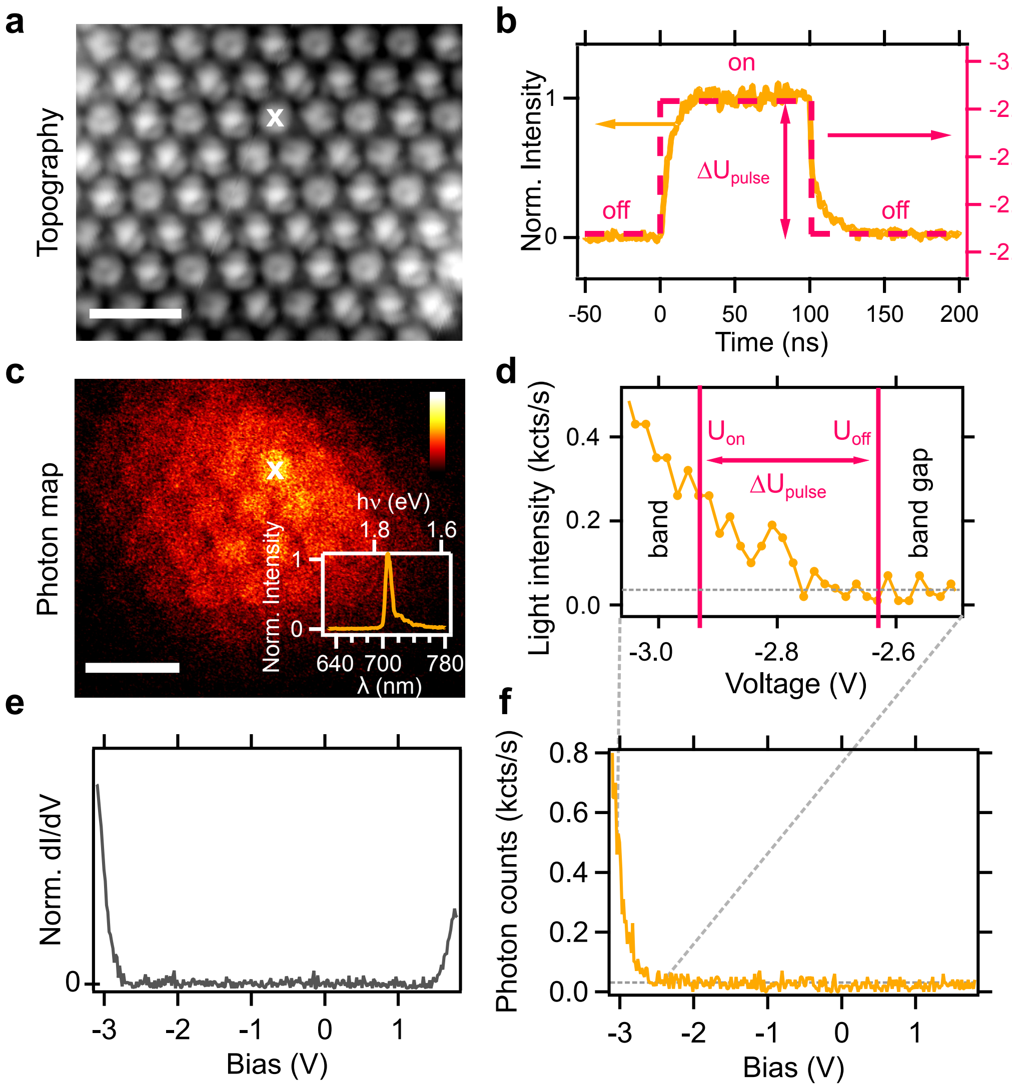

Figure 4.9 – Characterization of an EC. a) Constant-current STM image of the C_{60} layer, U = - 3 V, I = 50 pA. Scale bar 2 nm. b) Time-resolved electroluminescence response (yellow points) to the applied voltage pulse (magenta dashed line). c) Electroluminescence photon map recorded simultaneously with the image presented in a). The false colour scale represents the light intensity 0 - 5.3 kcounts s^{-1}, white scale bar 2 nm. The inset shows the light spectrum recorded at the position marked by a cross, U = - 3 V, I = 700 pA. d) Luminescence vs. bias voltage function measured at the position marked by a cross in a) and c). The magenta vertical lines indicate bias voltages during the pulse (U_{on}) and in between pulses (U_{off}). U_{on} = - 2.93 V, U_{off} = - 2.63 V, $\Delta U_{pulse} = -0.3V$. e) Scanning tunnelling spectroscopy showing the band-gap on the C_{60} thin film. f) Full range spectrum from Fig. 4.9d. Spectra d)-f) were recorded for the following set-point: U = -3 V, I = 5 pA. The gray horizontal dashed lines in d) and f) indicate the dark counts of the detector (30 cts s^{-1})

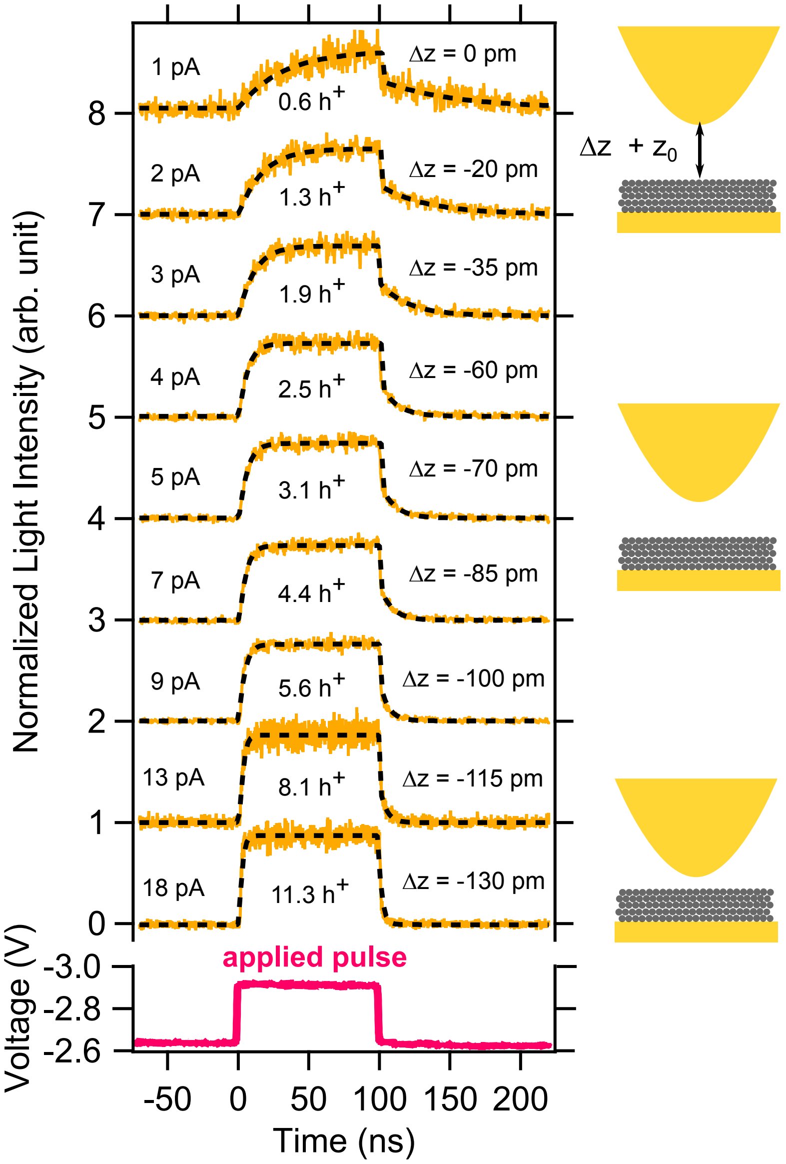

Figure 4.10 – Light transients as a function of the vertical position. The absolute tip-sample distance is defined as z = z_0+Δz, where z_0 is the (unknown) tip-sample distance at the set-point U_{on} = - 2.93 V and 1 pA tunnelling current (top trace). Traces are vertically offset for clarity. Each trace is labelled from left to right by the following parameters: I for corresponding z at U_{on}, the average number of holes injected during one pulse (Q=It_{pulse},t_{pulse}=100 ns), and the distance change Δz with respect to the experimental conditions of the top trace. The dashed lines are fits to the model described in the main text. Bottom: Applied pulse shape (magenta trace) measured by plasmonic emission on a clean Au(111) surface shown to highlight the difference between itself and the luminescence response. The cartoon on the right shows the reduction of z during the measurement (not to scale).

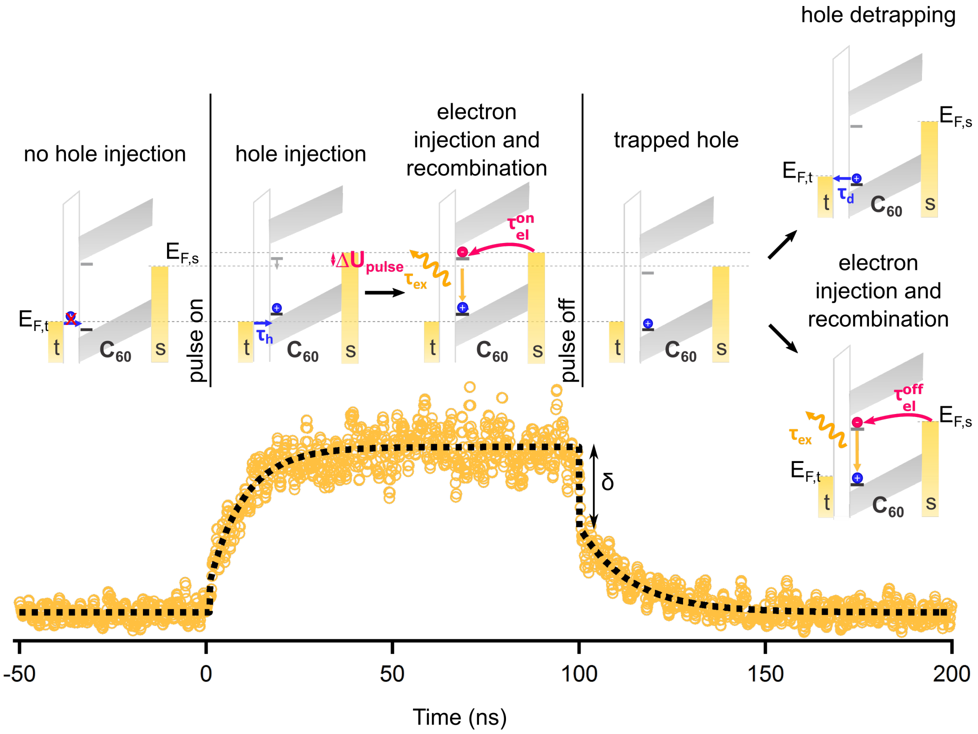

Figure 4.11 – The model of charge and exciton dynamics at the EC during transient measurement. The energy diagrams show the system in different stages of the measurement (before the pulse arrives, during pulse duration time, after the pulse). Details of the model are described in the main text. Below the energy diagrams, a representative transient (orange markers) is presented, the dashed line shows fit to the equation 4.3 described in the main text.

point of the EC (cross in Fig. 4.9c) at a stabilized tip-sample distance (z), which defines the tunnelling current and the electric field in the system. By varying z we change both parameters and control the dynamics of the system. The topmost trace is recorded at the furthest distance and used as a reference (z_0), the consequent traces are measured when the tip approaches the surface (negative Δz). With decreasing z, the EC is more intensely pumped and the light intensity increases. The influence of z on the dynamics is clearly visible: the closer the tip approaches to the surface, the steeper become the edges of the transient, indicating faster dynamics. The I-V characteristics measured for each tip-sample distance allows us to determine the current during the pulse and therefore the number of injected charges during the pulse. In the measurements shown in Fig 4.10, this value ranges from 0.6 (top trace) to 11.3 holes (bottom trace), proving that our study probes the single charge-single exciton regime. The value of the current also determines the hole injection rate (a reciprocal of the time between charges, as defined in eq. 4.1) using $\frac{1}{\tau_h} = \frac{I}{\alpha e}$. For $\alpha = 10\%$ τ_h is beyond 1 μs at the lowest currents (on the order of single pA).

The analysis of the transients can be split into three regimes, before, during, and after the pulse (Fig. 4.11). Before the pulse arrives at the tunnel junction (leftmost diagram), the Fermi level to the tip lies in the bandgap of the thin film (U_{off}), which results in the absence of charge injection and photon emission. When the applied voltage switches to U$_{on}$, E$_{F,t}$ shifts below the HOMO-derived band edge, permitting a hole to be injected into the defect state (middle diagram) with a time constant τ_h. The trapping of the hole shifts the electron trap below the Fermi level allowing an electron to be injected (τ_{el}^{on}) from the Au(111) substrate. Once this occurs an exciton is formed and decays radiatively within its lifetime τ_{ex}. While the pulse is on, this process may, in principle, repeat. After 100 ns the pulse ends, the voltage returns to U$_{off}$, therefore energy-level-wise the situation is the same as before the pulse. The luminescence still remains for a significant time (right side of Fig. 4.11). We know that the hole injection is no longer possible because as E$_{F,t}$ lies again in the band gap. The exciton lifetime (1.3 ns) obtained from Fig. 4.8 is too short, therefore the electron injection from the substrate is the only remaining process that can be responsible for the slow luminescence time constant. A similar analysis holds for the rising edge of the pulse (the hole injection is in the μs range as discussed earlier) and shows that our measurements are sensitive to the electron injection rate. In general, the process of exciton creation after the pulse requires the presence of a hole that was injected during the pulse but did not yet recombine. The hole still shifts the electron level below E$_{F,s}$, so that the electron injection is still possible (τ_{el}^{off}), even though the applied voltage is lower (see Fig. 4.6). As previously, this leads to exciton creation followed by recombination. However, this is not the only possible process for the remaining hole. E$_{F,t}$ at U$_{off}$ is located above the defect state, therefore there is a non-zero probability that the trapped hole tunnels to the tip, resulting in detrapping (τ_d). This process contributes to the electroluminescence quenching after the pulse.

Recent STML studies on single molecules report molecular luminescence due to energy transfer from plasmon modes excited in the junction [97, 109–111]. This would suggest that the coupling between tunnelling current and exciton formation occurs on the femtosecond time scale of plasmon lifetime [93]. By contrast, the nanosecond electroluminescence dynamics of ECs proves that the C$_{60}$ excitons originate from the binding of two charges of opposite sign taking place in the molecular layer.

The sketched dynamic behaviour can be cast into a quantitative shape by a three-state rate equation model as shown in Chapter 3 to obtain time-dependent light intensity P(t) that takes the following form for the three regimes observed in the experiment:

$$P(t) = \begin{cases} 0 & \text{if } t < 0 \\ \eta k_{ex} n_{ex}^{on}(t) & \text{if } 0 < t < t_{end} \\ \eta k_{ex} n_{ex}^{off}(t) & \text{if } t > t_{end} \end{cases} \tag{4.3}$$

With t_{end}, η, k_{ex}, $n_{ex}^{on}(t)$, and $n_{ex}^{off}(t)$ being the length of the pulse (100 ns), detection efficiency, exciton decay rate $k_{ex} = \frac{1}{\tau_{ex}}$, and exciton populations during and after the pulse respectively. The explicit forms of the exciton populations that depend on the 5 rate constants $\left(\frac{1}{\tau_{ex}}, \frac{1}{\tau_h}, \frac{1}{\tau_d}, \frac{1}{\tau_{el}^{on}}, \frac{1}{\tau_{el}^{off}}\right)$ can be found in Section 3.3. Two of the rates are known from earlier

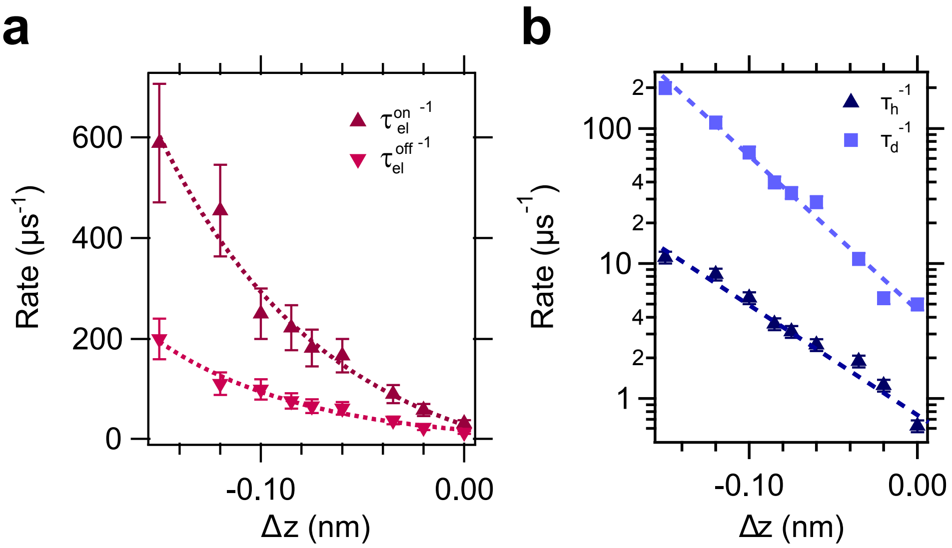

Figure 4.12 – Rates as a function of tip-sample distance obtained from the fits to the model. a) Electron injection rates during (triangles) and after the pulse (diamonds). b) Hole injection (triangles) and detrapping rates (squares).The hole trapping efficiency is included in the hole injection rate. Dashed lines are guides to the eye (exponentials)

measurements; the exciton decay $\frac{1}{\tau_{ex}}$ and the hole injection rate calculated from the current during the pulse $\frac{1}{\tau_h} = \frac{I}{\alpha e}$. The hole trapping efficiency α must lie between 1 and 10^{-4}. The minimal value is based on the fact that the experimentally detected light intensity is above the background and is calculated from the luminescence efficiency. Since not every injected hole is trapped, α has to be below 1. Here we assume $\alpha = 0.1$. As a result, there are only 3 free parameters in the fit $\left(\frac{1}{\tau_d}, \frac{1}{\tau_{el}^{on}}, \frac{1}{\tau_{el}^{off}}\right)$ that can be extracted from the shape of the transient. In principle, the transient is also described by 3 independent parameters, namely, the rising and falling edge time constants, and the immediate falloff marked as δ in Fig. 4.11. δ is determined by the $\frac{\tau_{el}^{off}}{\tau_{el}^{on}}$ ratio. It appears quasi-instantaneous (< 2 ns) since the change of the time constant for the electron injection ($\tau_{el}^{on} \rightarrow \tau_{el}^{off}$) occurs within 1 ns (time-resolution limit defined by the edges of the pulse) and the decay time of an exciton is also on the order of 1 ns. The measured traces can be fit using P(t) (dashed lines in Fig. 4.10) and a set of of time constants for every z value can be extracted. We find that the hole injection (τ_h) is the slowest process (90-1600 ns), limiting the exciton population, influencing mostly the light intensity and having a negligible effect on the transient shape. The resulting time constant $\frac{\tau_h}{\alpha}$ becomes long (in the μs range) and therefore α can even take values smaller that 0.1. The electron injection (τ_{el}) is a faster process (2-31 ns during the pulse and 5-68 ns after the pulse), but is slower than the exciton decay (τ_{ex}). The detrapping time (τ_d, 5-200 ns) has a small effect on the fits and follows an exponential dependence versus z (Fig. 4.12b), which is consistent with our interpretation of the hole tunnelling back to the tip. At elevated currents, above 10 pA during the pulse, the charge dynamics of the system becomes fast and the response becomes increasingly rectangular, with slightly rounded edges because under these experimental conditions, the exciton lifetime τ_{ex} = 1.3 ns is comparable to the rise time of the voltage pulses (1 ns). The exciton lifetime is here considered constant, since the exciton-charge annihilation process reduces the lifetime significantly only at currents above 100 pA (see Fig 4.8).

Fig. 4.12a presents the electron injection rates obtained by fitting the model to the transients as a function of z. The electric field in the thin film is approximately linear with the tip-sample separation. Therefore, the observed non-linear dependence of $\frac{1}{\tau_{el}^{on}}$ and $\frac{1}{\tau_{el}^{off}}$ on Δz in Fig. 4.12a confirms the presence of an energy barrier at the interface resulting in a non-ohmic character of the Au(111)/C_{60} junction. Subsurface defects (e.g. roughness of the Au(111) surface) and hidden interface dynamics (e.g. interface dipoles and charge transfer) are the factors affecting the injection at the interface [209, 210].

We have measured TR-STML curves at different emission centres and observed similar behaviour. However, no clear dependence could be derived as the charge dynamics strongly depends on the thickness, the electronic surroundings, and the roughness of the supporting metal surface. Also, some of the EC have dynamics faster than the measurement resolution (1 ns) even at the largest tip-sample separations, which may be due to an electron trap being located deeper in the band gap or locally enhanced band-bending, both of which facilitate electron injection. Charge injection may be also affected by substrate engineering - in the case of measurements on Ag(111) presented in the previous PhD thesis of C. Große [193] it was shown that the electron trap may be populated without the presence of the hole (as discussed in section 4.2.3), a process that results in an overshoot in the transient measurements. Such overshoot was not reproduced on C_{60} grown on Au(111) substrate.

4.4.1 Measurements within the HOMO-derived band

TR-STML measurements are not limited to on-off measurements but can be also applied to probe dynamics at different voltages within the HOMO-derived band, as shown in Fig 4.13. As for the measurements where the hole injection is switched on and off, the information about system dynamics is embedded in the edges of the transient. In order to model these measurements a slightly different model than the one presented above has to be used. Since the charge injection occurs also in between pulses, respective rate equations describing the system change (see Section 3.3). As derived from fits to this model, the injection at higher bias (electric fields) occurs faster (see values in Fig. 4.13), similarly to the case described earlier.

The advantage of these experiments lies in the increased light intensity at higher bias (see Fig. 4.9f) and therefore shorter measurement time and improved statistics. Although the P(V) curve can be used here to the advantage of the experimentalist, one issue has to be noted. In the case of a non-monotonic behaviour of P(V) in the range of applied pulses, the measured transients may not directly reflect the system dynamics, but be distorted due to these non-monotonicities (see Section 2.4.3). Additionally, the average current during such measurements is usually high enough to maintain stable feedback and thus a constant tip-sample distance.

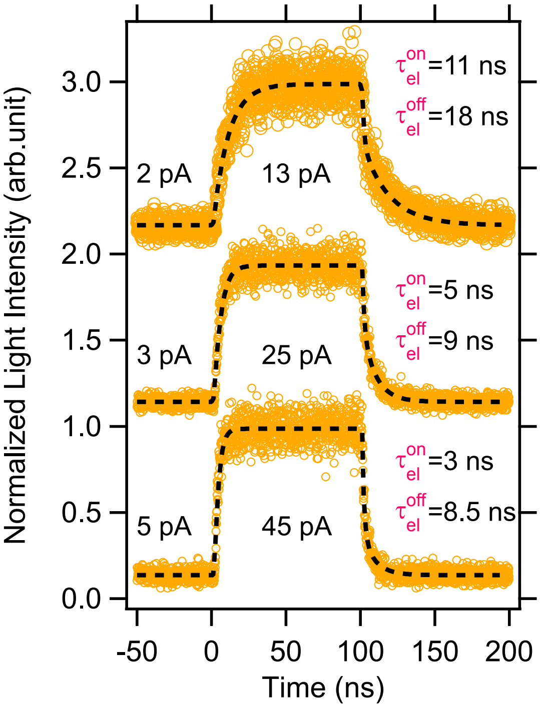

Figure 4.13 – Measurements within the HOMO-derived band. Currents during and after the pulses are indicated next to the traces. The black lines are fits to the model, as explained in the main text, the time constants obtained from the fit are listed on the right side of the traces. Traces are offset for clarity. U_{on} = -3.13 V, U_{off} = -2.83 V.

4.5 Four-dimensional imaging of single electron charging

The dynamics of single exciton formation as described above can be also understood as the dynamics of charging. Once the defect state becomes populated with a hole, a transient charged defect state is formed, which can be then neutralized by the injection of an electron. Charging effects in STM have been reported for single atoms [211–213], individual molecules [63, 214–217], defects in semiconductors [125, 127, 218–221] and 2D materials [222]. When the investigated object is stable in the charged state, its topographic appearance is changed as compared to the neutral form. For semiconductors, the spatial extent of topography protrusion is related to remote charging of the defect that changes the conductance in the vicinity. In dI/dV maps, charging appears as a ring-like feature [219, 222, 223]. The timescale of these processes is usually below the time resolution of the STM current amplifier and thus not accessible. Only recently, time-resolved studies reported spatially-resolved charging dynamics of dopants in semiconductors [16, 125, 127, 130]. However, time-resolved studies on molecular systems are still missing.

As reported in the previous section, the electron charge injection from the substrate to the defect state can be probed with ns time resolution as a function of the tip-sample distance - in the vertical dimension. This principle can be extended to the two lateral dimensions of the

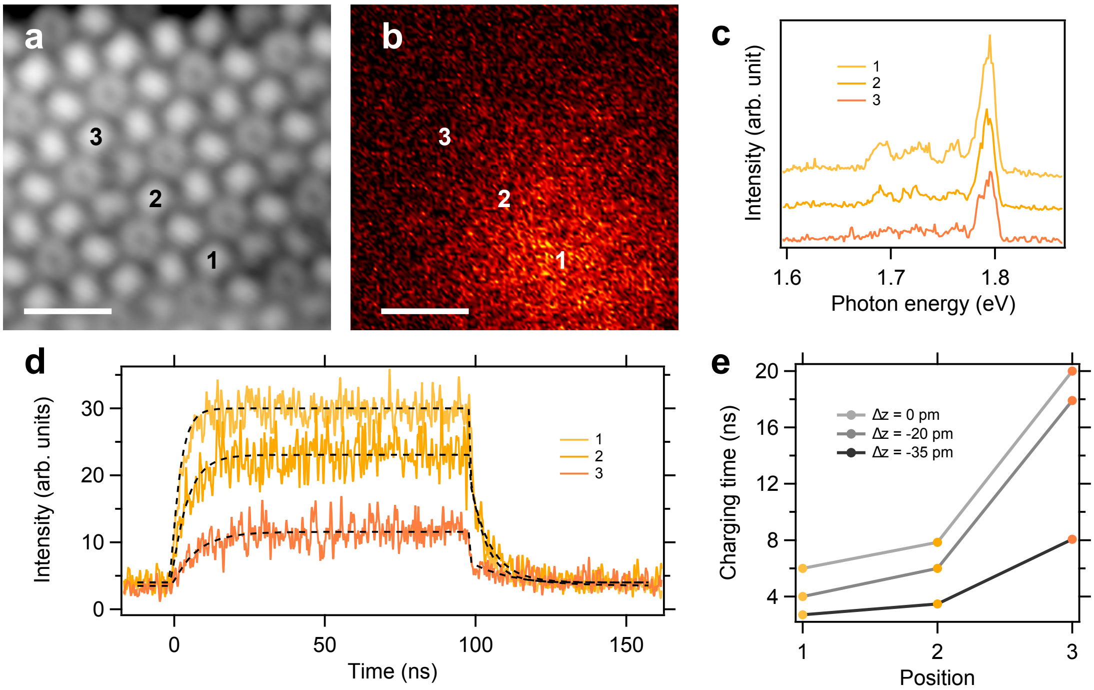

Figure 4.14 – Lateral dependence of charging time. a) Constant current image of a C_{60} layer. b) Simultaneously recorded photon map. Scale bars 2 nm. U = -3 V, I = 30 pA. c) Optical spectra recorded at positions marked in a) and b), U = -3 V, I = 30 pA. d) TR-STML transients measured at positions 1 to 3. Current during the pulse I_{pulse} = 12 pA, U_{on} = -2.83 V, U_{off} = -2.53 V. The dashed lines are fits to eq. 4.3. e) Charging (electron injection) time constants obtained from fitting a series of TR-STML measurements in pos. 1 to 3 for I_{pulse} = 12 pA (Δz = 0 pm), 20 pA (Δz = -20 pm), 37 pA (Δz = -35 pm).

surface comprising, together with the time domain, full nanoscale 4D imaging of molecular interfaces [224].

At first, we investigate in detail the spatial variation of the dynamics at the EC. Fig. 4.14a,b show the constant-current topography and the photon map of the sub-surface EC respectively. Three positions are marked, chosen such that the selected molecules are in the same orientation (hexagon-hexagon bond facing upwards). By doing so we assure that the DOS is the same for all of them [106] and a constant-current set-point will result in the same tip-sample distance. This is critical for comparing the respective dynamics, as the electron transfer rate is very sensitive to z (Fig. 4.10, electric field effect) and the orientation of individual C_{60} molecules. The emission spectra shown in Fig. 4.14c are constant - no Stark shift [101] is observed within the experimental accuracy. Only the emission yield decreases with the distance from the EC, which is also apparent in the photon map.

We measure the time-resolved luminescence of the EC at the marked positions using TR-STML and plot it in Fig. 4.14d. As observed directly from the measured transients, the charging rate determining in the rising and falling edges decreases when charge injection occurs farther from

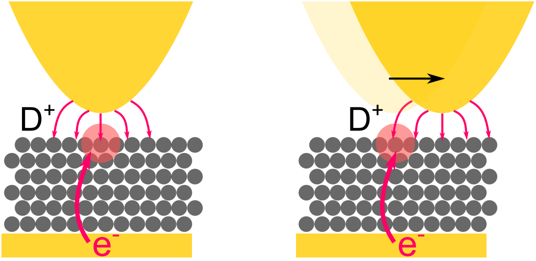

Figure 4.15 – Electric field at the defect site as a function of the lateral tip position.

the centre of the EC. We probe these dynamics for different tip-sample separations and find that the charge injection rate (Fig. 4.14e) consistently drops as we move away from the central molecule (1). As observed earlier, the charging rate increases when the tip-sample distance is reduced, which is attributed to an increase of the electric field and thus the reduction of the energy barrier at the C_{60}/Au(111) interface.

The observed reduction in the injection rate as a function of the distance from the central position of the EC can be rationalized by the electric field. We know that the detected light is formed in the hole trapping → electron injection → exciton formation and recombination process and that the electron and hole trap states have the DOS maximum in the central spot of the EC with a DOS decaying with the lateral distance [106]. Thus, when the tip is localized at the periphery of the EC, the hole can still reach the defect state and create a charged defect state D^+. For defects located in the subsurface layers, the apparent size (on the surface) of the EC will be larger than the size of the ECs located at the top layer, as the lateral distance from which the hole is injected into the defect state is increased. The reason for that is the fact that the hole transported deeper into the film may hop sideways (hexagonal stacking). The trapping probability (α) is reduced as compared to the central positions of the EC, which results in a lower electroluminescence yield. Once the defect is positively charged, the D^+ can be neutralized by an electron and from a neutral exciton. This charge injection is purely field driven (does not involve transport from the tip) and is induced remotely, similarly as in the previously reported charging studies [219, 221, 222]. However, the electric field induced by the tip located at the periphery will be reduced at the D^+ position, as shown schematically in Fig. 4.15, thus rendering a higher potential barrier for the electron injection from the substrate which impedes the neutralization process. As discussed before, a similar energy barrier increase is observed when the tip is retracted from the surface above the trap.

Such an increase in the observed time constant might be attributed to exciton diffusion. This process requires the electron-hole formation at some distance from the defect. It is however unlikely to occur because the free hole will not reside in the upper layers long enough to capture an electron. Moreover, the absence of the electron and hole traps requires even higher electric fields to sufficiently bend the LUMO-derived band below the Fermi level of the substrate. Finally, as shown in the previous section, the exciton lifetime is too short (1 ns) to directly observe its diffusion before it decays at the defect. In such a case, we would expect to

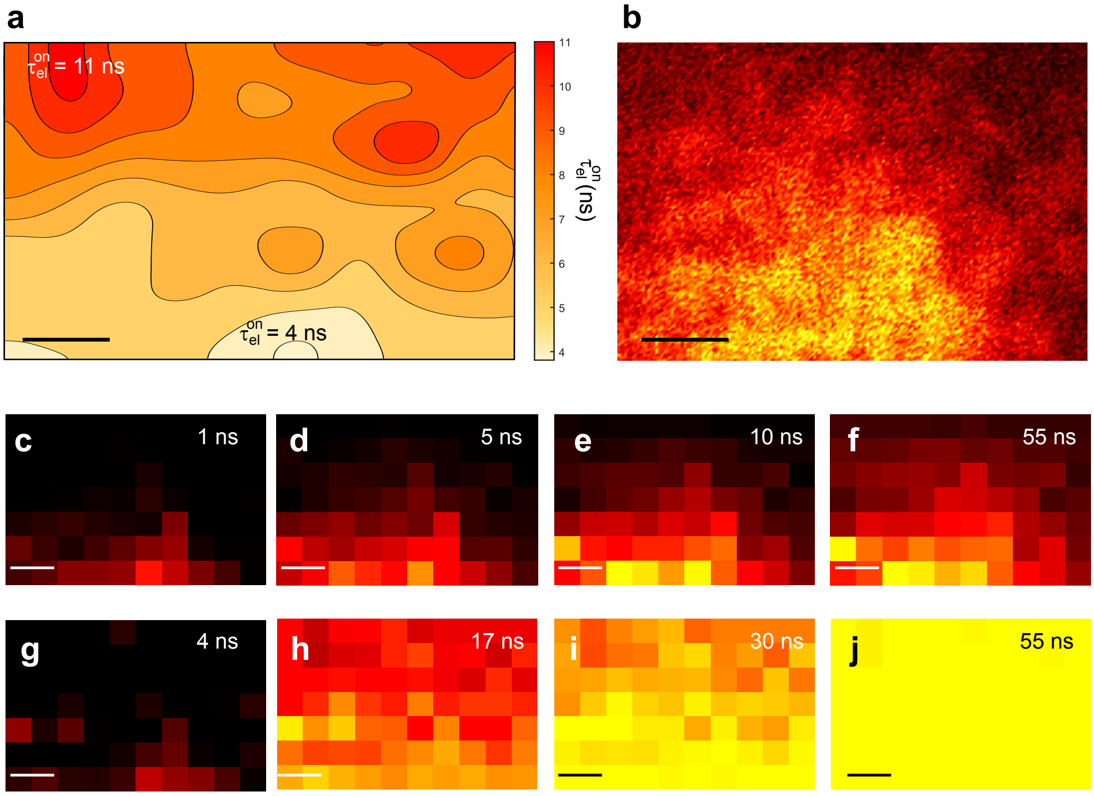

Figure 4.16 – Time-dependent light emission imaging. a) Map of charging time constants. The transient data were obtained on a grid of 7x10 points, fitted to the model described in the text, plotted on a grid and interpolated. b) Photon map (124x183 pixels) of the measured EC, U = -3 V, I = 30 pA c)-f) and g)-j) Light intensity maps retrieved from the time-dependent light intensity at the indicated times measured with respect to the pulse arrival. c)-f) are normalized to the maximum of the overall spatial intensity, g)-j) maps are normalized at each point to its respective maximum (reached at the steady-state) to highlight that the intensity maximum at the periphery is reached the latest. Due to a tip change, the last three points in the top row (right side) were discarded and approximated by the value of the last valid transient to maintain the proper scaling. Scale bars 1 nm. The total acquisition time of the time-resolved maps: 8h. U_{off} = -2.53 V, U_{on}= -2.83 V, I_{pulse}= 3.5 pA

observe an increase of the radiative lifetime, because the exciton radiative decay is strongly reduced at an ordered surface located at the distance from the EC. In a material with different properties (longer exciton lifetime and an allowed radiative transition) the method presented here could be used to study exciton diffusion in real time.

In the next step, we can directly map the charge transfer time as a function of position near an EC. To do so, we measure TR-STML transients on a 10x7 points grid (400 s integration time per point), fit each trace with the aforementioned model and plot the extracted electron charging time τ_{el}^{on} in Fig. 4.16a. This map can be compared with the spatial extension of the EC presented in Fig. 4.16b. As observed in an earlier measurement (Fig. 4.14), the charging time increases when the tip is located at the periphery of the EC. However, the change of the time constants is not spatially monotonic. These variations may be attributed to the local changes in the topography, electronic structure and the non-regular tip shape. To correct for the z drift of the STM tip, the feedback loop was turned on between individual measurements. To avoid lateral drift, the tip was stabilized at the EC for 10 h prior to the series.

The grid measurements can be used to directly image the time evolution of light emission. At first, we compare the map of steady-state intensity (Fig. 4.16f) that is usually reached after 30-40 ns (see Fig. 4.14) with the previously obtained photon map (Fig. 4.16b). Indeed, the transient map reproduces the spatial extent of the EC. Next, we plot the transient maps as a function of time delay from the beginning of the pulse, which are shown in Fig. 4.16c-f. As indicated by the charging time lateral dependence, the light evolves from the brightest point of the EC to the periphery, where the steady-state is reached the latest. This effect is emphasized in the panels g-j of Fig. 4.16, where each point has been scaled to its intensity maximum reached under steady-state conditions. By measuring the nanosecond-resolved light emission we are able to probe and image the single electron charging in 4 dimensions at the molecular scale.

4.6 Conclusions

Emission centres arising due to the defects in C_{60} thin films are valuable model systems for studying the dynamics of single charges and excitons. STML provides access to these dynamics at the molecular scale in various ways. First, the exciton lifetime can be probed without using time-resolved detectors by leveraging the reciprocal relation between the tunnelling current and the average time between injected charges that may quench the excitons within their lifetime. Second, using voltage pulse excitation in the TR-STML scheme, we can follow the formation of a single exciton at the nanoscale, reaching the goal long sought in the organic electronics community [26]. We extended the tip-sample distance dependent studies to the lateral dimensions, which resulted in spatial probing of single electron charging, a process critical for light harvesting and chemical reactions. By extracting time-resolved light intensity from every pulse measurement, we imaged light emission with unprecedented simultaneous nanometre and nanosecond resolution converting an STM into an ultra-fast camera.

The charge and exciton dynamics can also be probed using STM in the Hanbury Brown-Twiss configuration with even better time resolution (down to 50 ps) and provide information on the photon statistics. However, the measurements using HBT-STM require exceptional electroluminescence intensities [19, 60] and are thus limited to systems with high efficiencies or high current measurements. Using methods presented in this chapter, in particular TR-STML, we were able to study C_{60} thin films at currents low enough (pA) to reach the individual charge injection regime, thus reducing any perturbations and allowing studies of low-efficiency systems. The combination of HBT-STM and TR-STML thus provides a versatile set of tools for studying the dynamics of luminescence at the nanoscale.

5 Dynamically controlled exciton-plasmon luminescence from C_{60} thin films[1]

As discussed in Chapter 2, localized collective oscillations of electrons at the metal-dielectric interface (plasmons) are an efficient way of reaching below the diffraction limit down to the sub-nm scale [70]. Such resolution can be achieved using not only absorption and scattering methods, but also plasmonic electroluminescence occurring on sub-picosecond timescales [22]. Because the nanosecond excitonic emission is also present at the nanoscale (see Chapter 4), it is highly desirable to study the coexistence and dynamical interaction of these two emission mechanisms to explore the possibilities this combination offers [225].

In the following, we will show that plasmonic emission present in C_{60} thin films can be properly identified and differentiated from the excitonic emission using local measurements. Later we will profit from these differences to achieve a nanoscale light source with bimodal characteristics. Its properties can be controlled by the lateral charge injection position, band alignment and sweeping the injection dynamics from nanoseconds to picoseconds by altering the tunnelling current. All mechanisms allow continuous tuning of the emission colour.

5.1 Origin of plasmonic luminescence from C_{60} thin films

Fig 5.1a,b show a topography and a photon map of a region where there is an EC located in the top right part of the image. Additionally, we observe a dimmer homogeneous luminescence at the upper terraces. An emission spectrum recorded in such a region is presented in Fig. 5.1d. It shows a broadband emission, which is a hallmark of plasmonic luminescence (see Section 2.2.1). Notably, this type of light emission is observed only on thicker C_{60} layers and the lowest terraces in Fig. 5.1c remain dark. The plasmonic luminescence yield is 2 orders of magnitude lower than the maximum quantum efficiency measured for excitonic emission (10^{-6} and 10^{-4} photons per electron, respectively).

The excitation mechanism of such broadband emission is related to inelastic tunnelling. In the case of the C_{60} multilayer system with an applied negative bias, this process can occur on

---

[1] This chapter is based on a publication #7 from the publication list

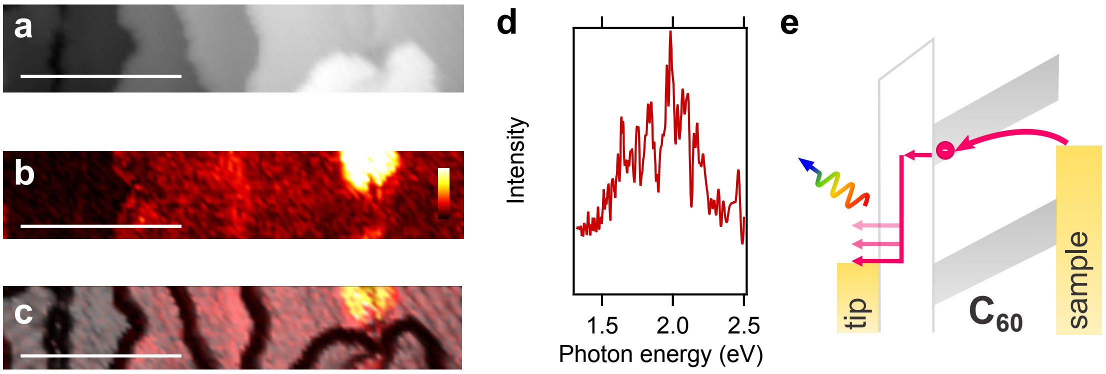

Figure 5.1 – Plasmonic luminescence from C_{60} thin films. a) Constant-current topography of a C_{60} thin film grown on Au(111). b) Photon map recorded simultaneously with a). The colour scale bar ranges from 0 to 1 kcts s^{-1}. c) Overlay of maps shown in a) and b). Horizontal scale bar 20 nm, U= -3 V, I = 30 pA. d) Optical spectrum recorded on the region with homogeneous luminescence, U = -3.3 V, I = 700 pA. e) Energy scheme for an inelastic process yielding plasmonic emission.

the tip-C_{60} interface. Since direct tunnelling of an electron from the substrate to the tip is not possible, the electron is injected first into the LUMO-derived band that is bent below the Fermi level of the substrate (see Fig. 5.1e) and then tunnel inelastically exciting plasmons. For this to occur, the electric field in the layer has to be particularly strong, which can be provided by a high applied bias, close distance (high current set-point) and a very sharp tip. For the Ag(111), where the LUMO-derived band has an onset closer to the Fermi level of the substrate (see section 4.2.3) the band alignment favours plasmonic generation as compared to the Au(111) substrate, an enhancement which indeed we observe in our experiments [76, 108].

5.2 Distinguishing between plasmonic and excitonic luminescence

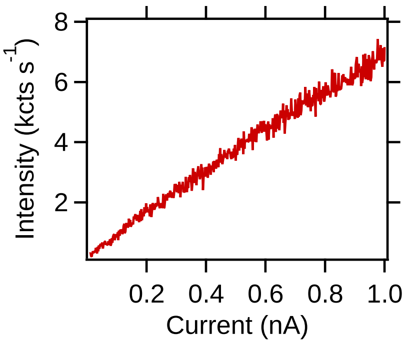

Figure 5.2 – Plasmonic light intensity as a function of current. U = -3.3 V.

Identifying the emission mechanism and the distinguishing between the plasmonic and excitonic luminescence occurring in C_{60} thin films probed by STML can be done in multiple ways. First of all, one can compare the emission spectra (Fig 5.1d and Fig. 4.5), which exhibit different characteristics. The excitonic emission has a sharp feature due to the defined energy of the transition, whereas the plasmonic luminescence is broadband. Next, the emission may be characterized by the P(I) function, which describes the dynamics of respective electroluminescence channels. As shown in the previous chapter (Fig. 4.8), P(I) for the excitonic emission rises in a sub-linear fashion, due to exciton annihilation. Plasmonic emission, on the other hand, has a linear relationship between in-

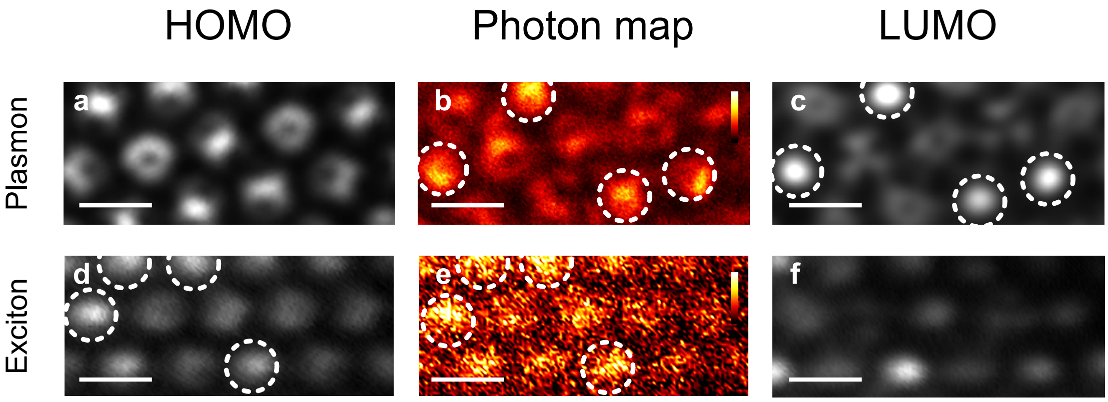

Figure 5.3 – Orbital and photon mapping of plasmonic (a)-c))and excitonic (d)-f)) luminescence. a) Constant height dI/dV map of the HOMO-derived band, U = -3.1 V. b) Photon map recorded simultaneously with a). c) Constant height dI/dV map of the LUMO-derived band, U = 1.6 V. d) Constant height dI/dV map of the HOMO-derived band, U = -2.8 V. e) Photon map recorded simultaneously with d). f) Constant height dI/dV map of the LUMO-derived band, U = 1.5 V. All scale bars 1 nm. Colour scale in b) ranges from 0 to 23 kcts s^{-1} and e) from 0 to 1 kcts s^{-1}. The molecules with the highest electroluminescence are marked in respective dI/dV and photon maps to enhance the similarity with the respective band.

tensity and current, both at low (few pA) and high (1 nA) currents, as shown in Fig. 5.2. For plasmons, there is no efficient charge-driven quenching channel, which could introduce deviations from linearity. Thus P_{pl}(I) can be written in a simple form of:

$$P_{pl}(I) = \frac{\gamma I}{e} \tag{5.1}$$

With γ being the experimentally observed plasmonic quantum efficiency.

The difference between the two emission mechanisms is evident also when comparing DOS (dI/dV) maps of the frontier bands with the respective light emission map as presented in Fig. 5.3. Such comparison permits determining the primary charge transport channel responsible for the light emission. The orbital through which such transport occurs is visible in the photon map [112]. On the ECs (Fig. 5.3d-f), the inhomogeneous photon map resembles the dI/dV map of HOMO-derived band (see circles in Fig. 5.3d,e), as expected for the hole-driven electroluminescence. On the other hand, the maps recorded at the region of plasmonic luminescence, reveal that the homogeneous photon map reproduces the shape of the LUMO-derived band, as marked by the circles in Fig. 5.3b,c. This correlation further indicates that the plasmonic luminescence occurs due to the electron injection into LUMO-derived states bent below the Fermi level of the substrate and further inelastic tunnelling to the tip when the plasmonic emission is excited.

5.3 Tuning between the excitonic and plasmonic emission

Having identified the two components of the electroluminescence from C_{60} thin films, we can now use this characterization toolbox to continuously tune the relative weight of the components of the plasmonic and excitonic emission. It can be done by the tip-position and the injection current, which controls the dynamics of charge injection into the system. To capture the respective dynamics of both components, we can use a combined P(I) function that describes both emission mechanisms:

$$P(I) = P_{ex}(I) + P_{pl}(I) = \eta \frac{\alpha I}{\alpha I \tau_{ex} + (e + \alpha I \tau_{el})\left(1 + \frac{\beta I \tau_{ex}}{e}\right)} + \frac{\gamma I}{e} \tag{5.2}$$

With $\alpha, \beta, \gamma, \eta, \tau_{ex}, \tau_{el}$ being the hole trapping efficiency, exciton-charge annihilation efficiency, the experimentally observed plasmon quantum efficiency, the detection efficiency, the exciton lifetime and electron injection time. This equation extends the previously described P(I) for the exciton (eq. 4.2) by the electron injection time component. A more detailed discussion on the approximations of the kinetic model can be found in Chapter 3.

Tuning by the injection position

Fig. 5.4 shows the smooth transition from plasmonic to excitonic luminescence upon approaching an EC (bottom to top), which is characterized by the topography (Fig. 5.4a) and the simultaneously recorded photon map (Fig. 5.4b). We measure the electroluminescence spectrum (Fig. 5.4c) and P(I) curves (Fig. 5.4d) on the positions marked in Fig. 5.4b. When the tip is approaching the EC we see the evolution from the broadband plasmonic (bottom trace) to sharp excitonic electroluminescence (top trace). Simultaneously, the P(I) curves evolve as well, from linear plasmonic to sub-linear excitonic dependence. These curves can be fit with eq. 5.2 and yield parameters listed in Fig. 5.4d. We find that the plasmonic yield is rather constant, hole trapping efficiency increases upon approaching the EC, in agreement with measurements shown in Chapter 4. The exciton-charge annihilation probability β takes values between 0.07 and 0.17.

Similar measurements performed recently on individual phthalocyanine molecules adsorbed on NaCl [63, 109–111] show that upon approaching the molecule, a Fano-like feature is observed, which is an evidence for the energy transfer from the plasmon to the molecule. In contrast, our measurements do not exhibit an apparent Fano-like feature, which suggests that the two emission channels are phase-decoupled, as the charge transport occurs through two different channels and the exciton is excited by the injected charges.

Tuning by the injection current

The relative ratio of the excitonic and plasmonic component in the emission can be also controlled by the charge injection dynamics (tunnelling current), which is apparent from eq.

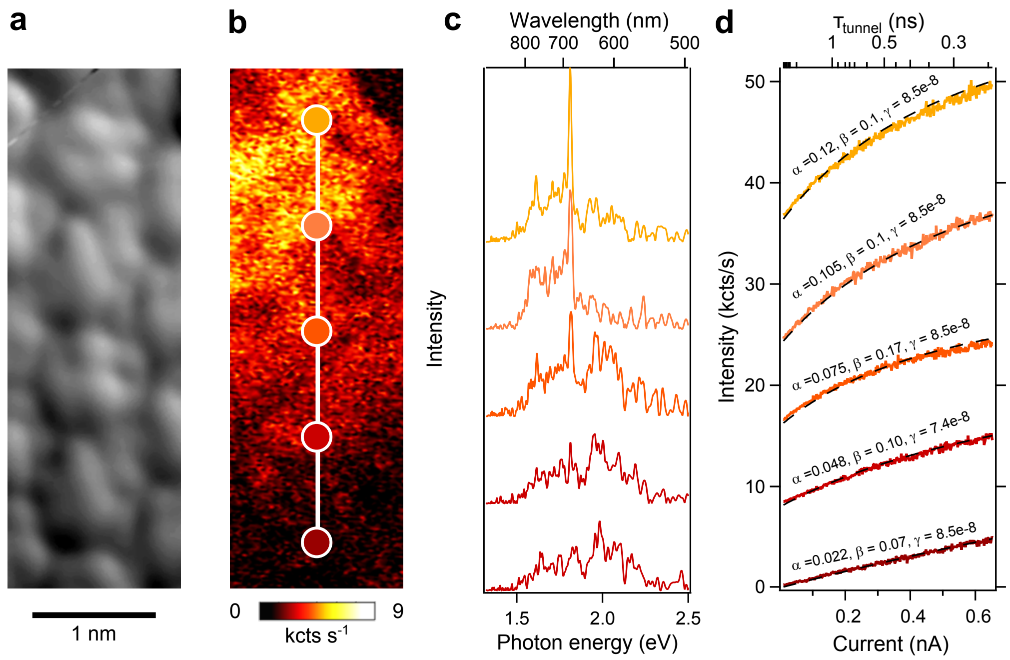

Figure 5.4 – Bimodal electroluminescence controlled by charge injection position. a) Constant-current topography of C_{60} thin film grown on Au(111), U = -3.3 V, I = 50 pA. b) Photon map obtained simultaneously with a). The marks indicate the positions of measurements in c) and d). c) Optical spectra measured at the positions marked in b), U = -3.3 V, I = 700 pA. d) P(I) curves measured at the positions marked in b), U = -3.3 V. Traces in c) and d) are vertically offset for clarity. Dashed lines are fits to eq. 5.2.

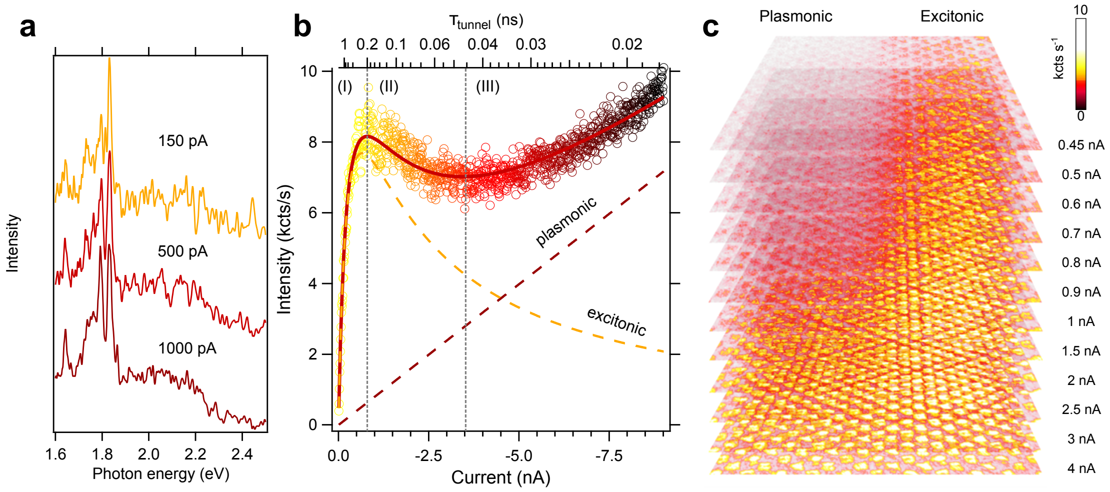

Figure 5.5 – Bimodal electroluminescence controlled by charge injection dynamics. a) A series of optical spectra recorded on an EC as a function of tunnelling current, U = -3.5 V. b) P(I) measurement at an EC, the three regimes (I) to (III) are discussed in the text. The line shows a fit to eq. 5.2. U = -3 V. c) A stack of photon maps (13.7 nm × 9.3 nm) recorded on a region with excitonic and plasmonic electroluminescence. The current is indicated next to each image. All maps have the same colour scale (top right). U = -3 V.

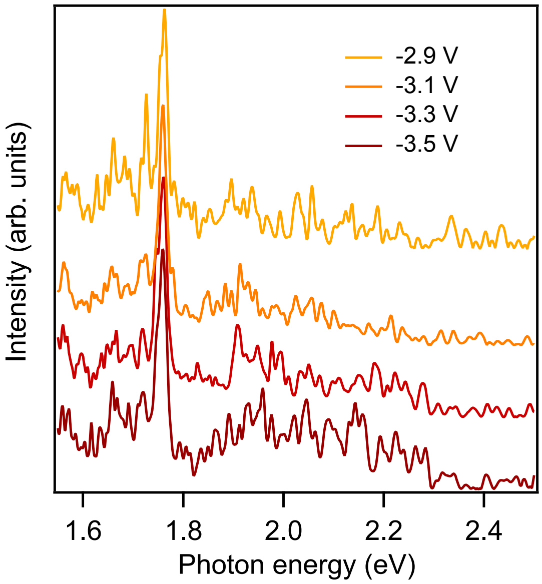

Figure 5.6 – Bimodal electroluminescence controlled by bias. I = 680 pA, integration time 120 s for each curve. The spectra are normalized to the maximum and shifted vertically for clarity.

5.2 and eq. 4.1. The optical spectra as a function of current are presented in Fig. 5.5a, in which the plasmonic component increases with the current I. Fig. 5.5b shows a P(I) measurements up to 9 nA performed on a bimodal source. The curve shows three regimes: (I) At low currents P(I) increases steeply, but with the sub-linear characteristics (as in Fig. 4.8); (II) at moderate currents, between 1 nA and 4 nA, the curve decreases from the local maximum (1 nA) to a local minimum (4 nA); (III) at high currents, above 4 nA the intensity increases again, however much slower than in (I). This data can be fitted with eq. 5.2 and yields α = 0.09, β = 0.5 and γ = 1.3 $\times 10^{-7}$. The separated excitonic and plasmonic components are plotted in yellow and red respectively. The excitonic electroluminescence dominates when the current is low and has its maximum when τ_{tunnel} is close to τ_{ex}. For higher injection rates it decreases due to exciton-charge annihilation that efficiently quenches the light emission. The regime (II) of the P(I) curve can thus be used to realize an optoelectronic NOT-gate, a critical component for the photonic circuitry. In the regime labelled as (III), the plasmonic electroluminescence increases linearly with the current and for I > 4.5 nA outshines the excitonic component.

Apart from measurement of the P(I) curve, this bimodal emission can be spatially resolved as a function of the tunnelling current, as presented in a stack of photon maps (Fig. 5.5c). At low injection currents, the electroluminescence channels are clearly distinguishable, the excitonic emission on the right is much more efficient than the plasmonic emission present on the left. When the current increases and τ_{tunnel} reaches the picosecond regime, the two intensities become comparable.

The P(I) (or equivalent quantum efficiency vs. current) dependencies were also probed for ZnPc molecules absorbed on a decoupling NaCl layer [60, 63]. For this system, the light inten-

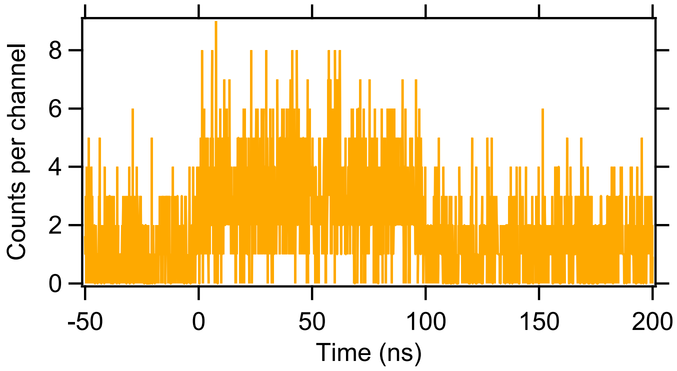

Figure 5.7 – TR-STML measurement performed on a region with plasmonic electroluminescence. U_{off} = -2.53 V (onset of the HOMO-derived band for this region), U_{on} = -2.83 V, I_{pulse} = 18 pA, acquisition time: 20 min.

sity increases with the tunnelling current in a super-linear manner. The authors suggested that this effect is related to an enhancement of a radiative decay rate when the tip is located closer to the molecule. This variation of mechanisms involved in light emission that is reflected in P(I) curves shows that these measurements provide an important insight into the physics of exciton-plasmon coupling at the nanoscale.

Tuning by the injection bias

Another parameter that can be used to control the components of the bimodal emission is the bias voltage. Applying higher negative bias enhances the band bending of the LUMO-derived states (see Fig. 5.1e), which results in a more efficient opening of the electron injection channel and an increased probability of plasmonic emission. Indeed, a series of spectra where the current set-point was constant (680 pA) and the bias voltage was increased (Fig. 5.6) confirms that and the plasmonic component increases with bias. Applying a positive bias to the junction leads to plasmonic emission, which occurs also via the LUMO-derived band [193].

5.4 Time-resolved plasmonic electroluminescence

We have studied the dynamics of plasmonic emission using TR-STML (see Section 2.4.3). Fig. 5.7 shows a transient obtained on a region with plasmonic electroluminescence. The edges of the luminescence transient are sharp and do not reveal notable dynamics on a timescale slower than 1 ns indicating that this light source operates in at least GHz regime, similar to previously reported plasmonic emission mediated by a presence of an adsorbed molecule [216]. If there was an observable dynamics it would be attributed either to electron injection time or to its residence time in the LUMO-derived band. This conclusion comes from regarding the emission as a three-state process: empty LUMO-derived band → populated LUMO-derived band → inelastic tunnelling (see Chapter 3 for a more detailed discussion). One has to note that these measurements on C_{60} multilayers are particularly challenging, because of the low plasmonic quantum efficiency. Because of that, the data have to be obtained at currents higher than used for the measurements of the exciton formation (see Section 4.4), which may be a regime of dynamics faster than the experimental resolution.

5.5 Conclusions

This chapter shows that C_{60} thin films are an efficient platform for studying the coexistence of excitonic and plasmonic electroluminescence at the molecular scale. In contrast to emission due to the exciton recombination that has a defined emission energy, the plasmonic luminescence occurs due to an inelastic tunnelling process leading to a broadband spectrum. The two components can be tuned by the charge injection position, bias and the tunnelling current that define the charge dynamics in the system. As a result, we obtain a quantum light source with a tunable emission spectrum. In addition, we show that the plasmonic electroluminescence operates in the GHz range.

6 Dynamics of H_2 molecules on the Au(111) surface[1]

The pursuit for alternatives to fossil fuels has lead to rapid development of vehicles powered by electricity, in particular, provided by lithium-ion batteries and hydrogen fuel cells. An issue of critical importance for the latter is thus hydrogen storage. Current methods include mechanical techniques (compressed or cooled gas), chemical hydrides and adsorption on the surface of porous materials [226]. Since H_2 is the smallest and the lightest molecule, it is particularly prone to diffusion and desorption making its storage challenging. Thus, studies on the kinetics and thermodynamics of its condensation, and the weak interaction with surfaces are critical for successful development of materials efficient for this task.

In the following chapter, we will present how this weak interaction leads to a motion of H_2 molecules adsorbed in a two-dimensional layer on Au(111) surface. A single molecule within the layer performs regular excursions below the apex of an STM tip. During the presence of H_2 in the tunnel junction the plasmonic emission from the metal substrate is changed, leading to alternating periods of luminescence and its absence. We study this process by measuring photon correlations and find that the excursions of the hydrogen molecule occur in the temporal range of few ms.

6.1 Molecular hydrogen on Au(111)

Molecular hydrogen adsorbates have been studied using STM both on various surfaces, such as graphene, hexagonal boron nitride [227, 228], Cu(111) [229, 230], Au(110) [231, 232] and next to structures deposited on Au(111) surface [233, 234]. Molecular hydrogen, due to its small atomic mass is inefficiently pumped by turbomolecular and ion pumps and is thus one of the major residual gas constituents in UHV. This presence of molecular hydrogen can result in a natural condensation of H_2 sub-monolayer on the surface of a cold (4 K) sample [80, 235]. A similar effect has been observed in the microscope used in this thesis, which operates at liquid helium temperature (4 K).

---

[1] This chapter is based on a publication #5 from the publication list

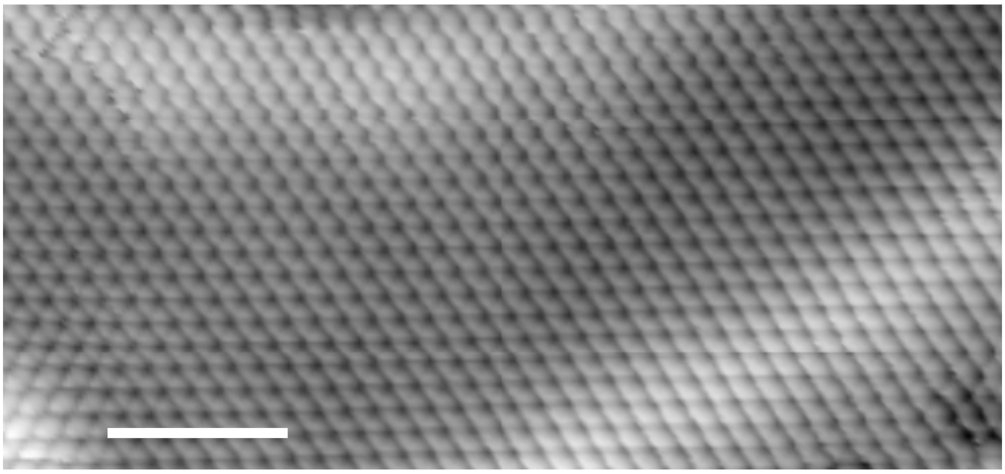

Figure 6.1 – Topography of an Au(111) surface with atomic resolution in the presence of hydrogen. U = 187 mV, I = 100 pA, scale bar 1.5 nm.

One of the effects that is typically associated with the presence of molecular hydrogen in the tunnel junction is an extraordinary enhancement of the topographic resolution in the STM images. The presence of H_2 enables imaging metallic surfaces with atomic resolution and molecules with bond resolution [236, 237], similar to what is obtained with a CO functionalized tip using non-contact AFM [31, 40]. This effect has been observed regularly in our experimental sessions and one example of such topography is presented in Fig. 6.1. The STM image shows atomic resolution topography obtained on Au(111) surface at relatively mild tunnelling conditions (*i. e.* out of contact).

Apart from its indirect detection, hydrogen can be also imaged directly by STM. Fig. 6.2 shows a series of constant current STM images of a H_2 covered Au(111) surface. Fig. 6.2a and Fig. 6.2b present a large scale image of H_2/Au(111) terraces and a high-resolution image of the adsorbates, respectively. It is important to note that the adsorbates are visible only at high bias, here +3.1 V. As seen in the STM images, the H_2 molecules arrange into a hexagonal network, which is patterned by the herringbone reconstruction of the Au(111) substrate. The average periodicity of the superstructure is 2 nm, which is close to a half of the surface state Fermi wavelength λ_F defined as:

$$\lambda_F = \frac{2\pi}{k_F} \tag{6.1}$$

where k_F is the magnitude of the wave vector of the surface state electrons at the Fermi level. For Au(111) this value is 0.16 Å^{-1} and thus $\lambda_F/2$ = 1.95 nm [238–240]. This relation suggests that the interaction between the molecules is of surface-state-mediated nature [241, 242] and constitutes a so-called Fermi superlattice. When the electrons of the surface state of the substrate are scattered at the adsorbed molecules or atoms, oscillations of electronic density occur and induce an effective potential between adsorbates that traps them in certain positions of the surface [241]. The images of the superlattice (Fig. 6.2a,b) reveal streaky features. Such features are usually an indication of motion of the adsorbate on the surface that

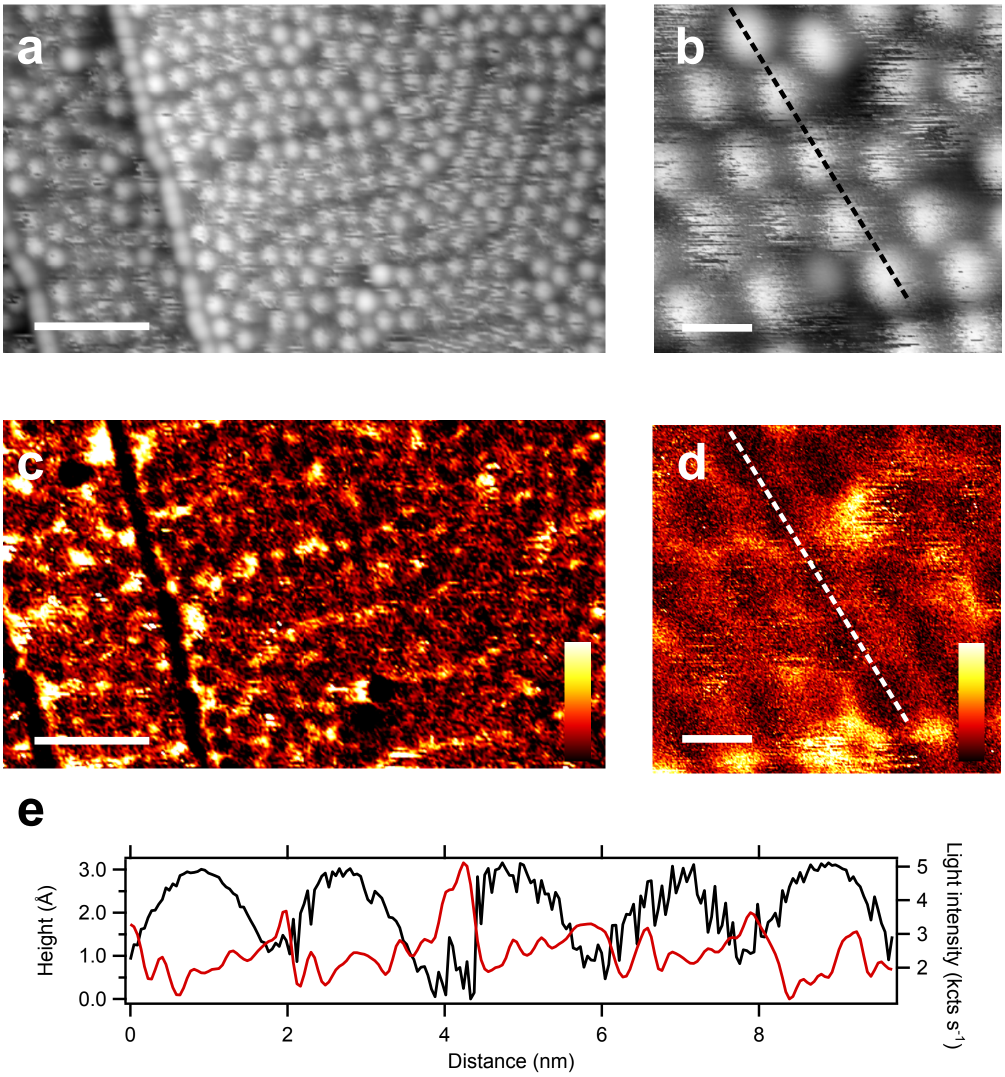

Figure 6.2 – H_2 on Au(111) - topography and luminescence. a) Large scale constant current image, U = 3.1 V, I = 30 pA, scale bar 10 nm. b) Small scale image, U = 3.1 V, I = 50 pA, scale bar 2 nm. Every white protrusion in a) and b) can be ascribed to a single H_2 molecule. c), d) Photon maps recorded simultaneously with the images in panels a) and b), respectively. The colour scale bar in the insets represent the spectrally integrated total photon intensity ranging from 1 kcts s^{-1} to 6 kcts s^{-1} and from 1 kcts s^{-1} to 12 kcts s^{-1} for c) and d) respectively. Scale bars 10 and 2 nm. e) Topography (black curve) and light intensity (red curve) profiles measured along lines indicated in b) and d). The highest light intensity positions are correlated with positions of lowest H_2 presence probability.

is slow enough to be registered by the feedback loop. This motion has important implications and will be discussed in detail in the following. The surface coverage of H_2 is estimated to be 2 % with respect to the reconstructed Au(111) surface atom density. However, this value will vary depending on the concentration of the hydrogen in the residual gas.

Hydrogen can be identified by measuring its characteristic vibronic features using either scanning tunnelling spectroscopy (STS) or inelastic scanning tunnelling spectroscopy (IETS) [227–233, 243]. The inset in Fig. 6.3 shows a spectrum with two characteristic peaks located symmetrically with respect to the Fermi level at the energy ± 48 meV [231, 233].

In order to further understand the experimental findings, the system was studied theoretically [2]. The relaxed geometry of the Au tip - H_2 - Au(111) system for tip-surface distances of 5 Å and 7 Å was calculated using density functional theory (DFT) is presented in Fig. 6.4a. The H_2 molecule is vertically aligned in the junction. One hydrogen atom is located directly below the last atom of the STM tip due to the higher reactivity of the low coordinated atom and the second hydrogen atom is located on top of a gold substrate atom.

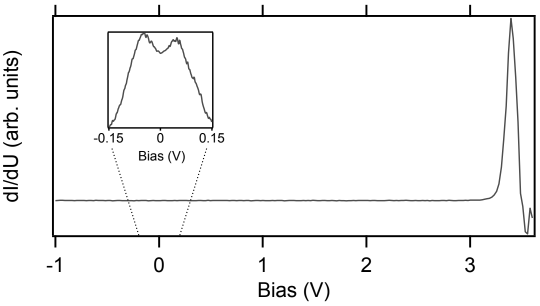

Figure 6.3 – Scanning tunnelling spectroscopy of H_2 on Au(111). Setpoint: U = +3.6 V, I = 118 pA; inset: U = -150 mV, I = 9.5 nA. The spectra were measured on top of the adsorbate.

This geometry was used to calculate the projected density of states (DOS), which reveals a peak at 2.58 eV above the E_F (Fig. 6.4b). As a comparison, Fig. 6.3 shows an STS measurement over a wide range of bias voltages measured on top of H_2. The spectrum shows a pronounced feature at +3.2 V which may be related to the antibonding $1\sigma^*$ state of a hydrogen molecule, as obtained from the calculations.

Since the $1\sigma^*$ state of the molecule is populated only at high positive voltages, the adsorbate is expected to be invisible at negative voltages. This effect is presented in Fig. 6.5, which shows that the surface is covered with the H_2 layer at +3.02 V, but at the negative voltage of -2.97 V it appears clean, even though it was verified that the layer is still present. This bias dependent invisibility may be a reason why such layers were previously unobserved in STM since the usual operational bias voltages range from -1 V to +1 V for most experiments. Another possible reason why the superlattice was not observed in other STM set-ups is that its formation may be strongly dependent on the precise hydrogen dose.

Moreover, the isosurface of the calculated DOS presented in Fig. 6.4a shows that the charge is unequally distributed between the two hydrogen atoms and is shifted towards the atom located closer to the substrate. This asymmetry can lead to the molecule being prone to the

---

[2] Calculations performed by Dr. C. González

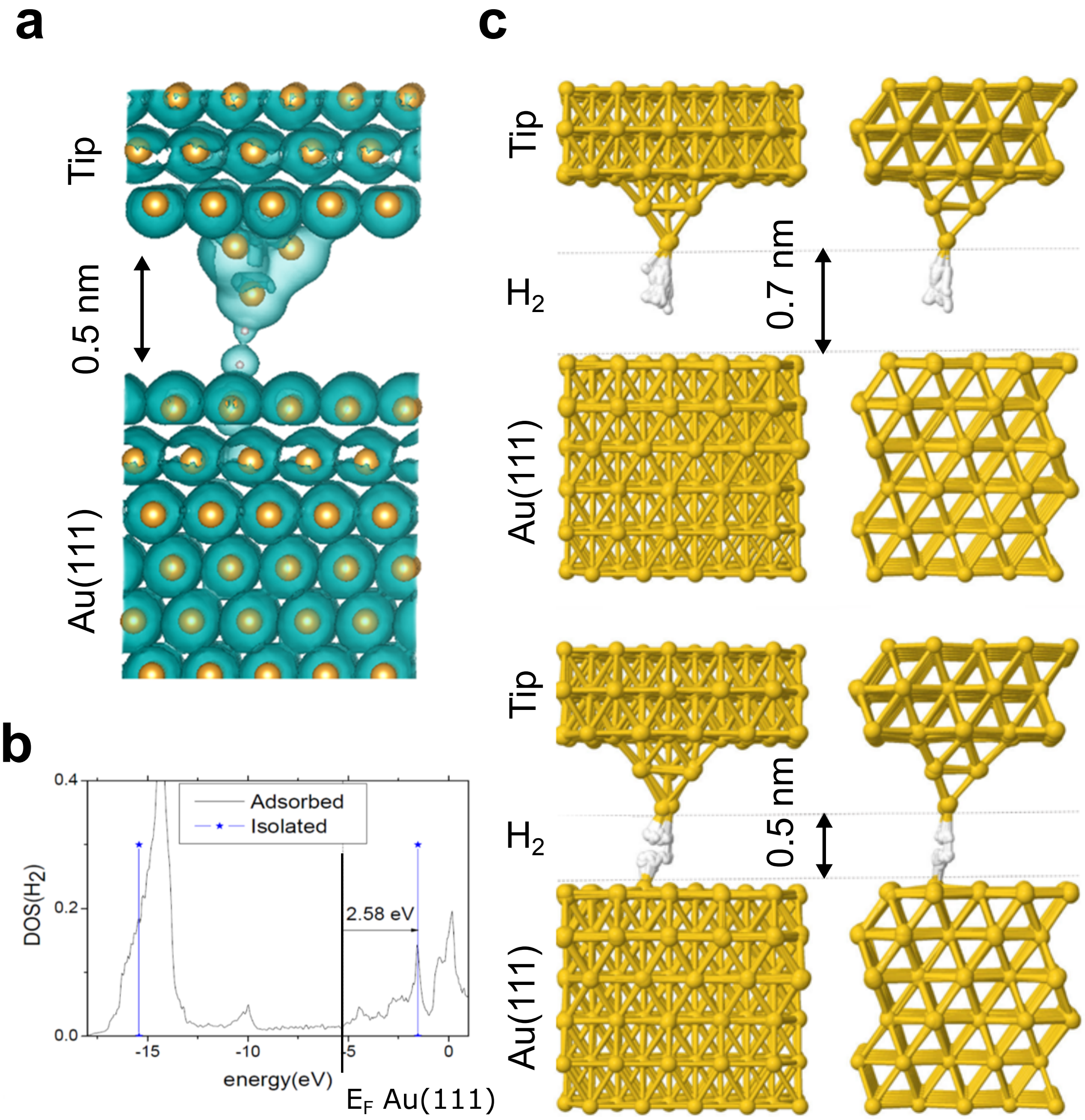

Figure 6.4 – DFT calculations of H_2 on Au(111) system. a) Isosurface of the density of states of the Au tip-H_2-Au(111) calculated at 2 eV. b) Projected electronic density of states as a function of energy. The line indicates the position of E_F c) Schematics of the molecular dynamics simulations. Left column front view, right column side view. The first 700 steps of the ab-initio molecular dynamics are overlaid in each of the schematics to represent the motion of the H_2 molecule in the tunnel junction. Calculations performed by Dr. C. González.

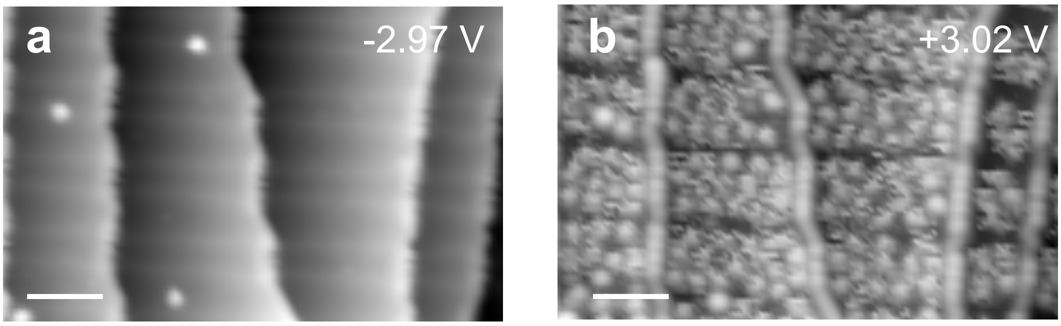

Figure 6.5 – Invisibility of H_2 superlattice at negative bias voltages. Two consecutive images of the same region are shown. a) U = -2.97 V, I = 107 pA. b) U = +3.02 V, I = 107 pA. Scale bars 7 nm.

excitation of vibrational and translational modes. Electron tunnelling results in transient charging of the molecules and the subsequent energy dissipation further excites the molecule leading to the excursion out of the junction. However, the potential associated with the Fermi superlattice will drive the H_2 back into the junction. As a result, the molecules may oscillate between two positions: inside and outside the junction.

The optimized geometry was used as a basis for *ab initio* molecular dynamics (AIMD) calculations to simulate the dynamics of the system upon excitation by the tunnelling current. Once an electron tunnels elastically to the molecule, the energy is transferred and dissipated to the system. This energy dissipation is modelled by equidistribution of 2.8 eV (energy of electrons during imaging of the superlattice) between all atoms of the unit cell. The system prepared in such a way is then allowed to evolve. Results of this evolution are presented in Fig. 6.4c, where the first 700 steps of the AIMD calculations are overlaid and show that the molecule oscillates in the tunnel junction. During these oscillations, the molecule may leave the junction and later return to its preferred position between the last atom of the tip and sample.

6.2 The H_2 molecule as a plasmonic chopper

As presented in the previous section, the H_2 molecule diffuses below the STM tip located above the Au(111) surface. To probe its dynamics, we record the time-resolved electroluminescence and calculate photon correlations.

First, we characterize the steady-state electroluminescence. Fig. 6.2c,d show large and small scale photon maps recorded in constant current mode. The luminescence arises due to the radiative decay of surface plasmon polaritons excited in the tip-sample junction by inelastic tunnelling (see Section 2.2.1 and Fig. 6.6a). One key observation here is that the luminescence efficiency, recorded in the constant current mode, is reduced at the positions where the molecules are located with the highest probability, which is reflected in the anticorrelation of height and light maxima in the profiles shown in (Fig. 6.2e).

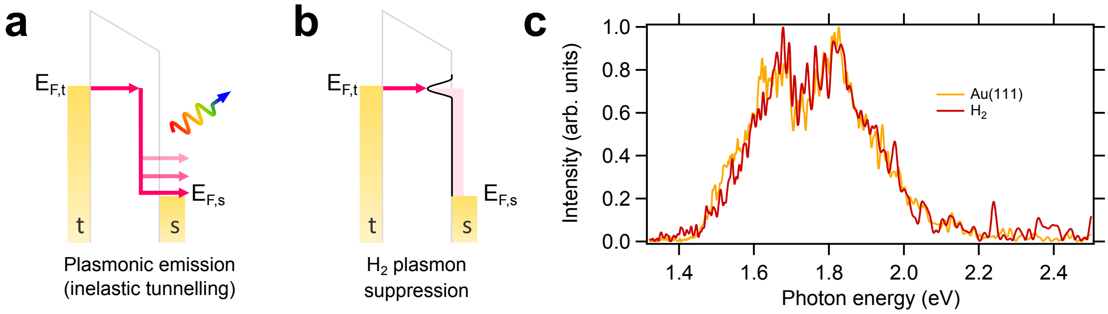

Figure 6.6 – Energy diagrams and optical spectroscopy of H_2 on Au(111). a), b) Energy diagrams for plasmonic emission and plasmonic suppression respectively. c) Optical spectroscopy on a clean Au(111) terrace (orange curve) and on H_2 molecule (red curve). The curves were normalized to the maximum. U = +3 V, I = 150 pA.

This luminescence efficiency alteration is not only related to the tip height variation (as in Fig. 6.2) but mostly occurs due to the presence of the state visible in Fig. 6.3, as it will be proven later by constant height correlation measurement. When the H_2 is present in the junction, the probability of inelastic tunnelling of electrons from the tip to the sample decreases and the charge transport, as well as the energy dissipation, occur via the electronic levels of the molecule (Fig. 6.6ab). Since this process modifies only the probability for photon emission, the spectrum when the molecule is present remains unchanged and shows the same broad plasmonic mode as when the surface is clean off the adsorbate (Fig. 6.6c).

When the H_2 molecule is excited and leaves the junction the inelastic tunnelling channel becomes the main channel and the probability for photon emission increases. Once the molecule returns to the junction, the plasmon creation is suppressed. However, when these processes are probed in a constant height mode (open feedback), the tunnelling current is higher when the molecule is present in the junction. This increase in the current overcompensates the reduced branching ratio in the tunnelling process, which results in an increase in the observed luminescence. Because the molecule is mobile, the luminescence alternates and results in a creation of photon bunches that are separated by the time the hydrogen is out of the junction - the molecule acts as a plasmonic chopper. This can be visualized in the time-resolved intensity traces, as in Fig. 6.7a, where the first 18 ms of measurement are shown. The experimental details were discussed in Section 2.4.3. In contrast, the emission on a clean Au(111) surface does not show such a behaviour (Fig. 6.7b) - the photons are emitted in a random process with a Poissonian distribution. One has to note, that these measurements are fast (only a few seconds) therefore providing easy access to the dynamics of adsorbate systems that modify plasmonic emission.

The photon intensity traces can be used to calculate the photon correlation function (see eq. 3.11). We find that for a clean Au(111) surface $g^{(2)}(\Delta t)$ is unity over 6 orders of magnitude in the time domain proving pure Poissonian photon statistics (Fig. 6.7c). It constitutes a critical reference measurement because photon bunching can be observed also due to

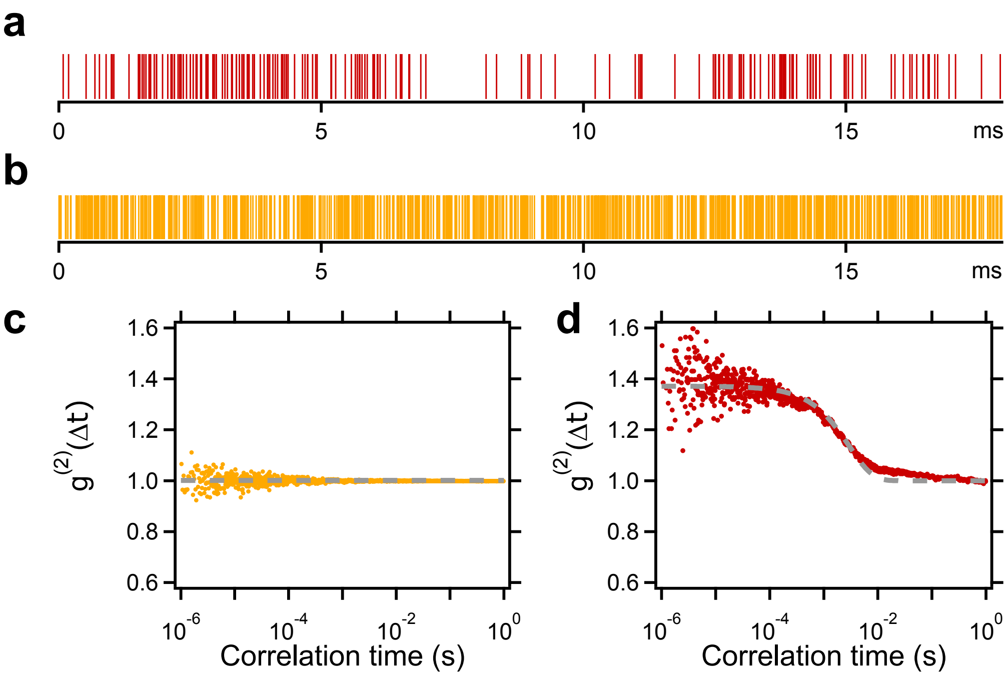

Figure 6.7 – Photon correlations at H_2/Au(111). a) and b) 18 ms sample of a photon train measured on a clean Au(111) and H_2/Au(111) surface respectively. The photon arrival times are indicated by vertical lines. The measurements were performed with an open feedback loop at the following set-point: U = 3 V, I = 250 pA. c) and d) calculated intensity correlation functions recorded on clean Au(111) and on H_2 respectively.

mechanical noise or other fluctuations of or in the junction [134–136]. On the other hand, the $g^{(2)}(\Delta t)$ function calculated for a measurement on the hydrogen molecules shows a significant bunching $g^{(2)}(0) = 1.4$. In order to derive the major transition time constant, we fit the data with an exponential function finding $T_1 = 2.37$ ms. This result indicates that the photons detected within times shorter that T_1 are not emitted independently of each other. Both measurements referred here were performed in the same conditions: +3 V, 250 pA set-point, with an open feedback loop (constant height). One has to remark here that the tip-sample distance at this set-point will be smaller for a clean surface than a surface with an adsorbate layer, due to the presence of the state visible in Fig. 6.3. This height difference results in lower intensity in between molecular excursions.

To further analyse our data we use a two-state rate model (see Chapter 3) with a dark and bright state referring to the absence and presence of the molecule in the junction with respective time constants T_{dark} and T_{bright}. The rates are related to switching between these two states and are defined in the following way: $k_{out} = \frac{1}{T_{bright}}$ and $k_{in} = \frac{1}{T_{dark}}$. To simplify the calculation we assume that there is no photon emission in the dark state. A solution for such system has

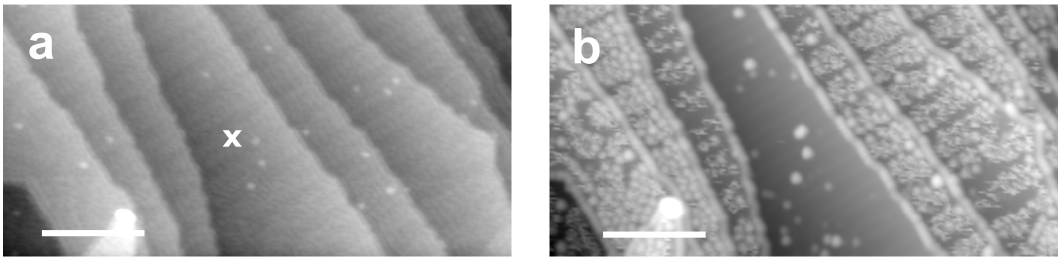

Figure 6.8 – Pulse-induced desorption of H_2. a) Constant current image before and b) after applying a voltage pulse of U = +6 V, t = 10 ms at the position marked by X. Scanning parameters for both images: U = 3.015 V, I = 107 pA, scale bar 20 nm.

the following form (eq. 3.19):

$$g^{(2)}(\tau) = 1 + \frac{k_{out}}{k_{in}} e^{-(k_{in}+k_{out})\tau} \tag{6.2}$$

and:

$$T_1 = \frac{1}{k_{in} + k_{out}} = \frac{T_{dark} T_{bright}}{T_{dark} + T_{bright}} \tag{6.3}$$

Using eq. 6.2 to fit data in Fig. 6.7d yields T_{bright} = 10.1 ms and T_{dark} = 3.1 ms. Therefore, the molecule tends to stay in the tunnelling junction, but performs excursions when excited and later returns to the gap. This motion proves the weak interaction between hydrogen and the gold surface.

In order to improve the fit shown in Fig. 6.7d we can expand eq. 6.2 by two additional exponential functions characterized by additional time constants T_2 and T_3. The modified fit yields $T_2 = 31\mu$s and T_3 = 87 ms. At the present stage, the origin of these two second-order time constants is not clear. The light-affecting processes that can be responsible for such time constants include dissociation of H_2 and molecular vibrations or rotations [231, 244, 245].

6.3 Controlled desorption of H_2

The weakly physisorbed molecules can be desorbed on demand by applying voltage pulses. Short (10 ms) pulses of an amplitude of +6 V that are locally applied to a terrace covered with molecules (Fig. 6.8a) efficiently remove adsorbates from the whole terrace (Fig. 6.8b). The neighbouring terraces remain covered with H_2 molecules. The fact that only the terrace where the pulse was applied is affected by the pulse strongly suggests that the desorption mechanism is related to the excitation of electrons in the surface state of Au(111). Similar surface-state mediated long-range effects have been observed for organic molecules adsorbed on the Cu(111) surface [246].

The molecules can be also desorbed by heating the sample. Our set-up can be slowly heated

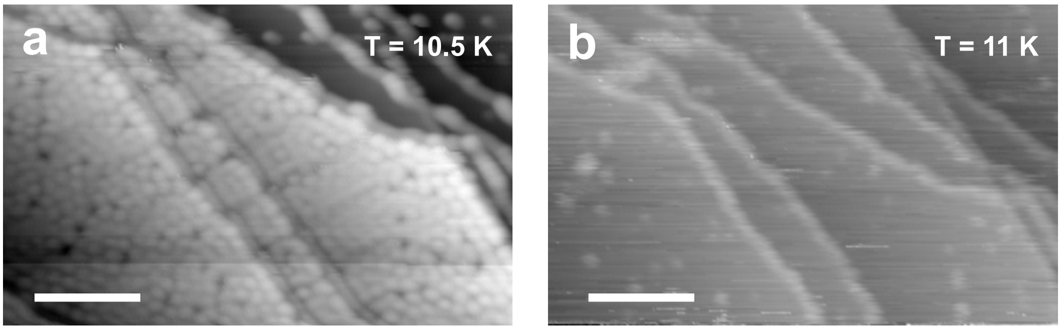

Figure 6.9 – Temperature-induced desorption of H_2. a) Constant current image at T = 10.5 K and b) T = 11 K. Scanning parameters for both images: U = 3.4 V, I = 100 pA, scale bar 12 nm.

once the helium cryostat has been emptied, which permits STM operation. The scans were recorded in approx. 0.5 K intervals as monitored by a Cernox thin film resistance cryogenic temperature sensor located on the STM head. The layer is still present on the surface at 10.5 K (Fig. 6.9a). However, when the temperature reaches 11 K, the layer is absent (Fig. 6.9b) and does not recover, also at higher temperatures. Desorption of hydrogen at these temperatures is typical for STM systems with liquid helium cryostats [235].

6.4 Conclusions

Studies presented in this chapter demonstrated the adsorption of H_2 on Au(111) at cryogenic temperatures. The molecules form a layer that can be described as a Fermi superlattice where the interaction of adsorbates with the surface electrons creates local potential minima that capture individual H_2 molecules. As supported by theoretical calculations, hydrogen in such potential is only weakly physisorbed, which leads to a translational motion below the STM tip. The presence of the molecule in the tunnelling junction modifies the plasmonic luminescence due to efficient elastic tunnelling to the $1\sigma^*$ antibonding orbital and therefore allows probing the motion inside and outside of the junction by photon correlations. The photons are emitted in bunches separated by the time in which the molecule is out of the junction. The correlation function of the measured intensity indeed yields bunching of $g^{(2)}(0) = 1.4$. Analysis of the data with the two-state rate model reveals the average residence times of H_2 molecule outside and inside the tunnel junction, as 3.1 ms and 10.1 ms respectively.

Such measurements provide valuable information about weak physisorption of H_2 on solid surfaces, which may be used to improve porous materials with high surface area employed for hydrogen storage. Moreover, experiments showed in this chapter extend the range of conventional STM beyond the kHz limit of the current amplifier, reaching the MHz regime by using a fast measurement method - one-detector correlation spectroscopy.

7 Emission of photon pairs from pristine metal surfaces[1]

The previous chapter presented how photon bunching arises due to the light-modulating motion of an adsorbate on a surface. Another physical process that naturally results in photon bunching is an emission of photon pairs [247], an effect critical for the implementation of quantum information processing. Such photons emitted simultaneously can be used to perform tasks based on heralded single-photons or, if entangled, superdense coding and quantum teleportation [248]. Currently, generation of such pairs is mostly done optically and based on the implementation of the following effects: four-wave mixing [249], pulsed lasers [250], and down-conversion [251].

In the following chapter, we will present how such photon pairs can be easily created using a generic metal-metal tunnel junction of an STM using a combination of Au tip and Ag(111), Au(111), and Cu(111) surfaces. This effect is reminiscent of recently reported photon pair emission from bulk tunnel junctions in the microwave regime at mK temperatures upon AC driving [252], but observed at more applicable conditions: higher temperatures, DC excitation and in the optical regime.

7.1 STML at high bias

When the bias applied to the tunnel junction is high enough to exceed the work function of the sample ($U > \phi_S$), the electron can be emitted into the vacuum. Noble metals, such as Au, Ag, and Cu have a band gap below the vacuum level (few eV above E_F). As a result of that, the electron will experience a potential barrier at the vacuum-metal interface. On the other hand, a single charge in front of a metal induces an image charge that creates an attractive potential towards the surface. These two effects combined lead to a formation of a potential well in front of the surface (Fig. 7.1), which is filled with an infinite series of Rydberg-like states [253–255], in STM studies often referred to as field emission resonances (FERs).

These states can be probed using dz/dV spectroscopy - a measurement in which the current

---

[1] This chapter is based on a publication #4 from the publication list

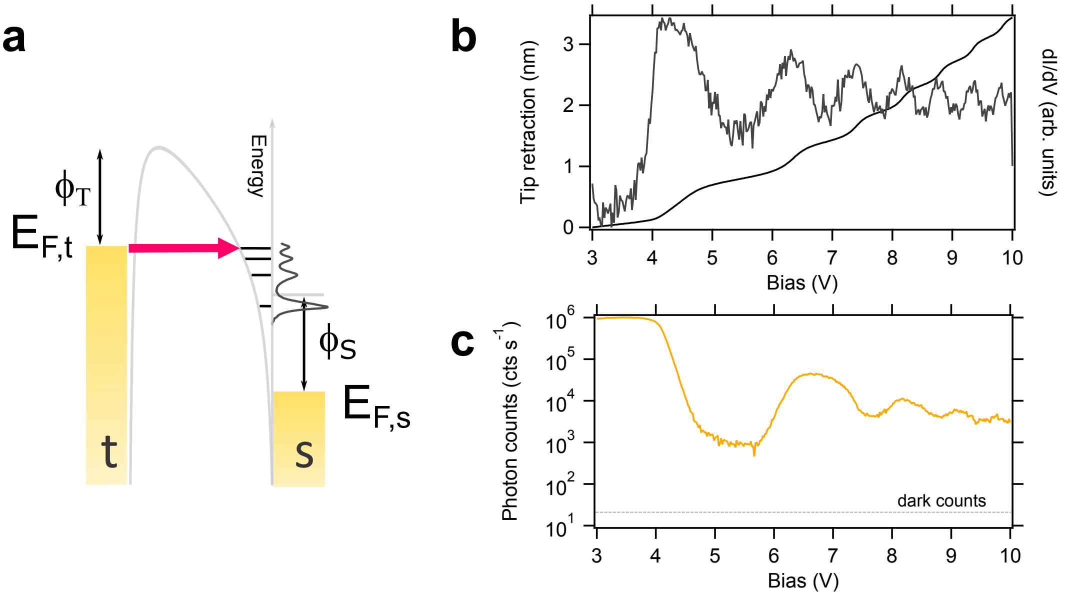

Figure 7.1 – The principle of probing image potential states. a) Energy scheme with Rydberg-like states in front of a surface, $U > \phi_S$ b) Tip retraction (black curve) and dI/dV (gray curve) measured on Cu(111) surface as a function of bias in the constant current mode, I = 5 nA, c) Light intensity recorded simultaneously with b). The horizontal line indicates the value of the dark counts of the detector (20 cts s^{-1}).

feedback is on, the bias is swept up usually to the limit of the used electronics (10 V in this case) and the tip z piezo position is recorded. When the applied bias is in resonance with one of the image potential states, the transmission of the junction is very high resulting in a rapid tip retraction, a condition necessary to maintain the current set-point. The dz/dV signal can be obtained either by calculating the numerical derivative of the recorded tip retraction or by running the lock-in amplifier at modulation frequencies above the current feedback response and reading the dI/dV signal [52].

An example of such measurement is shown in Fig. 7.1b. There are 7 image potential states visible in the range 3-10 V. The number of FERs observed in the given bias window depends on the tip sharpness [145] and can be used to estimate its curvature. Simultaneously we record light intensity (Fig. 7.1c) which between 3 and 4 V is so high that the SPAD reaches its saturation (millions of counts per second), above 4 V rapidly drops to approx. 1 kcts s^{-1} and recovers around 6 V showing oscillations. The electroluminescence has a broad spectrum (Fig. 7.7a), characteristic for the radiative decay of surface plasmon polaritons, a process that is extremely efficient in the optical regime when excited by bias voltages between 3 and 4 V. The subsequent oscillations occur due to inelastic tunnelling to respective FERs located at energies E_n and light is observed when the photon energy $h\nu = eU - E_n$ falls into the detection range of the SPAD/spectrometer [57, 145], in this case ~ 1.2 V - 3 eV.

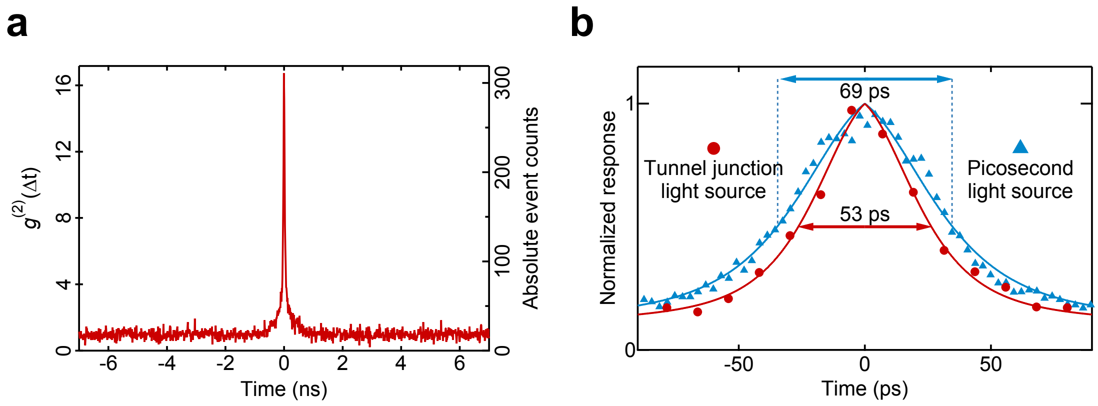

Figure 7.2 – Photon super-bunching from a tunnel junction. a) $g^{(2)}(\Delta t)$ measured at U = 4.63 V, I = 20 nA for Au-Ag(111) junction b) A comparison of the measurement showed in a) with a reference obtained with a picosecond light source. Both traces are normalized to unity.

7.2 Super-bunching of photons emitted from a tunnel junction

In the following part, we will inspect closely the light emitted at the regime between the 1st and 2nd FER (Fig. 7.1b). Although the intensity is low, it is sufficient to run a correlation measurement in the Hanbury Brown - Twiss configuration (for details see Section 2.4.3). The plot presented in Fig. 7.2a shows the $g^{(2)}(\Delta t)$ for Au-Ag(111) junction biased at 4.63 V at 20 nA, with $g^{(2)}(0)$ significantly greater than the limit for classical chaotic light ($g^{(2)}(0) \leq 2$), evidencing photon super-bunching effect (see Chapter 3). The registered events can be divided into two types, namely accidental coincidences when two uncorrelated photons are detected at any time delay (contributing to the correlation baseline, by definition $g^{(2)}(\Delta t)=1$), and true coincidences when (at least) two photons arrive simultaneously to both detectors resulting in $g^{(2)}(0) > 2$. The super-bunching peak is a very sharp feature, which decays within ± 1 ns. In that case, it is necessary to compare it with the detector's time resolution, as shown in Fig. 7.2b, which was measured with a picosecond light source (see Section 2.4.3) yielding FWHM of 69 ps. On the contrary, the FWHM of the trace obtained with a tunnel junction light source is 53 ps, which is closer to the true response time of the SPADs (30 ps as provided by the manufacturer) than the reference measurement with the laser. This leads to the conclusion that the observed process most likely occurs at the sub-ps timescale.

7.3 Dependence of super-bunching on the junction parameters

Current dependence

The observed effect can be probed as a function of the junction parameters, such as tunnelling current, bias voltage and junction geometry. Fig. 7.3a shows how super-bunching depends on the tunnelling current. The junction conditions were chosen so that the applied voltage coincides with the peak of the 1st FER. Since these states are subject to a significant Stark shift,

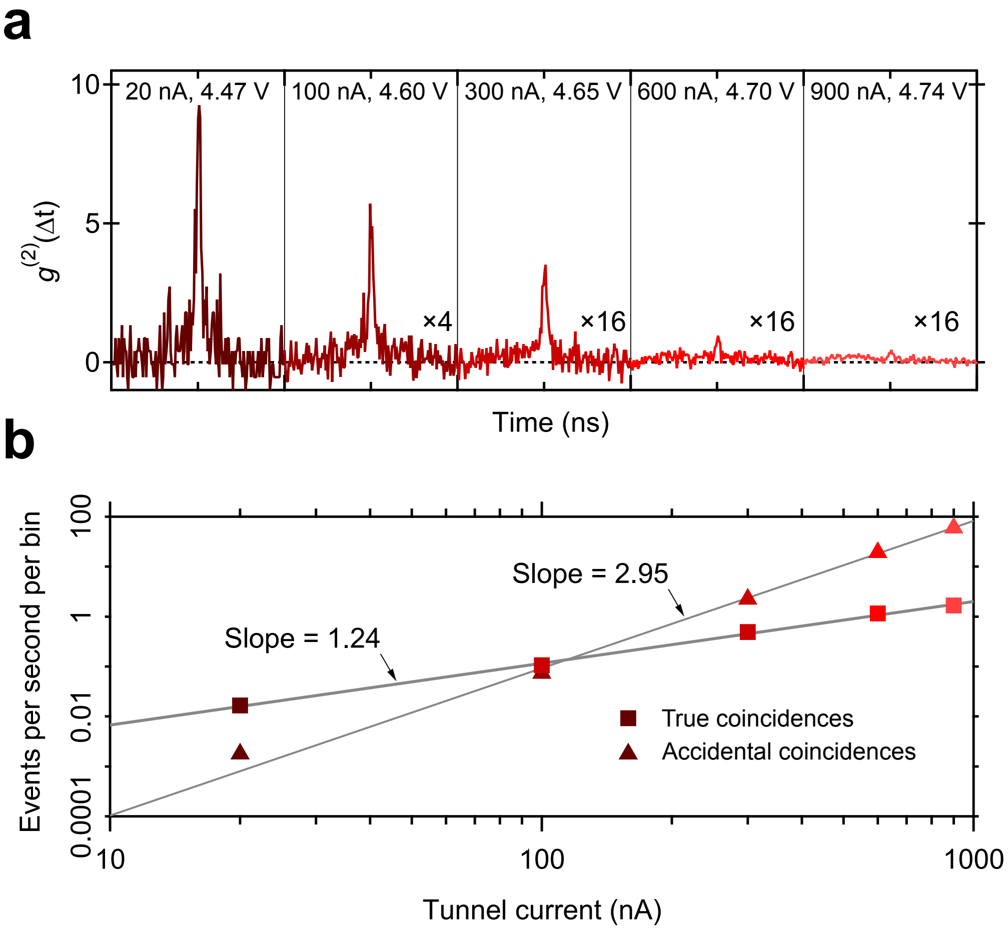

Figure 7.3 – Bunching as a function of current. a) $g^{(2)}(\Delta t)$-1 as a function of current. The bias is slightly adjusted to follow the position of the 1st FER. Accumulation times: 1200 s for 20, 100, 300 nA; 600 s for 600 and 900 nA. b) log-log plot of the absolute number of true and accidental coincidence events per integration bin as a function of current. The slopes of the power-law dependences are shown.

the bias has to be readjusted accordingly (see labels in Fig. 7.3a) in order to maintain the same tunnelling current at the peak of FER. The bunching factor is highest when the current is low and gradually disappears within the increasing correlation baseline of accidental coincidences as the current rises.

These results can be analysed in a quantitative way by plotting the number of true (the value of $g^{(2)}(0)$) and accidental coincidences (extracted from the correlation baseline) per measured bin as a function of current in a log-log plot. The respective points fall on lines, with exponents of the power law of 1.24 ($\sim I^{1.24}$) for true coincidences and 2.95 ($\sim I^{2.95}$) for accidental coincidences. As the uncorrelated photons arise due to independent tunnelling of two electrons that create a plasmonic excitation each, the fact that true coincidences scale with a factor less than a half of uncorrelated events is a strong indication that the observed photon pairs are created by only one electron.

Voltage dependence

Super-bunching depends also on the bias voltage. As evidenced from the scaling (Fig. 7.3b), it is best observed when the total light intensity is made low, which occurs between the 1st and the 2nd FER (Fig. 7.4a). The super-bunching index measured for these voltages is plotted in Fig. 7.4b and indeed shows maximum around 5 V. We have observed bunching for voltages as low as 3.2 V (with a tunnelling current of 20 pA), confirming that the super-bunching effect is not related to the population of the 1st FER. Moreover, we anticipate that the value of 3.2 V is not yet reaching the experimental limit, as measurements at even lower bias and current are possible for tips with a particularly strong plasmonic enhancement to ensure reasonable integration times (limited by the cryostat standing time). We have observed photon bunching up to voltages of 6 V. In general, the range between 3.2 V and 6 V in which bunching is observed, coincides with twice the detection limit of our set-up (~ 1.2 V - 3 V), indicating a presence of a down-conversion-like effect, which will be discussed later.

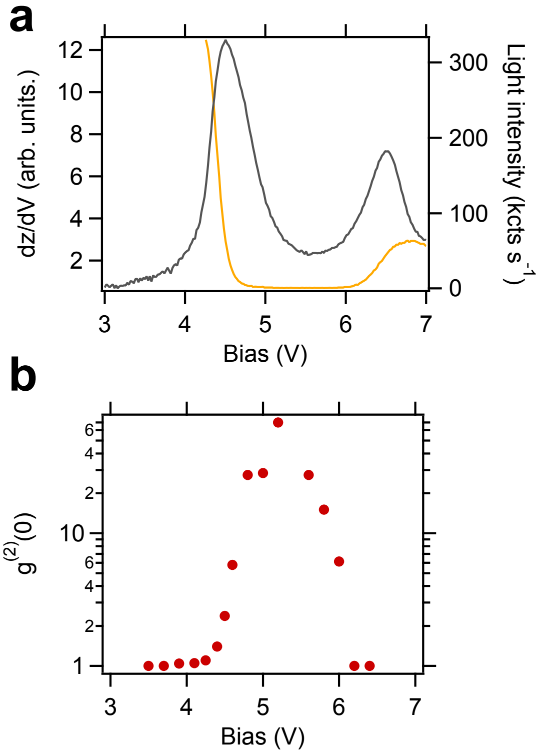

Figure 7.4 – Bunching as a function of bias. a) dz/dV spectrum (gray) and light intensity (yellow). b) Values of $g^{(2)}(0)$ vs. bias. I = 10 nA, measurement performed on Cu(111) surface.

Surface topography dependence

To ensure a proper evaluation of the data we monitor the stability of the tunnel junction by recording the z position of the scanner. Any substantial step in this trace indicates a change in the tip or on the surface, which may change the plasmonic enhancement preventing comparison between experiments. We also check the surface after the measurement, as shown in Fig. 7.5, which contains images before and after measurements presented in Fig. 7.4b. Over 6 hours the surface remained unchanged.

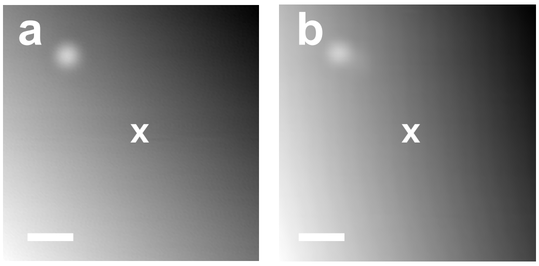

Figure 7.5 – Surface stability during measurement. a) and b) constant current images recorded before (a) and after (b) measurements shown in Fig. 7.4b. U = 3 V, I = 100 pA, scale bar 1 nm.

Occasionally, during data acquisition at very high set-points (a few hundred nA) the tip may deposit a single atom or a cluster, a process that appears as a step in the z trace. We have found that for the same junction parameters (bias and current set-point), the bunching on top of such an adsorbate is reduced as compared to the pristine metal surface. Such an effect possibly arises due to the increase of the tunnel gap on top of an adsorbate that changes the size of the plasmonic cavity, leading to reduced interaction.

7.4 Mechanism of photon pair production

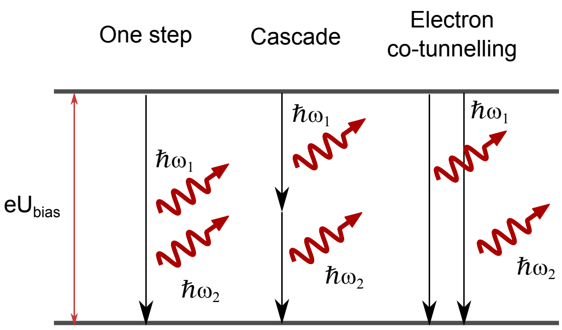

Figure 7.6 – Possible mechanisms for photon pair production.

There are several mechanisms that may lead to photon super-bunching as observed. In the first step, they can be divided into processes originating from single or multiple electron inelastic tunnelling events (see Fig. 7.6) occurring within the temporal limit of the experiment (50 ps). The latter process can occur for instance due to fluctuations of the tunnel junction, like vibrations of atoms at the tip in the ps and sub-ps range. However, fluctuations and instabilities of that sort occur at higher, rather than lower current set-points when bunching is best observed.

To prove that electron co-tunnelling is not the driving mechanism of the photon pair creation we performed measurements with optical filters inserted in front of both SPADs. The applied bias and the cut-off energy of the filters were chosen such that only photons of energies fulfilling $\hbar\omega > \frac{eU_{bias}}{2}$ condition can be detected. This is assured by applying 4 V and inserting shortpass filters with a cut-off wavelength of 600 nm that corresponds to 2.07 eV (see Fig. 7.7a). A correlation measurement in this configuration is presented in Fig. 7.7c, where no bunching is observed. For comparison, a measurement at the same conditions but without shortpass filters is shown in Fig. 7.7b in which clear bunching is observed. If the photon pairs were produced as a result of electron co-tunnelling, bunching should be observed for conditions when the energy of the pair exceeds eU_{bias}. Since it is not the case, we conclude that photon pairs are produced upon single electron inelastic tunnelling. This argument is further supported by the fact that bunching is observed in the bias range that corresponds to twice the detection range of our set-up. For photon pairs due to co-tunnelling the super-bunching would rather coincide with the emission maximum around 3 V (see Fig. 7.1c) and be observed at lower bias range (~ 1.2 V - 3 V).

In the case of photon pair creation in a one electron process ($1e \to 2\gamma$) the photons may be created either in a single step, or as a result of a cascade of events (see Fig. 7.6). Let us assume k_1 to be the quantum efficiency for emitting a single photon, k_2 for emitting a photon pair

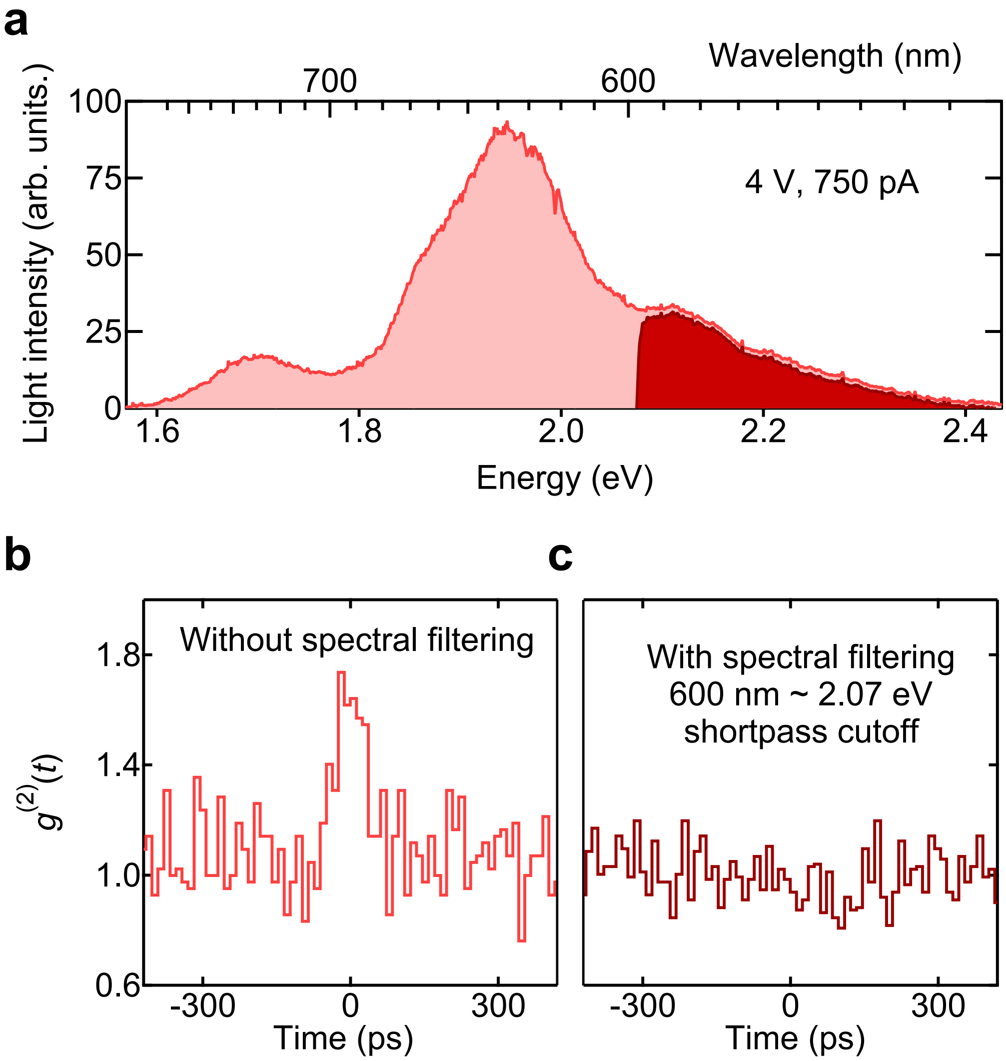

Figure 7.7 – Bunching with bandpass filters. a) Optical spectrum of the emitted light at U = 4 V, I = 750 pA, the dark red part indicates the part of spectrum that reaches the SPADs after spectral filtering (2 shortpass filters with a cut-off of 600 nm). For reference on the measurement set-up see Fig. 2.9. b) and c) Correlation measurements without (b) and with (c) filters. Bunching is absent when the total energy of photons reaching the SPADs is higher than eU_{bias}.

and $k_2 \ll k_1 \ll 1$. Using these rates we can write the number of respective events per second that contribute to a correlation measurement as seen in Fig. 7.2 and Fig. 7.3a. The accidental coincidences (the correlation baseline) occur because of the uncorrelated emission due to two tunnelling events separated in time, where each of these events is detected $N_1 = Ik_1\eta/e$ times per second with η being the overall detection efficiency. Thus, the number of accidental correlations per second $\hat{N}_2$ is:

$$\hat{N}_2 = N_1^2\tau = \left(\frac{Ik_1\eta}{e}\right)^2 \tau \tag{7.1}$$

with τ being the time bin width of the correlation measurement (12.2 ps).

The number of true coincidence events N_2 is:

$$N_2 = \frac{Ik_2\eta^2}{e} \tag{7.2}$$

As the absolute detection efficiency cannot be measured we can analyse a value independent of that parameter:

$$\frac{N_2}{\hat{N}_2} = \left(\frac{e}{I\tau}\right)\left(\frac{k_2}{k_1^2}\right) \tag{7.3}$$

In a cascade process for two events that have the same efficiency it follows that $k_2 = k_1^2$. To verify if this applies, we take the measurements presented in Fig. 7.2, where the total number of true coincidences is $\mathrm{N}_2 \cdot T = 2620$ (obtained by integration between ± 1 ns), number of accidental coincidences $\hat{N}_2 \cdot T$=18.6, I = 20 nA, τ=12.2 ps and obtain that $k_2 = 215k_1^2$. This constitutes an inconsistency higher than two orders of magnitude and precludes the cascade mechanism.

Moreover, if we compare the current dependencies shown in Fig. 7.3b we see that:

$$\hat{N}_2 = \left(\frac{Ik_1\eta}{e}\right)^2 \tau \sim I^{2.95} \tag{7.4}$$

implying that $k_1 \sim I^{0.475}$. On the other hand:

$$N_2 = \frac{Ik_2\eta}{e} \sim I^{1.24} \tag{7.5}$$

and thus $k_2 \sim I^{0.24}$. For a cascade process to be the driving mechanism $k_2 \sim k_1^2 \sim I^{0.95}$ should occur. Together with the fact that the exponent of the power law for true coincidences is half of the exponent of the power law for accidental coincidences (that are due to two independent tunnelling events), we conclude that the photon pairs are created in a one-step $1e \rightarrow 2\gamma$ process.

Photon pair creation may be driven by the intrinsic nonlinearities of the tunnel junction such as the tip-sample asymmetry, strong electric fields and a small volume where the light-matter interaction occurs. One possible process that may occur is the spontaneous parametric down-conversion [256]. Such $1e \rightarrow 2\gamma$ process complements another non-linear mechanisms observed in metal-metal tunnel junctions where few electrons interact via surface plasmon polaritons resulting in $2e \rightarrow 1\gamma$ and $3e \rightarrow 1\gamma$ luminescence [257–259], which will be discussed in more detail in the next chapter.

7.5 Conclusions

The most basic tunnel junction consisting of two noble metal electrodes is a reliable source of photon pairs. We observe photon super-bunching at high bias voltages (3-6 V) and study the current, bias and topography dependence. By a careful analysis of these dependencies, we find that the photon pairs are produced by inelastic tunnelling of a single electron that distributes its energy to two photons, a process that occurs in a single transition.

Such a nanoscale photon pair source can be used to perform quantum information processing with atomic-scale precision. Heralded photon experiments are now possible in nanocircuits and can be likely extended to operations requiring entangled photons.

8 Dynamics of atomic point contacts

The plasmonic enhancement occurring at the nanoscale, as discussed in Section 2.2, apart from being utilized to amplify light generated from nanostructures, can be used to efficiently couple incoming radiation. This coupling can be used to perform spectroscopic measurements with a precision of a few nm, reaching the scale of individual molecules. The signal from chemically sensitive Raman scattering can be efficiently amplified using either plasmonic nanoparticles in the vicinity of the investigated molecules in surface-enhanced Raman spectroscopy (SERS) or a tip of a scanning probe microscope positioned above the molecule of interest in tip-enhanced Raman spectroscopy (TERS) [70, 71, 260–264]. Both of these techniques have been proven to resolve vibrational spectra of individual molecules. A common issue in such measurements is the blinking of the recorded light intensity, occurring on the scale of seconds and minutes, which can be attributed to fluctuations in the plasmonic enhancement or configuration of the molecule in the nanocavity formed between the adjacent nanoparticles or the tip and the surface [71, 265–268]. Recently, the so-called picocavities have been studied using SERS and it has been found that the position of individual atoms in the cavity can be critical for the detection of a single-molecule signal [25] . Therefore, detailed studies of fluctuations in plasmonic atomic-scale junctions are crucial for understanding the dynamics occurring in nanoscale spectroscopies.

Atomically precise junctions can be routinely addressed using the tip of an STM approaching a single adatom on a surface down to the contact regime. Such junctions emit light due to the excitation of surface plasmons and are known to exhibit overbias emission, *i. e.* emit light with an energy higher than the applied energy level difference in a process reciprocal to the photon pair creation presented in Chapter 7. In the following, we study such overbias emission and utilize the time-resolution of STML to follow the fluctuations of its intensity in real time. In this way, we show that STML is an ideal tool to probe the plasmonic enhancement and relate its variation to the dynamics of atomic arrangements in the vicinity of the junction.

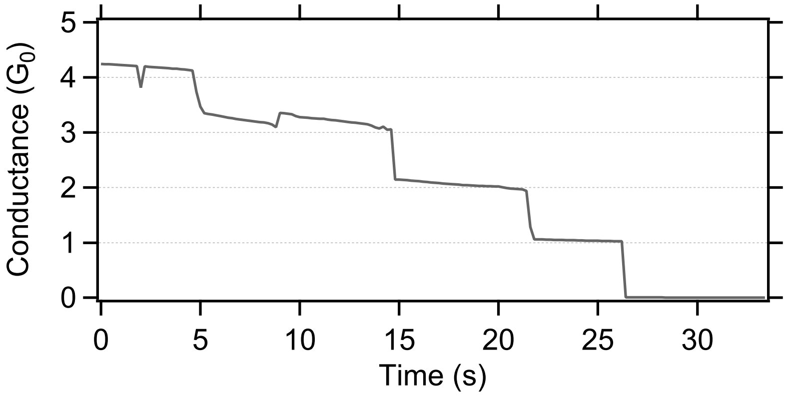

Figure 8.1 – Conductance quantization. Conductance trace recorded during STM tip retraction with a speed of 5 pm s^{-1}. Prior to the retraction, the contact was formed by a slight indentation in the sample. Au-Au junction, U = -0.8 V.

8.1 Atomically precise contacts

Since its early days, STM has been considered as a potential tool to perform manipulation on the ultimate scale of individual atoms. At first used to arrange atoms on the surface [33, 34], later it was employed to electrically contact single atoms [269] and deposit them in a controlled manner [270]. As a result, STM became an important tool to characterize properties of conductors as thin as a single molecule or atom, complementing other methods such as mechanically controllable break junctions (MCBJs) [271].

When a conductor is narrowed down to a diameter of few atoms, which is much smaller than the mean free path of the electrons, the transport through such a constriction can be described as ballistic. Using the scattering approach, the conductance G in such a system can be written in terms of the Landauer expression:

$$G = \frac{2e^2}{h} \sum_i T_i \tag{8.1}$$

where T_i defines the probability of the electron being transferred through eigenchannel i of the system. $\frac{2e^2}{h}$ is usually referred to as a conductance quantum G_0 and used as a unit to express the conductance. The number of transmission channels present in atomic-sized metallic contacts can be estimated to be $N = (\frac{k_F a}{2})^2$, where k_F is the Fermi wave vector and a is the contact radius. For metals such as gold, copper or silver this value is close to 1 in a single-atom junction, indicating that individual atoms correspond to individual transmission channels. The number of channels may be also estimated from the number of valence orbitals, which is 1 for Au. Therefore, a single atom contact with a transmission coefficient close to 1 should have a conductance of $1G_0$ and subsequently 2 G_0, 3 G_0 for 2, 3 atom contacts, which has been found to occur for Au. However, one has to note that the number of channels depends on the material and the exact atomic geometrical configuration of the junction [271].

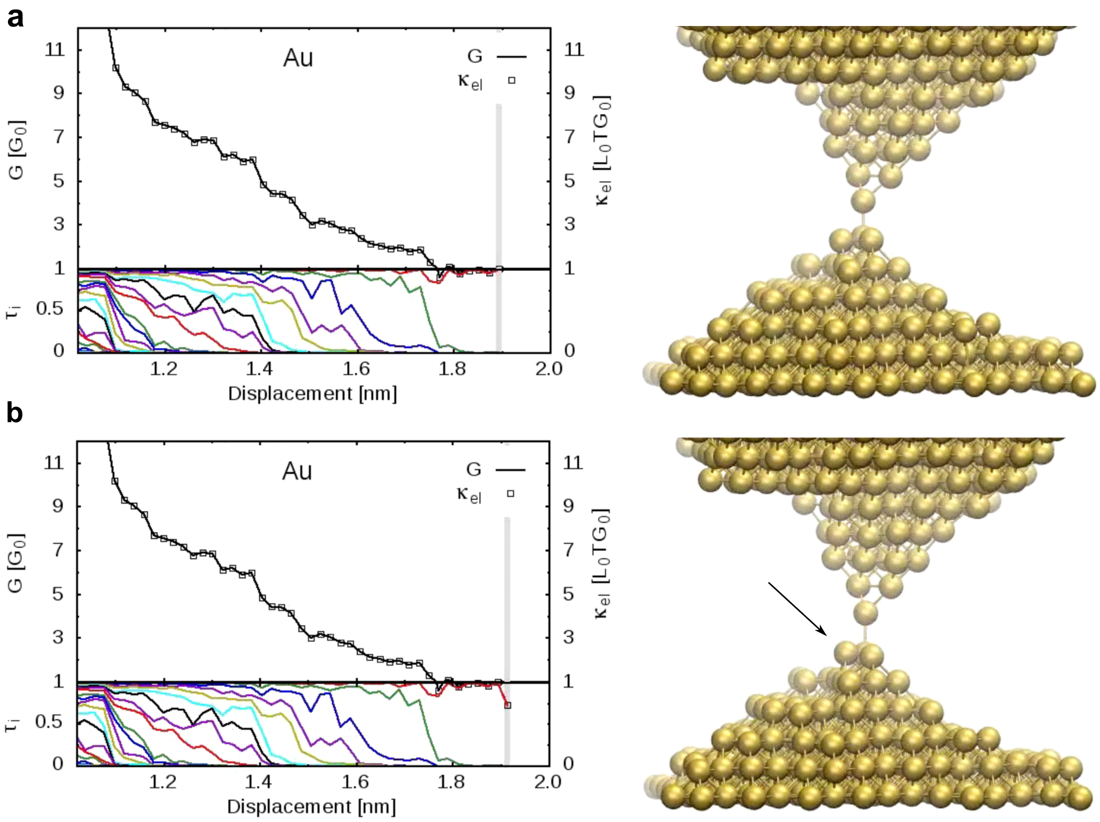

Figure 8.2 – Numerical simulation of an Au point contact. a) and b) show two consecutive steps of the calculation in which the atomic structure is allowed to evolve from full contact to breaking. The transport properties (total electrical and thermal conductance, and the relative contributions of the channels) of the junction are calculated for each step and plotted on the left. The values for the structures shown on the right are indicated by the grey bars. Adapted from Ref. [272]. Reprinted with permission from AAAS. Modified with permission from the Authors.

As a consequence of this conductance quantization, an experiment in which an STM tip first is indented into the sample and later retracts forming narrower and narrower junction should exhibit steps in a conductance trace. Indeed it is the case, as presented in Fig. 8.1 using a junction formed by an Au tip and Au(111) surface at 4 K. Upon constant retraction of the tip, the conductance changes in steps (of 1 G_0) with plateaus around 4 G_0, 3 G_0, 2 G_0 and 1 G_0. The steps can be assigned to atomic rearrangement of the junction resulting in the constriction of the contact. When analysed in detail, some deviations from the integer values of conductance are visible. They appear as step-wise changes (see the step around 10 s) or as a smooth change (between 15 and 20 s). From eq. 8.1 it is evident that these variations can be related to the number and transmission probability of the channels involved in the transport. Numerical simulations of Au point contact junctions reveal that even slight atomic rearrangement in the vicinity of the junction leads to a change of transmission over a stable constriction, for instance consisting of one atom. Snapshots of such a simulation done by

Cui *et al.* [272] are presented in Fig. 8.2. The difference in atomic structure between Fig. 8.2a and Fig. 8.2b is only slight (one of the atoms that relocated is indicated by an arrow in Fig. 8.2b), however the conductance changes by a factor of 0.2 G_0 and the transmission probability of the only contributing channel changes by the same factor. For a more insightful view, we refer the reader to the original animations presented in the Supplementary Materials for Ref. [272]. If more than one channel is involved in the transport, a change in conductance may be related to a change in relative contributions of each channel, which also occur due to atomic rearrangement in the junction, or in its close vicinity [273]. In general, these variations in transmission probability and thus conductance are a result of the electron wave function being scattered and reflected at the imperfections of the junction [271]. Similarly to measuring and calculating transport properties, the variation in the atomic structure of the contacts can be probed by measuring the forces during the stretching of an atomic contact [274].

8.2 Overbias STML

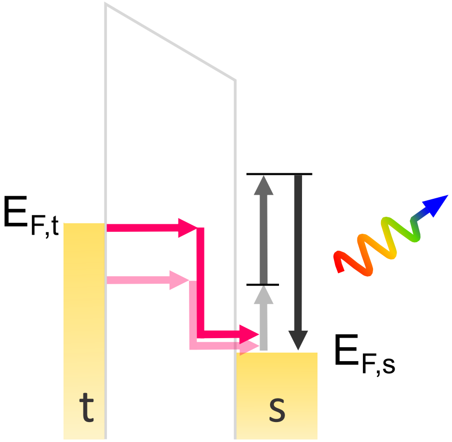

Figure 8.3 – The principle of overbias emission due to the electron-electron interaction.

The energy of the photons emitted from a tunnel junction biased by voltage U is expected to follow the relation $h\nu \leq eU$, as eU constitutes the maximum energy one electron can lose during an inelastic tunnelling process to a tip-induced plasmon. However, a number of studies reported that this relation is not always obeyed. Electroluminescence at energies higher than the applied potential difference was for the first time reported by Pechou *et al.*, who performed experiments at currents in the nA regime using an ambient STM set-up [275]. Later it was reported repeatedly at metallic tunnel junctions [257, 259, 276, 277], atomic contacts [258, 278] and atoms [279] or molecules adsorbed on surfaces [63, 98, 280, 281]. Apart from the STM studies, measurements performed in electromigrated junctions [282] and nanoclusters [283] showed similar characteristics. Such luminescence is usually referred to as overbias emission and is characterized by low efficiency in the range of $10^{-8} - 10^{-7}$ emitted photons per injected electron in the nA - μA regime [257].

The experiments performed on metallic junctions can be explained in terms of coherent electron processes as suggested recently [259, 284–286]. In such models, a few electrons tunnel coherently and due to high-order contributions to the shot noise are able to excite a plasmon of energy exceeding the energy provided by a single electron ($2e \rightarrow 1\gamma$ and $3e \rightarrow 1\gamma$ light, depending on the minimum number of electrons involved). That kind of process is schematically illustrated in Fig. 8.3. As an alternative explanation, blackbody radiation resulting from heating of the electron gas has been proposed [278, 282].

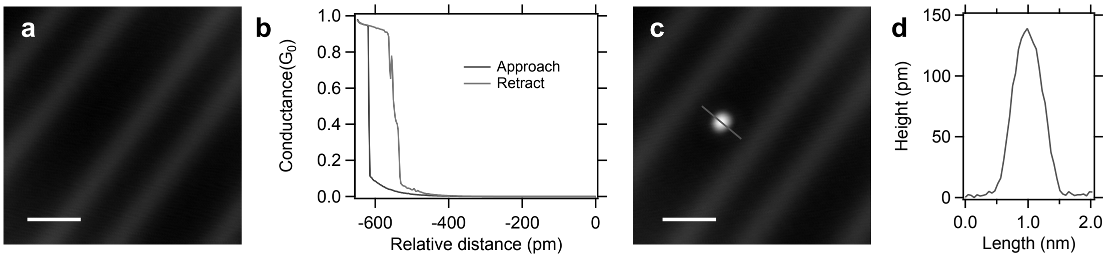

Figure 8.4 – Deposition of individual Au atoms. a) Image of a defect-free Au(111) surface, I = 100 pA, U = 1 V. b) Approach and retract curve resulting in deposition of a single atom, U = 1 V, current set-point 100 pA. c) Scan of the same area as in a) after atom deposition. Scale bars 2 nm. d) Height profile showing a cross section (marked in c)) over a single deposited atom.

As described in Section 2.2, plasmon modes in the junction are excited due to the shot noise of the current [85]. Shot noise is also relevant in atomic contacts. It is expected to vanish in a perfect transmission channel because the electron will be always transmitted when it enters an open mode and there is no reason for fluctuations to occur [287, 288]. As the STML can be viewed as a probe for shot noise, the light intensity was expected to be reduced at a single-atom contact, which indeed was observed by Schneider, Schull and Berndt [258]. In this study, the light intensity is observed to be reduced at conductances close to integer values of G_0. This reduction can be described by the Fano factor:

$$F = \frac{\sum_i T_i(1-T_i)}{\sum_i T_i} \tag{8.2}$$

The observed variation is a smooth function of conductance (varied by approaching the tip towards the surface) and does not exhibit abrupt changes.

8.3 Time-resolved STML from atomic point contacts

As described above, even slight rearrangements of the atomic structure in point contact junctions can result in a significant change in the transport properties. Therefore, it is interesting to investigate the influence of such arrangements in the plasmonic enhancement and the resulting luminescence intensity. Recent studies report that the plasmonic enhancement in structures separated by less than 5 Å cannot be properly described by classical plasmonics and quantum plasmonics models have to be used [289–291]. The plasmonic properties at the smallest possible separations were studied theoretically and revealed that the plasmonic response of the system depends on the shape of the involved particles [292] and their atomic structure [293–298] plays a key role.

To investigate these properties, we prepare an atomic scale contact by depositing individual atoms on the surface, which can be controllably achieved by approaching the tip until contact with a surface is formed [270]. Fig. 8.4 shows the details of this procedure. First, the surface

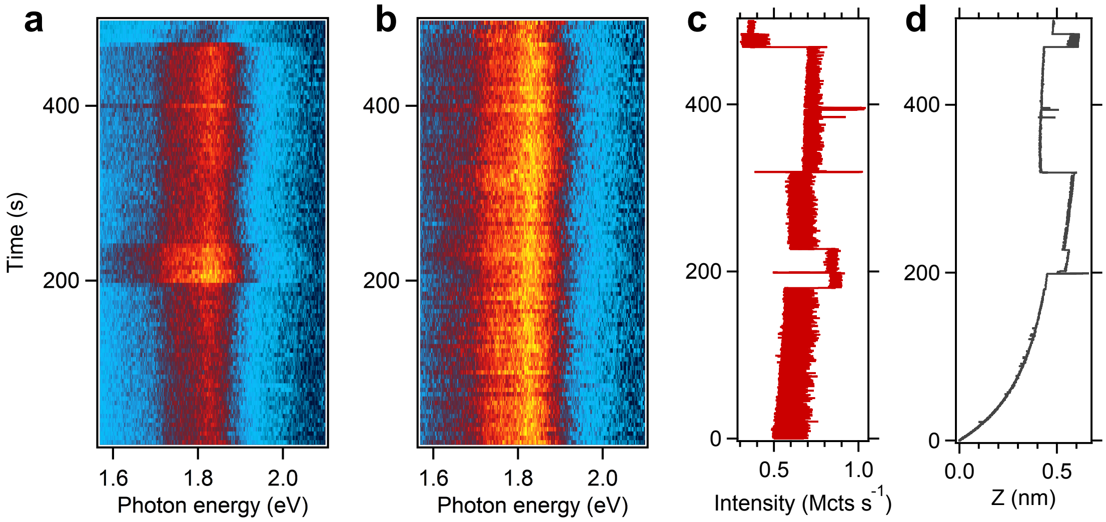

Figure 8.5 – Luminescence fluctuations at 1 G_0. a) Time-resolved spectra. The plot consists of 100 spectra, each recorded within 5 s integration time. b) Normalized spectra from a). c) and d) Simultaneously recorded light intensity measured by an SPAD and z position, respectively. 20 ms integration time per point in c) and d). The current feedback was enabled during the measurement in order to maintain 1 G_0, U = 1 V, I = 77.48 μA.

is scanned to ensure it is clean and free of defects, as presented in Fig. 8.4a. Next, the tip is moved towards the surface by 650 pm which results in a jump-to-contact event leading to a conductance close to 1 G_0 (Fig. 8.4b). After, the tip is subsequently retracted. In the next step, the surface is rescanned to confirm successful atomic deposition, as shown in Fig. 8.4c. We find this procedure to be highly reproducible, occasionally depositing a small cluster of few atoms, which can be identified by a higher maximum conductance during the approach-retract curve and higher topographic appearance. Since both the tip and the sample are made out of Au, the deposited structures consist of Au atoms only. We monitor the plasmonic spectrum before and after deposition, and find that the atom transfer from the tip to the surface does not alter the shape of the spectrum.

After such deposition, we can form the contact, maintain the desired conductance using the feedback loop of the STM and record the light intensity and spectra as a function of time in a stable manner. Fig. 8.5 presents such a measurement performed at a single-atom contact (1 G_0), which enables us to access the dynamics of atomic junctions in real time. We observe fluctuations in the luminescence, as seen in the time-resolved spectra (Fig. 8.5a) and integrated light intensity (Fig. 8.5c). Interestingly, the spectral shape does not change over the measurement, as evident when plotting the spectra from Fig. 8.5a after normalization (Fig. 8.5b). The fluctuations in the luminescence can have both smooth and step-wise behaviour. A smooth evolution of the light intensity can be observed starting from the beginning, until 180 s of the measurement and is on the order of 5 %. Right afterwards, we observe a step-like change on the order of 40 % of the integrated luminescence. Variations of that sort occur also later during the measurement. Since we maintain the current feedback, we are able to follow

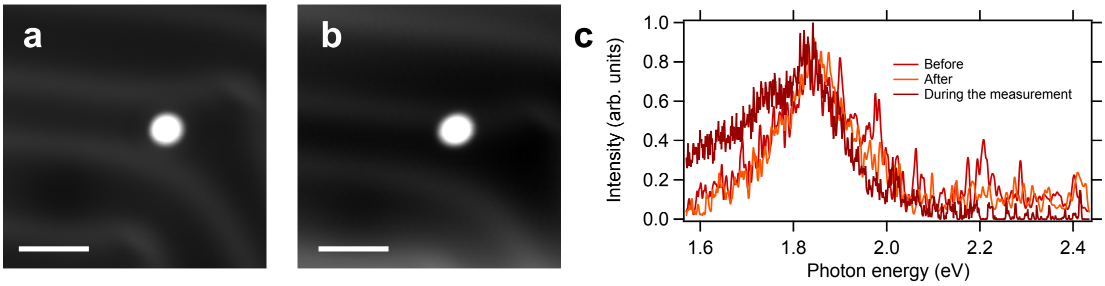

Figure 8.6 – Stability of the point contact junction. a) and b) Images recorded before and after measurements in Fig. 8.5, which were performed on top of the deposit. Scale bars 2 nm. c) Normalized reference spectra recorded before and after measurements in Fig. 8.5, U = 3 V, I = 100 pA. One of the spectra from Fig. 8.5 is presented for comparison, U = 1 V, I = 77.48 μA, t = 5 s.

the relative change in the z position (Fig. 8.5 d) and correlate it with the luminescence trace. What we observe is that the abrupt changes in the light intensity occur simultaneously with a change in the z position, which can be attributed to the atomic rearrangements in the junction. Remarkably, there is no correlation regarding the direction of the variations - a retraction of the tip may coincide with both an increase and decrease in the light intensity. There is also another type of fluctuation in the luminescence that can be noticed. During periods of constant average intensity, the light intensity varies on the ms timescale. The amplitude of this fluctuation changes after each step-wise change. To further investigate the different types of fluctuations described above, we performed measurements for different bias voltages, also at a single-atom contact (1 G_0), where we observe a similar behaviour.

We would like to note that this particular measurement was performed on a cluster consisting of probably 3 Au atoms, one of which was directly contacted during the formation of the atomic junction. To validate the stability of the junction we rescanned the surface after the measurements and recorded the optical spectra (Fig. 8.6). We found that the cluster only slightly moved during 5 min of measurement in contact and the plasmonic modes were preserved. However, the spectrally integrated intensity varies in the range 5-20 % when measured before and after similar measurements. For data gathered at negative bias voltages, we noticed that the stability of the junction is reduced and after the measurement, we find that we deposited clusters with a size of a few nm.

In the next measurement, we manually approached (in steps of 1 pm) an individual atom deposited on the surface until a single atom contact was formed (conductance close to 1 G_0). Subsequently, we continuously retracted the tip and recorded the conductance, spectrally integrated light intensity and optical spectra, which are presented in Fig. 8.7. In this configuration, we can directly correlate the fluctuations in the luminescence with the fluctuations in the conductance. The measurements were performed in an extremely gentle fashion, each time the tip was continuously retracted (in steps of 3.5 pm) by 350 pm in total and if the contact was not yet broken, this procedure was repeated. The optical spectra were recorded

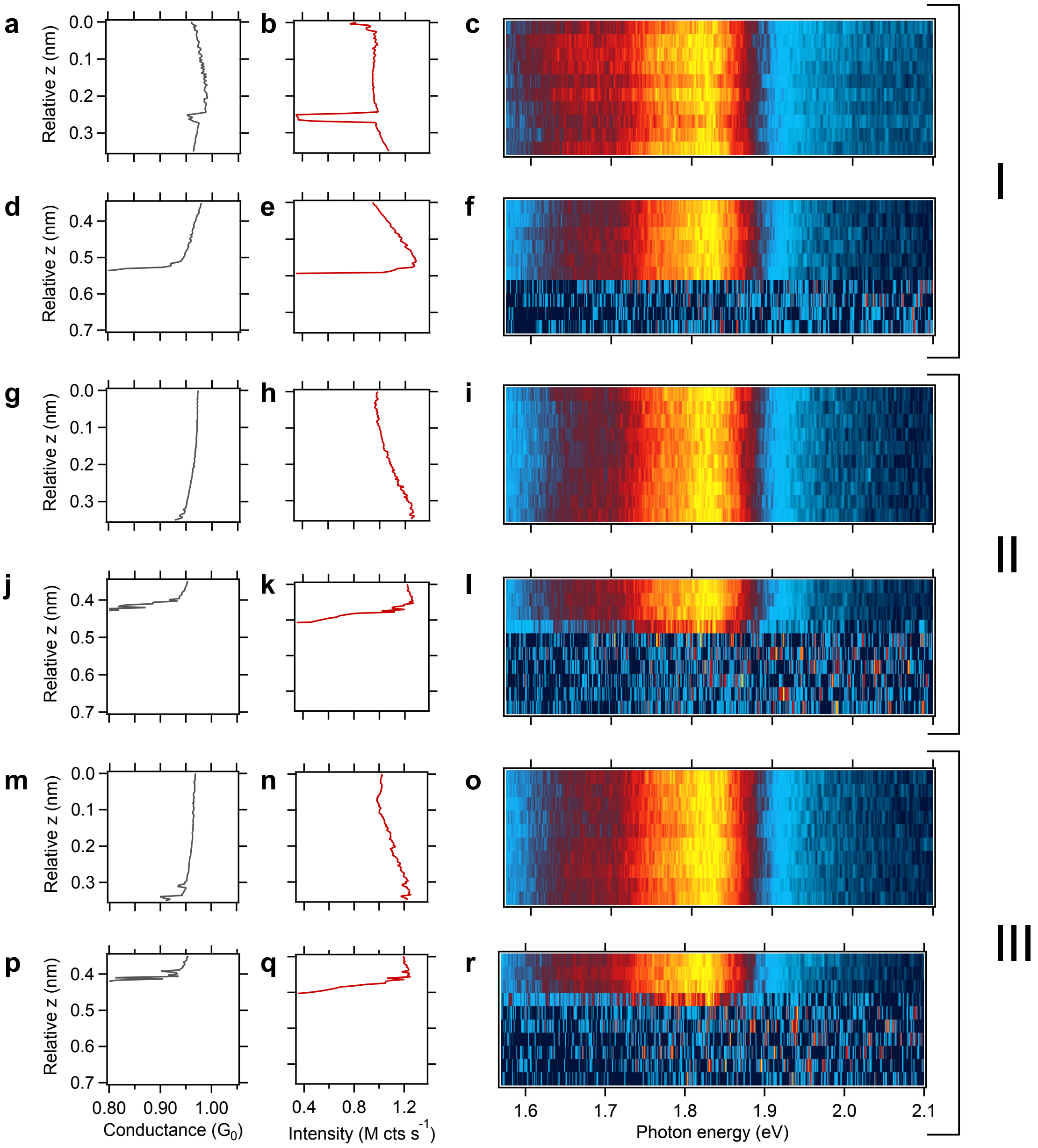

Figure 8.7 – Luminescence fluctuations during retraction from an atomic contact. The contact was formed by a manual approach towards an Au adatom located on the surface until a single-atom contact was formed (conductance close to 1 G_0). The left column shows conductance traces, the middle one spectrally integrated light intensity, the right spectra normalized to the maximum. Each spectral plot consists of 10 spectra, each recorded within 5 s. The whole figure consists of 3 measurements (I, II, III), separated in two parts each (for example a)-c) and d)-f)) accounting for the start of the stretching and the breaking. In each part, the tip was retracted by 350 pm. The surface was inspected in between each measurement (I, II, III) and the investigated atom was approached once again. U = 1 V.

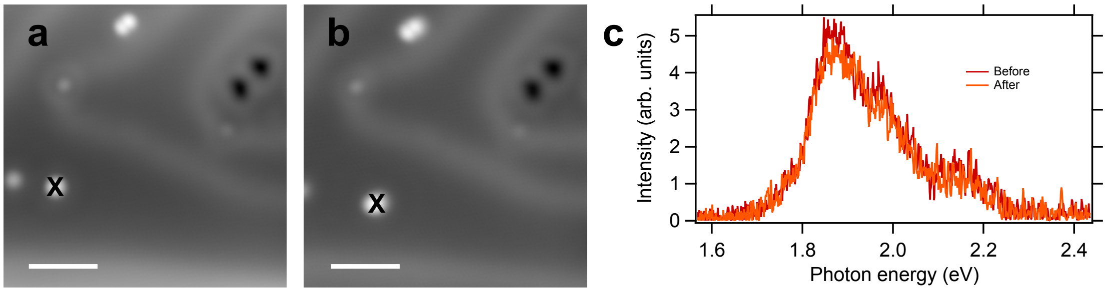

Figure 8.8 – Stability of a single atom on the surface during atomic-contact measurements. a), b) Topographies recorded before and after measurements presented in Fig. 8.7, which were performed on the position marked by X. U = 1 V, I = 100 pA, scale bars 2 nm. c) Optical spectra recorded before and after measurements presented in Fig. 8.7, U = 3 V, I = 100 pA.

during the retraction. We found that usually the contact was lost after a total retraction of approx. 450 pm. When the contact was broken, the surface was rescanned and a plasmonic spectrum was recorded in order to ensure that no change occurred neither to the tip nor to the sample, as presented in Fig. 8.8, except a slight displacement of the investigated atom and some adsorbates in the vicinity. The shape of the spectrum does not change, however, there is a permanent alteration in the light intensity on the order of a few percent (8 % in this case). Afterwards, the same atom was approached once again and the measurement was repeated. This procedure was reproducible and the same atom could be investigated multiple times. Fig. 8.7 shows 3 measurements (labelled as I, II and III) performed on the same atom. The tip was stabilized for 15 h prior to the series.

Similarly to the measurements presented in Fig. 8.5, the luminescence evolved in both a smooth and a step-wise manner. Again, the spectral shape does not change during the measurement. By correlating the luminescence and conductance, we observe that in contact an increase in the conductance does not always coincide with an increase in the light intensity. However, in the transition to the tunnel contact, a decrease in the conductance always results in a decrease in the luminescence. The deviations from the integer value of conductance during the measurements may occur due to the series resistance of the leads, which is not compensated and can be in the order of a few hundred Ω [271].

The fact that the plasmonic modes do not change and the surface remains clean during measurements presented in Fig. 8.5 and Fig. 8.7 indicates that the observed variations in the luminescence are not related to significant changes in the structure of the atomic contact and its vicinity. Therefore we can study contacts, which are closer to a realistic junction between two plasmonic nanoparticles in a nano- or pico- cavity, which do not have a well-characterized surface. We performed measurements similar to the MCBJ technique by repeatedly forming the contact at 5 G_0 and retracting the tip while recording the conductance and luminescence. Selected traces are presented in Fig. 8.9. As expected, we observe steps in the conductance, which occur often close to the integer values of G_0. Similarly to the previous experiments, fluctuations in the conductance coincide with fluctuations in the luminescence, which can change its intensity by up to a factor of 3 (Fig. 8.9d) and have both step-wise and smooth character.

Having studied the dynamics of fluctuations in the luminescence from atomic point contacts in various configurations (Fig. 8.5, 8.7 and 8.9) we can now discuss the possible mechanisms behind such variations. First of all, we will focus on the smooth changes, where light intensity either decreases or increases with the conductance. The luminescence decreases as the conductance smoothly reaches integer values of G_0, irrespective of the direction (decreasing or increasing towards nG_0). An example of such behaviour can be found in Fig. 8.9d for the displacements between 200 pm and 300 pm. That sort of variation in the luminescence can be interpreted in terms of shot noise reduction close to perfect transmission, as discussed earlier [258]. For high conductances 4-5 G_0 (Fig. 8.9a,d) this effect is not pronounced anymore, because many channels contribute to the transport even for Au-Au junctions [271] and the shot noise reduction described by eq. 8.2 is obscured. Occasionally, we found deviations from this relation, as evidenced in Fig. 8.9b around 1 G_0, where light intensity increases as the conductance approaches G_0, which may be related to a presence of multiple transport channels in the junction. During the transition to the tunnelling contact (Fig. 8.7e,k,q and Fig. 8.9), as expected [22, 258], the luminescence systematically decreases.

Apart from the smooth changes in the luminescence, we observe also step-like fluctuations. They can be easily correlated with the steps in the conductance, however, the relative change of the luminescence may reach 300 %, whereas the conductance changes only by a factor of 10 % (see Fig. 8.9d as an example). Here, there is no clear correlation between the directions of changes, in contrast to the smooth variations related to the shot noise. As described in Section 8.1, the changes in the conductance in atomic contacts are related to the atomic rearrangement at or in the vicinity of the junction. Similarly, the changes in the plasmonic enhancement can be also related to the atomic structure [25, 293–298]. Studies by Rossi *et al.* [295] and Marchesin *et al.* [297] report that the fluctuations in the plasmonic mode intensity coincide with the changes in the conductance. This leads us to the conclusion that the fluctuations in the luminescence may occur because the atomic structure of the contact changes resulting in different plasmonic enhancement. The calculations show also a shift in the mode energy, however, in our measurements the spectrum is preserved. The variations could be potentially a result of different transmission channels contributions and a change in the shot noise. However, the fact that we observe a change in the plasmonic enhancement before and after formation of contact (Fig. 8.8) indicates that indeed the structure of the tip changes and variations in the transmissions of conductance channels may contribute only in a minor way. Sometimes a step in the light intensity occurs with no, or insignificant change in the conductance (Fig. 8.5 and Fig. 8.9b). Such an effect may be explained by an atomic rearrangement further away from the junction, thus resulting only in a minor change in the transmission.

These step-like fluctuations may be correlated with the frequently observed blinking in SERS and TERS measurements. So far, there have been many mechanisms proposed to explain this

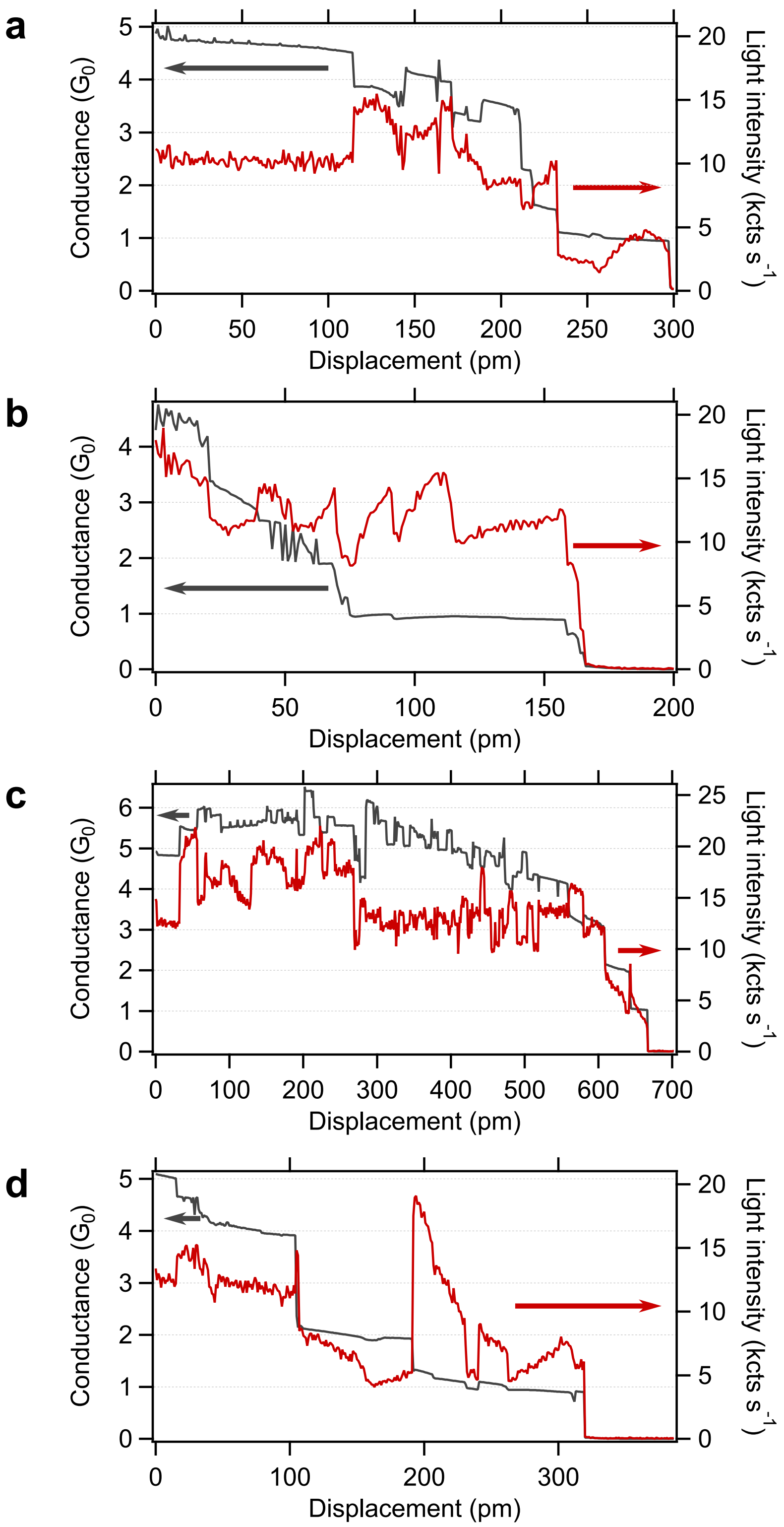

Figure 8.9 – MCBJ-like measurements. a)-d) Conductance (black) and light intensity (red) recorded during retraction (with a speed of 5 pm s^{-1}) from four different point contacts, which were formed by approaching the tip until a conductance of 5 G_0 was reached. U = -0.8 V.

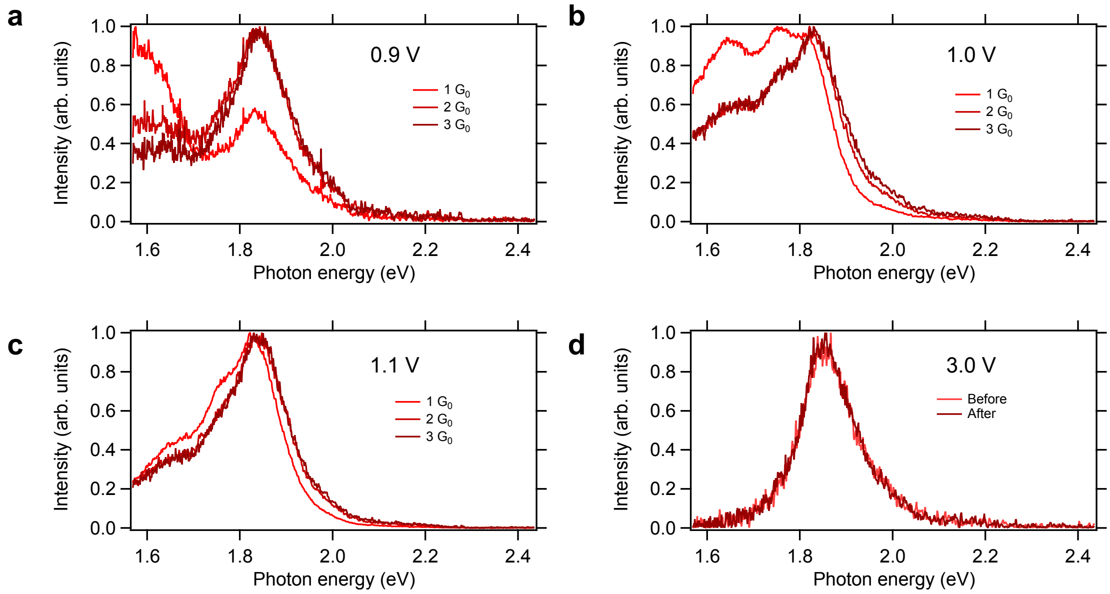

Figure 8.10 – Optical spectra as a function of conductance and bias. a)-c) Normalized optical spectra as a function of bias and conductance, with the values indicated next to the traces. The current feedback was enabled during the measurements. d) Normalized reference spectra recorded at tunnelling conditions before and after the measurements presented in a)-c), U = 3 V, U = 100 pA

effect, including changes related to the investigated molecules (diffusion, absorption position, contaminants) [71] or charge transfer [265]. As another likely explanation, fluctuations in the atomic structure of the plasmonic junctions have been invoked, especially for blinking that does not involve relative changes in the vibronic peaks [71, 268, 299]. With our studies, we are able to follow these mechanisms in real time in a clean plasmonic contact, where no adsorbate, but only a change in the plasmonic enhancement (preserving the plasmonic mode) can be involved. Motion in the atomic junction is also responsible for the formation of the "picocavities" and the selection rules for the molecule in the cavity [25].

8.4 Optical spectroscopy of light emitted from point contacts

The luminescence observed in measurements presented in Fig. 8.5, 8.7 and 8.9 has an overbias character. It can be described as $2e \rightarrow 1\gamma$ emission for Fig. 8.5 and 8.7 (U = 1 V, the spectra shows contributions until 1.95 eV), whereas the data gathered at U = -0.8 V has also a $3e \rightarrow 1\gamma$ contribution. The advantage of studying overbias emission is that the power injected into the junction is lower than for measurements performed at for example U = 2 V leading to the excellent stability we encounter during the measurements (Fig. 8.6 and 8.8). We observe some heating effects in the junction, as evidenced by a tip retraction while in contact (Fig. 8.5d). However, the very small expansion of the junction (< 1 nm in 500 s) indicates that the resulting temperature is too low to explain the observed luminescence in terms of blackbody radiation.

In fact, in this study, we utilize the fact that there is power dissipation in the junction, leading to atomic motion in the junction (located in a 4 K cryostat) that occurs on a timescale that we can follow in both conductance and luminescence measurements.

To study overbias emission it is interesting to inspect the optical spectra in more detail, both as a function of the applied bias and the conductance of the junction. Such measurements performed with an enabled feedback loop at integer values of G_0 are presented in Fig. 8.10. The overbias emission is clearly resolved, with components reaching up to $3e \rightarrow 1\gamma$ (Fig. 8.10a,b). The feature around 1.84 eV is related to the plasmon mode of the junction as compared with a reference spectrum recorded in tunnelling conditions (Fig. 8.10d). Interestingly, there is a difference between spectra recorded at a single atom contact (1 G_0) and multiple atom contact (2, 3 G_0). For all 3 bias voltages shown, the spectrum at 1 G_0 has a more intense component in the low energy part of the emission than the data gathered at 2 and 3 G_0. Such an effect may be understood in terms of coherent electron-electron processes. When only one channel is open, which is often the case at 1 G_0, it is less likely for an electron to interact with another charge via plasmon excitation. Thus, it is more difficult to observe light due to many-electron interaction. The relative contributions depend also on the energy provided by one electron (applied bias). As evident in Fig. 8.10, the higher the applied bias, the closer the shape of the spectrum to the ones observed at higher conductances. At these conditions, there is more than one transmission channel open and the interaction appears to be enhanced. Also, for 1 and 1.1 V the spectra recorded at 2 and 3 G_0 are basically identical. The observed variations in the spectra as a function of conductance may also partially contribute to the changes in the total light intensity shown in Fig. 8.9.

8.5 Conclusions

In this chapter, we presented how to follow in real-time the fluctuations in luminescence from atomic-scale junctions. By using STM manipulation we deposit single atoms on the surface and contact them with the tip, forming few atom constrictions. We utilize here the overbias luminescence resulting from plasmon mediated electron-electron interactions, follow the changes in its intensity and observe a constant spectral shape. We can correlate them with the variations in the conductance, which leads us to a conclusion that the changes in the light intensity occur due to the dynamics of single atoms in the junction and its vicinity. Such changes of the plasmonic luminescence at the atomic scale may be related to the blinking observed in nanoscale Raman spectroscopies (SERS and TERS). Further theoretical studies to support this claim are thus of interest.

9 Conclusions and outlook

Studies presented in this thesis reveal the potential of STM coupled with time-resolved light detection as an ultimate tool to study ps-pm dynamics of systems as small as individual charges, atoms, and molecules. In the following, we will briefly summarize the results of this research and present its potential perspectives.

Instrumental improvements

In this thesis, we further developed and employed different approaches to STML with time resolution: voltage pulse excitation, photon correlations with one time-resolving photon detector, photon correlations using two detectors and time-resolved optical spectroscopy. The limits of these techniques can be pushed forward by improving the instrumentation used, some of which has been already accomplished in the course of this thesis. First of all, the previously used SPADs have been replaced by detectors with time resolution < 50 ps and the STM wiring has been improved to provide a better high frequency performance for the voltage pulses arriving at the tunnel junction. With these advances, studies of charge dynamics in C_{60} thin films could reach 1 ns time resolution and a clear demonstration of photon super-bunching with a resolution of 50 ps became possible.

To further develop the experimental set-up for the future measurements, additional improvements have been made recently. The amplitude of the pulses used in Chapter 4 was limited by the output parameters of the AWG. After introducing a high frequency voltage amplifier, the pulses can be externally amplified by 20 dB, so that amplitudes up to 3 V can be realized. Measurements using voltage pulses can be now combined with time-resolved optical spectroscopy reaching down to few ns using a PI-MAX 4 emICCD camera. The possibilities of photon correlation measurements have been improved as well. So far, photon correlations with one detector were possible down to few µs and the correlations with two detectors were limited by the maximum range of the SPC-130 card (5 µs). It was not possible to explore the full-time regime accessible to the SPADs in a single measurement. With a new multichannel card (Swabian Instruments, Time Tagger Ultra) arrival times from multiple detectors can be recorded and photon time correlations can be measured over 12 orders of magnitude, from ps to s.

Charge and exciton dynamics in organic compounds

As presented in Chapter 4 the dynamics of individual electrons, holes, and excitons can be probed using TR-STML at the scale of one emitter - the smallest possible OLED, which was a long-standing goal of organic electronics [26]. Here, we showed that we can follow the formation and recombination of a single exciton in real time and space, as well as control the rate of this process by tuning the energy barrier at the metal-organic interface.

Such studies can be easily extended to other systems and properties. The excitons in C_{60} have a singlet character (antiparallel aligned electron and hole spins), which decay with ns lifetimes. However, during electrical excitation due to the spin statistics, only 25 % of the excitons are of singlet character, the remaining 75 % are triplets, which are usually not efficient emitters and decay with µs lifetimes [26]. Therefore, it is of great interest to probe with TR-STML how the local structure of the electrodes and emitters affects processes involving both singlets and triplets such as radiative transition, electroluminescence efficiency, charging and intersystem crossing. Measurements of the intensity transients can be extended by the gated optical spectroscopy. Such a combination allows distinguishing different emission modes in the time domain, for instance, the singlet and triplet emission lines and probing their relative interplay and evolution. Using these methods, besides the single molecule studies, it is possible to access the luminescence properties of molecular aggregates with sub-molecular spatial precision. This will allow investigating how the local environment affects the electron-to-photon energy conversion and in the long term enable efficient control over that process. For even larger systems (islands or layers) it is possible to probe singlet fission or exciton diffusion [26]. In such an experiment, the excitons induced locally by the tip migrate at the scale of a few tens of nm and eventually decay radiatively. Non-radiative processes would result in reduced luminescence efficiency and could be probed for instance at different molecular interfaces. Detailed knowledge of these dynamical properties at the molecular scale will help to improve the efficiency of future OLEDs. Additionally, the methods described above are not limited to organic molecules and layers but can be used to study inorganic semiconductors and two-dimensional materials.

Studies of motion at the nanoscale

Apart from charge and exciton dynamics, we also probed the motion at the nanoscale. Chapter 6 showed that we can probe the dynamics of a hydrogen molecule on a Au(111) surface trapped in a shallow potential well and extract the time the molecule spends inside and outside of the tunnelling junction. This motion leads to a modification of the plasmonic luminescence, which results in photon bunching. Studies of such a system are not only relevant for hydrogen storage [226] but open new possibilities for studying adsorbates on surfaces. The limits of the commonly utilized telegraphic noise in the current [125] have been overcome already in the studies presented here that employ a one photon detector reaching the µs regime. However, the use of the new correlation card extends possibilities of probing adsorbate motion down to the ps scale. Such studies are of high relevance for molecular motors so that for instance toggling between different adsorption configurations can be probed in more detail. Another research direction concerns catalysis, because alterations in the reaction rate can be potentially followed.

Correlation measurements constitute an interesting extension of studies presented in Chapter 8. We probed the changes in the plasmonic enhancement, which are related to the motion of individual atoms in the single-atom junction and its vicinity. Some of the recorded intensity vs. time traces showed fluctuations occurring on the scale faster than ms STM electronics, which in the future can be probed by photon correlations. Because now the correlations can be studied from ps to s regime, such a point contact junction is another promising system to resolve even ps fluctuations between two junction configurations. Additionally, the changes in the plasmonic enhancement may be explored in junctions containing molecules or under external illumination in order to understand finer details of processes relevant for TERS. This plasmonic enhancement was studied by observing overbias emission from a tunnel junction, which itself is a process of fundamental importance. It provides information about electron-electron and electron-plasmon interactions in atomic contacts and deserves further studies especially at higher conductances.

Quantum properties of light

Fundamental electron-plasmon interactions play a crucial role in the formation of photon pairs as presented in Chapter 7. We found that a generic metal-metal tunnel junction acts as a source of such pairs converting the energy of one electron to two photons within less than 50 ps in a process reminiscent of spontaneous parametric down-conversion. Since the precise mechanism of this process is not yet clear, it is critical to further extend these studies, for example, to probe photon super-bunching with narrow spectral filtering to study only photons of defined energies. One could expect that some photon energy combinations may be more favourable than others, which would enhance the purity of the source. Another potential research direction involves studies on various adsorbates or layers. Additional layers in between the metallic electrodes such as hexagonal boron nitride could also serve as a protection layer for otherwise unstable tunnel junctions [300]. The quantum nature of the emitted pair also leads to interesting questions, especially those related to a possible photon entanglement. For a down-conversion process, the entanglement is expected to occur for instance in the photon polarizations [301], which can be probed in the so-called CHSH (Clauser-Horne-Shimony-Holt) scheme [302]. It employs four detectors with polarisers and is based on demonstrating a violation of the so-called CHSH Bell's inequality. Additionally, the length of a correlated photon wave packet can be probed using Hong-Ou-Mandel interferometry [303]. Such a measurement requires narrowband optical filtering and proves the indistinguishability of emitted photons by destructive interference.

Another effect that occurs on ultrafast timescales is exciton-plasmon interaction. In Chapter 5 we have shown that the excitonic and plasmonic emission can coexist in C_{60} thin films and be used to control the emission spectrum. These two mechanisms are driven by two different transport channels and therefore may exhibit interesting correlations in the ps time domain depending on the precise nature of the exciton-plasmon interaction. If only one channel can be operant at a time, one would expect anticorrelation between the excitonic and plasmonic emission, which can be separately addressed by optical filtering. On the other hand, a similar experiment performed on molecules adsorbed on a NaCl layer [109–111] should result in an absence of anticorrelation because the two emission channels are likely to be open at the same time.

Bibliography

[1] Brown, R. XXVII. A brief account of microscopical observations made in the months of June, July and August 1827, on the particles contained in the pollen of plants; and on the general existence of active molecules in organic and inorganic bodies. *Philos. Mag.* **4**, 161–173 (1828).

[2] Vale, R. D. The Molecular Motor Toolbox for Intracellular Transport. *Cell* **112**, 467–480 (2003).

[3] Verbrugge, S., Kapitein, L. C. & Peterman, E. J. G. Kinesin Moving through the Spotlight: Single-Motor Fluorescence Microscopy with Submillisecond Time Resolution. *Biophys. J.* **92**, 2536–2545 (2007).

[4] Bigioni, T. P. *et al.* Kinetically driven self assembly of highly ordered nanoparticle monolayers. *Nat. Mater.* **5**, 265–270 (2006).

[5] Koperski, M. *et al.* Single photon emitters in exfoliated WSe2 structures. *Nat. Nanotechnol.* **10**, 503–506 (2015).

[6] Zhang, Q. *et al.* Efficient blue organic light-emitting diodes employing thermally activated delayed fluorescence. *Nat. Photon.* **8**, 326–332 (2014).

[7] Krausz, F. & Ivanov, M. Attosecond physics. *Rev. Mod. Phys.* **81**, 163–234 (2009).

[8] Garg, M. *et al.* Multi-petahertz electronic metrology. *Nature* **538**, 359–363 (2016).

[9] Gaumnitz, T. *et al.* Streaking of 43-attosecond soft-X-ray pulses generated by a passively CEP-stable mid-infrared driver. *Opt. Express, OE* **25**, 27506–27518 (2017).

[10] Eggeling, C. *et al.* Direct observation of the nanoscale dynamics of membrane lipids in a living cell. *Nature* **457**, 1159–1162 (2009).

[11] Mangel, S., Aronovitch, E., Enyashin, A. N., Houben, L. & Bar-Sadan, M. Atomic-Scale Evolution of a Growing Core–Shell Nanoparticle. *J. Am. Chem. Soc.* **136**, 12564–12567 (2014).

[12] Feist, A. *et al.* Ultrafast transmission electron microscopy using a laser-driven field emitter: Femtosecond resolution with a high coherence electron beam. *Ultramicroscopy* **176**, 63–73 (2017).

[13] Leijten, Z. J. W. A., Keizer, A. D. A., de With, G. & Friedrich, H. Quantitative Analysis of Electron Beam Damage in Organic Thin Films. *J. Phys. Chem. C* **121**, 10552–10561 (2017).

[14] Driscoll, R. J., Youngquist, M. G. & Baldeschwieler, J. D. Atomic-scale imaging of DNA using scanning tunnelling microscopy. *Nature* **346**, 294–296 (1990).

[15] Abb, S., Harnau, L., Gutzler, R., Rauschenbach, S. & Kern, K. Two-dimensional honeycomb network through sequence-controlled self-assembly of oligopeptides. *Nat. Commun.* **7**, 10335 (2016).

[16] Terada, Y., Yoshida, S., Takeuchi, O. & Shigekawa, H. Real-space imaging of transient carrier dynamics by nanoscale pump–probe microscopy. *Nat. Photon.* **4**, 869–874 (2010).

[17] Loth, S., Etzkorn, M., Lutz, C. P., Eigler, D. M. & Heinrich, A. J. Measurement of Fast Electron Spin Relaxation Times with Atomic Resolution. *Science* **329**, 1628–1630 (2010).

[18] Cocker, T. L. *et al.* An ultrafast terahertz scanning tunnelling microscope. *Nat. Photon.* **7**, 620–625 (2013).

[19] Merino, P., Große, C., Rosławska, A., Kuhnke, K. & Kern, K. Exciton dynamics of C60-based single-photon emitters explored by Hanbury Brown-Twiss scanning tunnelling microscopy. *Nat. Commun.* **6**, 8461 (2015).

[20] Li, S., Chen, S., Li, J., Wu, R. & Ho, W. Joint Space-Time Coherent Vibration Driven Conformational Transitions in a Single Molecule. *Phys. Rev. Lett.* **119**, 176002 (2017).

[21] Qiu, X. H., Nazin, G. V. & Ho, W. Vibrationally Resolved Fluorescence Excited with Submolecular Precision. *Science* **299**, 542–546 (2003).

[22] Kuhnke, K., Große, C., Merino, P. & Kern, K. Atomic-Scale Imaging and Spectroscopy of Electroluminescence at Molecular Interfaces. *Chem. Rev.* **117**, 5174–5222 (2017).

[23] Leon, C. *et al.* Photon super-bunching from a generic tunnel junction. *arXiv:1805.10234 [cond-mat]* (2018).

[24] Barth, J. V. Transport of adsorbates at metal surfaces: From thermal migration to hot precursors. *Surface Science Reports* **40**, 75–149 (2000).

[25] Benz, F. *et al.* Single-molecule optomechanics in "picocavities". *Science* **354**, 726–729 (2016).

[26] Ostroverkhova, O. Organic Optoelectronic Materials: Mechanisms and Applications. *Chem. Rev.* **116**, 13279–13412 (2016).

[27] Novotny, L. & Hecht, B. *Principles of Nano-Optics* (Cambridge University Press, 2012).

[28] Young, R., Ward, J. & Scire, F. The Topografiner: An Instrument for Measuring Surface Microtopography. *Review of Scientific Instruments* **43**, 999–1011 (1972).

[29] Binnig, G., Rohrer, H., Gerber, C. & Weibel, E. Surface Studies by Scanning Tunneling Microscopy. *Phys. Rev. Lett.* **49**, 57–61 (1982).

[30] Binnig, G., Rohrer, H., Gerber, C. & Weibel, E. 7 x 7 Reconstruction on Si(111) Resolved in Real Space. *Phys. Rev. Lett.* **50**, 120–123 (1983).

[31] Gross, L., Mohn, F., Moll, N., Liljeroth, P. & Meyer, G. The Chemical Structure of a Molecule Resolved by Atomic Force Microscopy. *Science* **325**, 1110–1114 (2009).

[32] Morita, S., Giessibl, F. J., Meyer, E. & Wiesendanger, R. *Noncontact Atomic Force Microscopy* (Springer, 2015).

[33] Eigler, D. M. & Schweizer, E. K. Positioning single atoms with a scanning tunnelling microscope. *Nature* **344**, 524–526 (1990).

[34] Crommie, M. F., Lutz, C. P. & Eigler, D. M. Confinement of Electrons to Quantum Corrals on a Metal Surface. *Science* **262**, 218–220 (1993).

[35] Wiesendanger, R., Güntherodt, H.-J., Güntherodt, G., Gambino, R. J. & Ruf, R. Observation of vacuum tunneling of spin-polarized electrons with the scanning tunneling microscope. *Phys. Rev. Lett.* **65**, 247–250 (1990).

[36] Heinrich, A. J., Gupta, J. A., Lutz, C. P. & Eigler, D. M. Single-Atom Spin-Flip Spectroscopy. *Science* **306**, 466–469 (2004).

[37] Loth, S., Baumann, S., Lutz, C. P., Eigler, D. M. & Heinrich, A. J. Bistability in Atomic-Scale Antiferromagnets. *Science* **335**, 196–199 (2012).

[38] Romming, N. *et al.* Writing and Deleting Single Magnetic Skyrmions. *Science* **341**, 636–639 (2013).

[39] Hla, S.-W., Bartels, L., Meyer, G. & Rieder, K.-H. Inducing All Steps of a Chemical Reaction with the Scanning Tunneling Microscope Tip: Towards Single Molecule Engineering. *Phys. Rev. Lett.* **85**, 2777–2780 (2000).

[40] de Oteyza, D. G. *et al.* Direct Imaging of Covalent Bond Structure in Single-Molecule Chemical Reactions. *Science* 1238187 (2013).

[41] Borca, B. *et al.* Electric-Field-Driven Direct Desulfurization. *ACS Nano* **11**, 4703–4709 (2017).

[42] Somorjai, G. A. The surface science of heterogeneous catalysis. *Surf. Sci.* **299-300**, 849–866 (1994).

[43] Bowker, M. Catalysis resolved using scanning tunnelling microscopy. *Chem. Soc. Rev.* **36**, 1656–1673 (2007).

[44] Overney, R. M. *et al.* Friction measurements on phase-separated thin films with a modified atomic force microscope. *Nature* **359**, 133–135 (1992).

[45] Socoliuc, A. *et al.* Atomic-Scale Control of Friction by Actuation of Nanometer-Sized Contacts. *Science* **313**, 207–210 (2006).

[46] Chen, C. J. *Introduction to Scanning Tunneling Microscopy: Second Edition* (Oxford University Press, 2007).

[47] Voigtländer, B. Lock-In Technique. In Voigtländer, B. (ed.) *Scanning Probe Microscopy: Atomic Force Microscopy and Scanning Tunneling Microscopy*, NanoScience and Technology, 101–105 (Springer Berlin Heidelberg, Berlin, Heidelberg, 2015).

[48] Balantekin, A. B. & Takigawa, N. Quantum tunneling in nuclear fusion. *Rev. Mod. Phys.* **70**, 77–100 (1998).

[49] Löwdin, P.-O. Proton Tunneling in DNA and its Biological Implications. *Rev. Mod. Phys.* **35**, 724–732 (1963).

[50] Muller, D. A. *et al.* The electronic structure at the atomic scale of ultrathin gate oxides. *Nature* **399**, 758–761 (1999).

[51] Bardeen, J. Tunnelling from a Many-Particle Point of View. *Phys. Rev. Lett.* **6**, 57–59 (1961).

[52] Voigtlaender, B. *Scanning Probe Microscopy: Atomic Force Microscopy and Scanning Tunneling Microscopy*. NanoScience and Technology (Springer-Verlag, Berlin Heidelberg, 2015).

[53] Tersoff, J. & Hamann, D. R. Theory of the scanning tunneling microscope. *Phys. Rev. B* **31**, 805–813 (1985).

[54] Young, R. D. Surface microtopography. *Physics Today* **24**, 42 (1971).

[55] Lambe, J. & McCarthy, S. L. Light Emission from Inelastic Electron Tunneling. *Phys. Rev. Lett.* **37**, 923–925 (1976).

[56] Gimzewski, J. K., Reihl, B., Coombs, J. H. & Schlittler, R. R. Photon emission with the scanning tunneling microscope. *Z. Physik B - Condensed Matter* **72**, 497–501 (1988).

[57] Berndt, R., Gimzewski, J. K. & Johansson, P. Inelastic tunneling excitation of tip-induced plasmon modes on noble-metal surfaces. *Phys. Rev. Lett.* **67**, 3796–3799 (1991).

[58] Berndt, R. & Gimzewski, J. K. Injection luminescence from CdS(112¯0) studied with scanning tunneling microscopy. *Phys. Rev. B* **45**, 14095–14099 (1992).

[59] Berndt, R. *et al.* Photon Emission at Molecular Resolution Induced by a Scanning Tunneling Microscope. *Science* **262**, 1425–1427 (1993).

[60] Zhang, L. *et al.* Electrically driven single-photon emission from an isolated single molecule. *Nat. Commun.* **8**, 580 (2017).

[61] Zhang, Y. *et al.* Visualizing coherent intermolecular dipole–dipole coupling in real space. *Nature* **531**, 623–627 (2016).

[62] Imada, H. *et al.* Real-space investigation of energy transfer in heterogeneous molecular dimers. *Nature* **538**, 364–367 (2016).

[63] Doppagne, B. *et al.* Electrofluorochromism at the single-molecule level. *Science* **361**, 251–255 (2018).

[64] Gustafsson, A., Pistol, M.-E., Montelius, L. & Samuelson, L. Local probe techniques for luminescence studies of low-dimensional semiconductor structures. *J. Appl. Phys.* **84**, 1715–1775 (1998).

[65] Watanabe, A., Ito, O., Watanabe, M., Saito, H. & Koishi, M. Picosecond time-resolved near-IR spectra of C60 excited states by pump-probe measurements using a probe beam based on broad-band optical parametric generation. *Chem. Commun.* 117–118 (1996).

[66] Rossel, F., Pivetta, M. & Schneider, W.-D. Luminescence experiments on supported molecules with the scanning tunneling microscope. *Surf. Sci. Rep.* **65**, 129–144 (2010).

[67] Barnes, W. L., Dereux, A. & Ebbesen, T. W. Surface plasmon subwavelength optics. *Nature* **424**, 824–830 (2003).

[68] Rendell, R. W., Scalapino, D. J. & Mühlschlegel, B. Role of Local Plasmon Modes in Light Emission from Small-particle Tunnel Junctions. *Phys. Rev. Lett.* **41**, 1746–1750 (1978).

[69] Rendell, R. W. & Scalapino, D. J. Surface plasmons confined by microstructures on tunnel junctions. *Phys. Rev. B* **24**, 3276–3294 (1981).

[70] Zhang, R. *et al.* Chemical mapping of a single molecule by plasmon-enhanced Raman scattering. *Nature* **498**, 82–86 (2013).

[71] Zrimsek, A. B. *et al.* Single-Molecule Chemistry with Surface- and Tip-Enhanced Raman Spectroscopy. *Chem. Rev.* **117**, 7583–7613 (2017).

[72] Aizpurua, J., Hoffmann, G., Apell, S. P. & Berndt, R. Electromagnetic Coupling on an Atomic Scale. *Phys. Rev. Lett.* **89**, 156803 (2002).

[73] Berndt, R. *et al.* Atomic Resolution in Photon Emission Induced by a Scanning Tunneling Microscope. *Phys. Rev. Lett.* **74**, 102–105 (1995).

[74] Schull, G., Becker, M. & Berndt, R. Imaging Confined Electrons with Plasmonic Light. *Phys. Rev. Lett.* **101** (2008).

[75] Reinhardt, M., Schull, G., Ebert, P. & Berndt, R. Atomic resolution in tunneling induced light emission from GaAs(110). *Appl. Phys. Lett.* **96**, 152107 (2010).

[76] Große, C. *et al.* Submolecular Electroluminescence Mapping of Organic Semiconductors. *ACS Nano* **11**, 1230–1237 (2017).

[77] Blaber, M. G., Arnold, M. D. & Ford, M. J. A review of the optical properties of alloys and intermetallics for plasmonics. *J. Phys.: Condens. Matter* **22**, 143201 (2010).

[78] Wang, H., Tam, F., Grady, N. K. & Halas, N. J. Cu Nanoshells: Effects of Interband Transitions on the Nanoparticle Plasmon Resonance. *J. Phys. Chem. B* **109**, 18218–18222 (2005).

[79] Stipe, B. C., Rezaei, M. A. & Ho, W. Single-Molecule Vibrational Spectroscopy and Microscopy. *Science* **280**, 1732–1735 (1998).

[80] Jacobson, P. *et al.* Potential energy–driven spin manipulation via a controllable hydrogen ligand. *Sci. Adv.* **3**, e1602060 (2017).

[81] Parzefall, M. & Novotny, L. Light at the End of the Tunnel. *ACS Photonics* **5**, 4195–4202 (2018).

[82] Persson, B. N. J. & Baratoff, A. Theory of photon emission in electron tunneling to metallic particles. *Phys. Rev. Lett.* **68**, 3224–3227 (1992).

[83] Laks, B. & Mills, D. L. Photon emission from slightly roughened tunnel junctions. *Phys. Rev. B* **20**, 4962–4980 (1979).

[84] Johansson, P., Monreal, R. & Apell, P. Theory for light emission from a scanning tunneling microscope. *Phys. Rev. B* **42**, 9210–9213 (1990).

[85] Lü, J.-T., Christensen, R. B. & Brandbyge, M. Light emission and finite-frequency shot noise in molecular junctions: From tunneling to contact. *Phys. Rev. B* **88** (2013).

[86] Nilius, N., Ernst, N. & Freund, H.-J. Photon Emission Spectroscopy of Individual Oxide-Supported Silver Clusters in a Scanning Tunneling Microscope. *Phys. Rev. Lett.* **84**, 3994–3997 (2000).

[87] Dong, Z.-C. *et al.* Vibrationally Resolved Fluorescence from Organic Molecules near Metal Surfaces in a Scanning Tunneling Microscope. *Phys. Rev. Lett.* **92** (2004).

[88] Zhang, Y. *et al.* Modulation of local plasmon mediated emission through molecular manipulation. *Phys. Rev. B* **79**, 075406 (2009).

[89] Krukowski, P. *et al.* Detection of Light Emission from (S)-PTCDI Molecules Adsorbed on Au(111) and NiAl(110) Surfaces Induced by a Scanning Tunneling Microscope. *J. Phys. Chem. C* **120**, 3964–3977 (2016).

[90] Tao, X. *et al.* Influence of a dielectric layer on photon emission induced by a scanning tunneling microscope. *J. Chem. Phys.* **130**, 084706 (2009).

[91] Steinmüller-Nethl, D., Höpfel, R. A., Gornik, E., Leitner, A. & Aussenegg, F. R. Femtosecond relaxation of localized plasma excitations in Ag islands. *Phys. Rev. Lett.* **68**, 389–392 (1992).

[92] Hecht, B., Bielefeldt, H., Novotny, L., Inouye, Y. & Pohl, D. W. Local Excitation, Scattering, and Interference of Surface Plasmons. *Phys. Rev. Lett.* **77**, 1889–1892 (1996).

[93] Grosse, C., Etzkorn, M., Kuhnke, K., Loth, S. & Kern, K. Quantitative mapping of fast voltage pulses in tunnel junctions by plasmonic luminescence. *Appl. Phys. Lett.* **103**, 183108 (2013).

[94] Avouris, P. & Persson, B. N. J. Excited states at metal surfaces and their non-radiative relaxation. *J. Phys. Chem.* **88**, 837–848 (1984).

[95] Andrews, D. L. A unified theory of radiative and radiationless molecular energy transfer. *Chem. Phys.* **135**, 195–201 (1989).

[96] Kuhnke, K., Becker, R., Epple, M. & Kern, K. C_{60} Exciton Quenching near Metal Surfaces. *Phys. Rev. Lett.* **79**, 3246–3249 (1997).

[97] Doppagne, B. *et al.* Vibronic Spectroscopy with Submolecular Resolution from STM-Induced Electroluminescence. *Phys. Rev. Lett.* **118**, 127401 (2017).

[98] Dong, Z. C. *et al.* Generation of molecular hot electroluminescence by resonant nanocavity plasmons. *Nat. Photon.* **4**, 50–54 (2009).

[99] Ćavar, E. *et al.* Fluorescence and Phosphorescence from Individual C 60 Molecules Excited by Local Electron Tunneling. *Phys. Rev. Lett.* **95** (2005).

[100] Kabakchiev, A., Kuhnke, K., Lutz, T. & Kern, K. Electroluminescence from Individual Pentacene Nanocrystals. *ChemPhysChem* **11**, 3412–3416 (2010).

[101] Kuhnke, K. *et al.* Pentacene Excitons in Strong Electric Fields. *ChemPhysChem* **19**, 277–283 (2017).

[102] Reecht, G. *et al.* Electroluminescence of a Polythiophene Molecular Wire Suspended between a Metallic Surface and the Tip of a Scanning Tunneling Microscope. *Phys. Rev. Lett.* **112** (2014).

[103] Chong, M. C. *et al.* Narrow-Line Single-Molecule Transducer between Electronic Circuits and Surface Plasmons. *Phys. Rev. Lett.* **116**, 036802 (2016).

[104] Chong, M. C. *et al.* Ordinary and Hot Electroluminescence from Single-Molecule Devices: Controlling the Emission Color by Chemical Engineering. *Nano Lett.* **16**, 6480–6484 (2016).

[105] Chong, M. C. *et al.* Bright Electroluminescence from Single Graphene Nanoribbon Junctions. *Nano Lett.* **18**, 175–181 (2018).

[106] Große, C., Gunnarsson, O., Merino, P., Kuhnke, K. & Kern, K. Nanoscale Imaging of Charge Carrier and Exciton Trapping at Structural Defects in Organic Semiconductors. *Nano Letters* **16**, 2084–2089 (2016).

[107] Rosławska, A. *et al.* Single Charge and Exciton Dynamics Probed by Molecular-Scale-Induced Electroluminescence. *Nano Lett.* **18**, 4001–4007 (2018).

[108] Merino, P. *et al.* Bimodal exciton-plasmon light sources controlled by local charge carrier injection. *Sci. Adv.* **4**, eaap8349 (2018).

[109] Imada, H. *et al.* Single-Molecule Investigation of Energy Dynamics in a Coupled Plasmon-Exciton System. *Phys. Rev. Lett.* **119**, 013901 (2017).

[110] Zhang, Y. *et al.* Sub-nanometre control of the coherent interaction between a single molecule and a plasmonic nanocavity. *Nat. Commun.* **8**, 15225 (2017).

[111] Kröger, J., Doppagne, B., Scheurer, F. & Schull, G. Fano Description of Single-Hydrocarbon Fluorescence Excited by a Scanning Tunneling Microscope. *Nano Lett.* **18**, 3407–3413 (2018).

[112] Lutz, T. *et al.* Molecular Orbital Gates for Plasmon Excitation. *Nano Lett.* **13**, 2846–2850 (2013).

[113] Rost, M. J. *et al.* Scanning probe microscopes go video rate and beyond. *Rev. Sci. Instrum.* **76**, 053710 (2005).

[114] Schitter, G. & Rost, M. J. Scanning probe microscopy at video-rate. *Materials Today* **11**, 40–48 (2008).

[115] van Houselt, A. & Zandvliet, H. J. W. Colloquium : Time-resolved scanning tunneling microscopy. *Rev. Mod. Phys.* **82**, 1593–1605 (2010).

[116] Patera, L. L. *et al.* Real-time imaging of adatom-promoted graphene growth on nickel. *Science* **359**, 1243–1246 (2018).

[117] Nunes, G. & Freeman, M. R. Picosecond Resolution in Scanning Tunneling Microscopy. *Science* **262**, 1029–1032 (1993).

[118] Durkan, C. & Welland, M. E. Electronic spin detection in molecules using scanning-tunneling- microscopy-assisted electron-spin resonance. *Appl. Phys. Lett.* **80**, 458–460 (2002).

[119] Takeuchi, O., Yoshida, S. & Shigekawa, H. Light-modulated scanning tunneling spectroscopy for nanoscale imaging of surface photovoltage. *Appl. Phys. Lett.* **84**, 3645–3647 (2004).

[120] Shigekawa, H., Takeuchi, O. & Aoyama, M. Development of femtosecond time-resolved scanning tunneling microscopy for nanoscale science and technology. *Sci. Technol. Adv. Mater.* **6**, 582 (2005).

[121] Yan, S., Choi, D.-J., Burgess, J. A. J., Rolf-Pissarczyk, S. & Loth, S. Control of quantum magnets by atomic exchange bias. *Nat. Nanotechnol.* **10**, 40–45 (2015).

[122] Baumann, S. *et al.* Electron paramagnetic resonance of individual atoms on a surface. *Science* **350**, 417–420 (2015).

[123] Yan, S. *et al.* Nonlocally sensing the magnetic states of nanoscale antiferromagnets with an atomic spin sensor. *Sci. Adv.* **3**, e1603137 (2017).

[124] Paul, W. *et al.* Control of the millisecond spin lifetime of an electrically probed atom. *Nat. Phys.* **13**, 403–407 (2017).

[125] Rashidi, M. *et al.* Time-resolved single dopant charge dynamics in silicon. *Nat. Commun.* **7**, 13258 (2016).

[126] Rashidi, M. *et al.* Time-Resolved Imaging of Negative Differential Resistance on the Atomic Scale. *Phys. Rev. Lett.* **117**, 276805 (2016).

[127] Rashidi, M. *et al.* Resolving and Tuning Carrier Capture Rates at a Single Silicon Atom Gap State. *ACS Nano* **11**, 11732–11738 (2017).

[128] Yoshida, S. *et al.* Single-Atomic-Level Probe of Transient Carrier Dynamics by Laser-Combined Scanning Tunneling Microscopy. *Appl. Phys. Express* **6**, 032401 (2013).

[129] Yoshida, S. *et al.* Probing ultrafast spin dynamics with optical pump-probe scanning tunnelling microscopy. *Nat. Nanotechnol.* **9**, 588–593 (2014).

[130] Kloth, P. & Wenderoth, M. From time-resolved atomic-scale imaging of individual donors to their cooperative dynamics. *Sci. Adv.* **3** (2017).

[131] Jelic, V. *et al.* Ultrafast terahertz control of extreme tunnel currents through single atoms on a silicon surface. *Nat. Phys.* **13**, 591–598 (2017).

[132] Yoshioka, K. *et al.* Real-space coherent manipulation of electrons in a single tunnel junction by single-cycle terahertz electric fields. *Nat. Photon.* **10**, 762–765 (2016).

[133] Cocker, T. L., Peller, D., Yu, P., Repp, J. & Huber, R. Tracking the ultrafast motion of a single molecule by femtosecond orbital imaging. *Nature* **539**, 263–267 (2016).

[134] Silly, F. & Charra, F. Time-autocorrelation in scanning-tunneling-microscope-induced photon emission from metallic surface. *Appl. Phys. Lett.* **77**, 3648–3650 (2000).

[135] Silly, F. & Charra, F. Time-correlations as a contrast mechanism in scanning-tunneling-microscopy-induced photon emission. *Ultramicroscopy* **99**, 159–164 (2004).

[136] Perronet, K., Schull, G., Raimond, P. & Charra, F. Single-molecule fluctuations in a tunnel junction: A study by scanning-tunnelling-microscopy–induced luminescence. *EPL* **74**, 313 (2006).

[137] Pan, S. H., Hudson, E. W. & Davis, J. C. 3He refrigerator based very low temperature scanning tunneling microscope. *Rev. Sci. Instrum.* **70**, 1459–1463 (1999).

[138] Horcas, I. *et al.* WSXM: A software for scanning probe microscopy and a tool for nanotechnology. *Rev. Sci. Instrum.* **78**, 013705 (2007).

[139] Kuhnke, K. *et al.* Versatile optical access to the tunnel gap in a low-temperature scanning tunneling microscope. *Rev. Sci. Instrum.* **81**, 113102 (2010).

[140] Kabakchiev, A. *Scanning Tunneling Luminescence of Pentacene Nanocrystals.* Ph.D. thesis, EPFL (2010).

[141] Hervé, M., Peter, M. & Wulfhekel, W. High frequency transmission to a junction of a scanning tunneling microscope. *Appl. Phys. Lett.* **107**, 093101 (2015).

[142] Paul, W., Baumann, S., Lutz, C. P. & Heinrich, A. J. Generation of constant-amplitude radio-frequency sweeps at a tunnel junction for spin resonance STM. *Rev. Sci. Instrum.* **87**, 074703 (2016).

[143] Saunus, C., Bindel, J. R., Pratzer, M. & Morgenstern, M. Versatile scanning tunneling microscopy with 120 ps time resolution. *Appl. Phys. Lett.* **102**, 051601 (2013).

[144] Ren, B., Picardi, G. & Pettinger, B. Preparation of gold tips suitable for tip-enhanced Raman spectroscopy and light emission by electrochemical etching. *Rev. Sci. Instrum.* **75**, 837–841 (2004).

[145] Martínez-Blanco, J. & Fölsch, S. Light emission from Ag(111) driven by inelastic tunneling in the field emission regime. *J. Phys.: Condens. Matter* **27**, 255008 (2015).

[146] Fox, M. *Quantum Optics: An Introduction* (OUP Oxford, 2006).

[147] Loudon, R. *The Quantum Theory of Light* (OUP Oxford, 2000).

[148] Brown, R. H. & Twiss, R. Q. Correlation between Photons in two Coherent Beams of Light. *Nature* **177**, 27–29 (1956).

[149] Hanbury Brown, R. & Twiss, R. Q. A Test of a New Type of Stellar Interferometer on Sirius. *Nature* **178**, 1046–1048 (1956).

[150] Michler, P. *et al.* A Quantum Dot Single-Photon Turnstile Device. *Science* **290**, 2282–2285 (2000).

[151] Meuret, S. *et al.* Photon Bunching in Cathodoluminescence. *Phys. Rev. Lett.* **114**, 197401 (2015).

[152] Kurtsiefer, C., Mayer, S., Zarda, P. & Weinfurter, H. Stable Solid-State Source of Single Photons. *Phys. Rev. Lett.* **85**, 290–293 (2000).

[153] Berthel, M. *et al.* Photophysics of single nitrogen-vacancy centers in diamond nanocrystals. *Phys. Rev. B* **91**, 035308 (2015).

[154] Khramtsov, I. A., Agio, M. & Fedyanin, D. Y. Dynamics of Single-Photon Emission from Electrically Pumped Color Centers. *Phys. Rev. Appl.* **8**, 024031 (2017).

[155] Neu, E., Agio, M. & Becher, C. Photophysics of single silicon vacancy centers in diamond: Implications for single photon emission. *Opt. Express* **20**, 19956–19971 (2012).

[156] Michler, P. *et al.* Quantum correlation among photons from a single quantum dot at room temperature. *Nature* **406**, 968–970 (2000).

[157] Lohrmann, A. *et al.* Single-photon emitting diode in silicon carbide. *Nature Communications* **6**, 7783 (2015).

[158] Neuman, T., Esteban, R., Casanova, D., García-Vidal, F. J. & Aizpurua, J. Coupling of Molecular Emitters and Plasmonic Cavities beyond the Point-Dipole Approximation. *Nano Lett.* **18**, 2358–2364 (2018).

[159] Marks, R. W. & Fuller, R. B. *The Dymaxion World of Buckminster Fuller* (Reinhold Pub. Corp., New York, 1960).

[160] Kroto, H. W., Heath, J. R., O'Brien, S. C., Curl, R. F. & Smalley, R. E. C_{60}: Buckminsterfullerene. *Nature* **318**, 162–163 (1985).

[161] Dresselhaus, M., Dresselhaus, G. & Eklund, P. C. *Science of Fullerenes and Carbon Nanotubes* (Academic Press, 1996).

[162] Allemand, P.-M. *et al.* Organic Molecular Soft Ferromagnetism in a Fullerene C_{60}. *Science* **253**, 301–302 (1991).

[163] Hebard, A. F. *et al.* Superconductivity at 18 K in potassium-doped C_{60}. *Nature* **350**, 600–601 (1991).

[164] Rosseinsky, M. J. *et al.* Superconductivity at 28 K in Rb_xC_{60}. *Phys. Rev. Lett.* **66**, 2830–2832 (1991).

[165] Tanigaki, K. *et al.* Superconductivity at 33 K in $Cs_xRb_yC_{60}$. *Nature* **352**, 222–223 (1991).

[166] Mitrano, M. *et al.* Possible light-induced superconductivity in K_3C_{60} at high temperature. *Nature* **530**, 461–464 (2016).

[167] Günes, S., Neugebauer, H. & Sariciftci, N. S. Conjugated Polymer-Based Organic Solar Cells. *Chem. Rev.* **107**, 1324–1338 (2007).

[168] Thompson, B. C. & Fréchet, J. M. J. Polymer–Fullerene Composite Solar Cells. *Angew. Chem.* **47**, 58–77 (2008).

[169] Shirota, Y. & Kageyama, H. Charge Carrier Transporting Molecular Materials and Their Applications in Devices. *Chem. Rev.* **107**, 953–1010 (2007).

[170] Wilson, R. J. *et al.* Imaging C60 clusters on a surface using a scanning tunnelling microscope. *Nature* **348**, 621–622 (1990).

[171] Hashizume, T. & Sakurai, T. C_{60} adsorption on the Si(100)2×1 and Cu(111)1×1 surfaces. *Journal of Vacuum Science & Technology B: Microelectronics and Nanometer Structures Processing, Measurement, and Phenomena* **12**, 1992–1999 (1994).

[172] Hashizume, T. *et al.* Intramolecular structures of C_{60} molecules adsorbed on the Cu(111)-(1x1) surface. *Phys. Rev. Lett.* **71**, 2959–2962 (1993).

[173] Cuberes, M., Schlittler, R. & Gimzewski, J. Manipulation of C_{60} molecules on Cu(111) surfaces using a scanning tunneling microscope. *Appl Phys A* **66**, S669–S673 (1998).

[174] Schull, G., Frederiksen, T., Brandbyge, M. & Berndt, R. Passing Current through Touching Molecules. *Phys. Rev. Lett.* **103**, 206803 (2009).

[175] Schull, G., Frederiksen, T., Arnau, A., Sánchez-Portal, D. & Berndt, R. Atomic-scale engineering of electrodes for single-molecule contacts. *Nat. Nanotechnol.* **6**, 23–27 (2011).

[176] Weckesser, J., Barth, J. V. & Kern, K. Mobility and bonding transition of C_{60} on Pd(110). *Phys. Rev. B* **64**, 161403 (2001).

[177] Weckesser, J. *et al.* Binding and ordering of C_{60} on Pd(110): Investigations at the local and mesoscopic scale. *J. Chem. Phys.* **115**, 9001–9009 (2001).

[178] Altman, E. I. & Colton, R. J. Determination of the orientation of C_{60} adsorbed on Au(111) and Ag(111). *Phys. Rev. B* **48**, 18244–18249 (1993).

[179] Altman, E. I. & Colton, R. J. The interaction of C_{60} with noble metal surfaces. *Surf. Sci.* **295**, 13–33 (1993).

[180] Howells, S. *et al.* High resolution images of single C_{60} molecules on gold (111) using scanning tunneling microscopy. *Surf. Sci.* **274**, 141–146 (1992).

[181] Gimzewski, J. K., Modesti, S., Gerber, C. & Schlittler, R. R. Observation of a new Au (111) reconstruction at the interface of an adsorbed C_{60} overlayer. *Chem. Phys. Lett.* **213**, 401–406 (1993).

[182] Rogero, C., Pascual, J. I., Gómez-Herrero, J. & Baró, A. M. Resolution of site-specific bonding properties of C_{60} adsorbed on Au(111). *J. Chem. Phys.* **116**, 832–836 (2001).

[183] Schull, G. & Berndt, R. Orientationally Ordered (7×7) Superstructure of C_{60} on Au(111). *Phys. Rev. Lett.* **99** (2007).

[184] Schull, G., Néel, N., Becker, M., Kröger, J. & Berndt, R. Spatially resolved conductance of oriented C_{60}. *New J. Phys.* **10**, 065012 (2008).

[185] Torrente, I. F., Franke, K. J. & Pascual, J. I. Spectroscopy of C 60 single molecules: The role of screening on energy level alignment. *J. Phys.: Condens. Matter* **20**, 184001 (2008).

[186] David, W. I. F., Ibberson, R. M., Dennis, T. J. S., Hare, J. P. & Prassides, K. Structural Phase Transitions in the Fullerene C 60. *EPL* **18**, 219 (1992).

[187] Wang, H. *et al.* Orientational configurations of the C_{60} molecules in the (2x2) superlattice on a solid C_{60} (111) surface at low temperature. *Phys. Rev. B* **63**, 085417 (2001).

[188] Rossel, F. *et al.* Growth and characterization of fullerene nanocrystals on NaCl/Au(111). *Phys. Rev. B* **84**, 075426 (2011).

[189] Blase, X., Attaccalite, C. & Olevano, V. First-principles GW calculations for fullerenes, porphyrins, phtalocyanine, and other molecules of interest for organic photovoltaic applications. *Phys. Rev. B* **83**, 115103 (2011).

[190] Ohno, T. R. *et al.* C_{60} bonding and energy-level alignment on metal and semiconductor surfaces. *Phys. Rev. B* **44**, 13747–13755 (1991).

[191] Tzeng, C.-T., Lo, W.-S., Yuh, J.-Y., Chu, R.-Y. & Tsuei, K.-D. Photoemission, near-edge x-ray-absorption spectroscopy, and low-energy electron-diffraction study of C_{60} on Au(111) surfaces. *Phys. Rev. B* **61**, 2263–2272 (2000).

[192] Schulze, G. *et al.* Resonant Electron Heating and Molecular Phonon Cooling in Single C_{60} Junctions. *Phys. Rev. Lett.* **100**, 136801 (2008).

[193] Grosse, C. *Monitoring Charge Carrier Dynamics at Atomic Length Scales by STM-Induced Luminescence.* Ph.D. thesis, EPFL (2015).

[194] Catalan, J. & Elguero, J. Fluorescence of fullerenes (C60 and C70). *J. Am. Chem. Soc.* **115**, 9249–9252 (1993).

[195] Laporte, O. & Meggers, W. F. Some Rules of Spectral Structure*. *J. Opt. Soc. Am., JOSA* **11**, 459–463 (1925).

[196] Akimoto, I. & Kan'no, K.-i. Photoluminescence and Near-Edge Optical Absorption in the Low-Temperature Phase of Pristine C60 Single Crystals. *J. Phys. Soc. Jpn.* **71**, 630–643 (2002).

[197] Jahn, H. A. & Teller, E. Stability of polyatomic molecules in degenerate electronic states - I—Orbital degeneracy. *Proc. R. Soc. Lond. A* **161**, 220–235 (1937).

[198] Akimoto, I. & Kan'no, K. Origin of photoluminescence and spectral analysis of vibronic structure resolved in C_{60} single crystals. *J. Lumin.* **87-89**, 788–790 (2000).

[199] Berndt, R. *et al.* Photon emission from adsorbed C_{60} molecules with sub-nanometer lateral resolution. *Appl. Phys. A* **57**, 513–516 (1993).

[200] Sakamoto, K. *et al.* Light emission spectra of the monolayer-island of C_{60} molecules on Au(111) induced by scanning tunneling microscope. *Surf. Sci.* **502–503**, 149–155 (2002).

[201] Rossel, F., Pivetta, M., Patthey, F. & Schneider, W.-D. Plasmon enhanced luminescence from fullerene molecules excited by local electron tunneling. *Opt. Express* **17**, 2714–2721 (2009).

[202] Geng, F. *et al.* Modulation of nanocavity plasmonic emission by local molecular states of C_{60} on Au(111). *Opt. Express, OE* **20**, 26725–26735 (2012).

[203] Schulze, G., Franke, K. J. & Pascual, J. I. Resonant heating and substrate-mediated cooling of a single C_{60} molecule in a tunnel junction. *New J. Phys.* **10**, 065005 (2008).

[204] Kuehne, A. J. C. & Gather, M. C. Organic Lasers: Recent Developments on Materials, Device Geometries, and Fabrication Techniques. *Chem. Rev.* **116**, 12823–12864 (2016).

[205] Hosokawa, C., Tokailin, H., Higashi, H. & Kusumoto, T. Transient behavior of organic thin film electroluminescence. *Appl. Phys. Lett.* **60**, 1220–1222 (1992).

[206] Brütting, W., Berleb, S. & Mückl, A. G. Device physics of organic light-emitting diodes based on molecular materials. *Organic Electronics* **2**, 1–36 (2001).

[207] Kasemann, D., Brückner, R., Fröb, H. & Leo, K. Organic light-emitting diodes under high currents explored by transient electroluminescence on the nanosecond scale. *Phys. Rev. B* **84** (2011).

[208] Nakanotani, H. *et al.* High-efficiency organic light-emitting diodes with fluorescent emitters. *Nat. Commun.* **5**, 4016 (2014).

[209] Lüssem, B. *et al.* Doped Organic Transistors. *Chem. Rev.* **116**, 13714–13751 (2016).

[210] Veenstra, S., Heeres, A., Hadziioannou, G., Sawatzky, G. & Jonkman, H. On interface dipole layers between C_{60} and Ag or Au. *Appl. Phys. A* **75**, 661–666 (2002).

[211] Repp, J., Meyer, G., Olsson, F. E. & Persson, M. Controlling the Charge State of Individual Gold Adatoms. *Science* **305**, 493–495 (2004).

[212] Olsson, F. E., Paavilainen, S., Persson, M., Repp, J. & Meyer, G. Multiple Charge States of Ag Atoms on Ultrathin NaCl Films. *Phys. Rev. Lett.* **98**, 176803 (2007).

[213] Sterrer, M. *et al.* Control of the Charge State of Metal Atoms on Thin MgO Films. *Phys. Rev. Lett.* **98**, 096107 (2007).

[214] Nazin, G. V., Wu, S. W. & Ho, W. Tunneling rates in electron transport through double-barrier molecular junctions in a scanning tunneling microscope. *PNAS* **102**, 8832–8837 (2005).

[215] Wu, S. W., Ogawa, N. & Ho, W. Atomic-Scale Coupling of Photons to Single-Molecule Junctions. *Science* **312**, 1362–1365 (2006).

[216] Große, C. *et al.* Dynamic Control of Plasmon Generation by an Individual Quantum System. *Nano Lett.* **14**, 5693–5697 (2014).

[217] Fatayer, S. *et al.* Reorganization energy upon charging a single molecule on an insulator measured by atomic force microscopy. *Nat. Nanotechnol.* **13**, 376–380 (2018).

[218] Berthe, M. *et al.* Probing the Carrier Capture Rate of a Single Quantum Level. *Science* **319**, 436–438 (2008).

[219] Teichmann, K. *et al.* Controlled Charge Switching on a Single Donor with a Scanning Tunneling Microscope. *Phys. Rev. Lett.* **101** (2008).

[220] Lee, D. H. & Gupta, J. A. Tunable Field Control Over the Binding Energy of Single Dopants by a Charged Vacancy in GaAs. *Science* **330**, 1807–1810 (2010).

[221] Zheng, H., Kröger, J. & Berndt, R. Spectroscopy of Single Donors at ZnO(0001) Surfaces. *Phys. Rev. Lett.* **108**, 076801 (2012).

[222] Wong, D. *et al.* Characterization and manipulation of individual defects in insulating hexagonal boron nitride using scanning tunnelling microscopy. *Nat. Nanotechnol.* **10**, 949–953 (2015).

[223] Kocić, N. *et al.* Periodic Charging of Individual Molecules Coupled to the Motion of an Atomic Force Microscopy Tip. *Nano Lett.* **15**, 4406–4411 (2015).

[224] Najafi, E., Scarborough, T. D., Tang, J. & Zewail, A. Four-dimensional imaging of carrier interface dynamics in p-n junctions. *Science* **347**, 164–167 (2015).

[225] Du, W. *et al.* On-chip molecular electronic plasmon sources based on self-assembled monolayer tunnel junctions. *Nat. Photon.* **10**, 274–280 (2016).

[226] Durbin, D. J. & Malardier-Jugroot, C. Review of hydrogen storage techniques for on board vehicle applications. *Int. J. Hydrog. Energy* **38**, 14595–14617 (2013).

[227] Natterer, F. D., Patthey, F. & Brune, H. Distinction of Nuclear Spin States with the Scanning Tunneling Microscope. *Phys. Rev. Lett.* **111**, 175303 (2013).

[228] Natterer, F. D., Patthey, F. & Brune, H. Resonant-Enhanced Spectroscopy of Molecular Rotations with a Scanning Tunneling Microscope. *ACS Nano* **8**, 7099–7105 (2014).

[229] Gupta, J. A., Lutz, C. P., Heinrich, A. J. & Eigler, D. M. Strongly coverage-dependent excitations of adsorbed molecular hydrogen. *Phys. Rev. B* **71** (2005).

[230] Lotze, C., Corso, M., Franke, K. J., von Oppen, F. & Pascual, J. I. Driving a Macroscopic Oscillator with the Stochastic Motion of a Hydrogen Molecule. *Science* **338**, 779–782 (2012).

[231] Li, S. *et al.* Rotational and Vibrational Excitations of a Hydrogen Molecule Trapped within a Nanocavity of Tunable Dimension. *Phys. Rev. Lett.* **111**, 146102 (2013).

[232] Wang, H. *et al.* Trapping and Characterization of a Single Hydrogen Molecule in a Continuously Tunable Nanocavity. *J. Phys. Chem. Lett.* **6**, 3453–3457 (2015).

[233] Yang, K. *et al.* Construction of two-dimensional hydrogen clusters on Au(111) directed by phthalocyanine molecules. *Nano Res.* **7**, 79–84 (2014).

[234] Therrien, A. J. *et al.* Collective effects in physisorbed molecular hydrogen on Ni/Au(111). *Phys. Rev. B* **92**, 161407 (2015).

[235] Natterer, F. D., Patthey, F. & Brune, H. Quantifying residual hydrogen adsorption in low-temperature STMs. *Surf. Sci.* **615**, 80–87 (2013).

[236] Temirov, R., Soubatch, S., Neucheva, O., Lassise, A. C. & Tautz, F. S. A novel method achieving ultra-high geometrical resolution in scanning tunnelling microscopy. *New J. Phys.* **10**, 053012 (2008).

[237] Liu, S., Shiotari, A., Baugh, D., Wolf, M. & Kumagai, T. Enhanced resolution imaging of ultrathin ZnO layers on Ag(111) by multiple hydrogen molecules in a scanning tunneling microscope junction. *Phys. Rev. B* **97**, 195417 (2018).

[238] Schouteden, K. *et al.* Confinement of surface state electrons in self-organized Co islands on Au(111). *New J. Phys.* **10**, 043016 (2008).

[239] Schouteden, K. & Haesendonck, C. V. Narrow Au(111) terraces decorated by self-organized Co nanowires: A low-temperature STM/STS investigation. *J. Phys.: Condens. Matter* **22**, 255504 (2010).

[240] Petersen, L., Laitenberger, P., Lægsgaard, E. & Besenbacher, F. Screening waves from steps and defects on Cu(111) and Au(111) imaged with STM: Contribution from bulk electrons. *Phys. Rev. B* **58**, 7361–7366 (1998).

[241] Ternes, M., Pivetta, M., Patthey, F. & Schneider, W.-D. Creation, electronic properties, disorder, and melting of two-dimensional surface-state-mediated adatom superlattices. *Progress in Surface Science* **85**, 1–27 (2010).

[242] Knorr, N. *et al.* Long-range adsorbate interactions mediated by a two-dimensional electron gas. *Phys. Rev. B* **65**, 115420 (2002).

[243] Tuerhong, R., Kezilebieke, S., Barbara, B. & Bucher, J.-P. Conductance hysteresis and inelastic excitations at hydrogen decorated cerium atoms and clusters in a tunnel junction. *Nano Res.* **9**, 3171–3178 (2016).

[244] Motobayashi, K., Kim, Y., Ueba, H. & Kawai, M. Insight into Action Spectroscopy for Single Molecule Motion and Reactions through Inelastic Electron Tunneling. *Phys. Rev. Lett.* **105**, 076101 (2010).

[245] Mukherjee, S. *et al.* Hot Electrons Do the Impossible: Plasmon-Induced Dissociation of H2 on Au. *Nano Lett.* **13**, 240–247 (2013).

[246] Schendel, V. *et al.* Remotely Controlled Isomer Selective Molecular Switching. *Nano Lett.* **16**, 93–97 (2016).

[247] McNeil, K. J. & Walls, D. F. Possibility of observing enhanced photon bunching from two photon emission. *Phys. Lett. A* **51**, 233–234 (1975).

[248] Horodecki, R., Horodecki, P., Horodecki, M. & Horodecki, K. Quantum entanglement. *Rev. Mod. Phys.* **81**, 865–942 (2009).

[249] Dong, S. *et al.* True Single-Photon Stimulated Four-Wave Mixing. *ACS Photonics* **4**, 746–753 (2017).

[250] Ma, C. *et al.* Silicon photonic entangled photon-pair and heralded single photon generation with CAR > 12,000 and $g^{(2)}(0) < 0.006$. *Opt. Express* **25**, 32995–33006 (2017).

[251] Kwiat, P. G. *et al.* New High-Intensity Source of Polarization-Entangled Photon Pairs. *Phys. Rev. Lett.* **75**, 4337–4341 (1995).

[252] Forgues, J.-C., Lupien, C. & Reulet, B. Emission of Microwave Photon Pairs by a Tunnel Junction. *Phys. Rev. Lett.* **113**, 043602 (2014).

[253] Crampin, S. Lifetimes of Stark-Shifted Image States. *Phys. Rev. Lett.* **95**, 046801 (2005).

[254] Echenique, P. M. & Uranga, M. E. Image potential states at surfaces. *Surf. Sci.* **247**, 125–132 (1991).

[255] Echenique, P. M. *et al.* Decay of electronic excitations at metal surfaces. *Surf. Sci. Rep.* **52**, 219–317 (2004).

[256] Loot, A. & Hizhnyakov, V. Modeling of enhanced spontaneous parametric down-conversion in plasmonic and dielectric structures with realistic waves. *J. Opt.* **20**, 055502 (2018).

[257] Schull, G., Néel, N., Johansson, P. & Berndt, R. Electron-Plasmon and Electron-Electron Interactions at a Single Atom Contact. *Phys. Rev. Lett.* **102** (2009).

[258] Schneider, N. L., Schull, G. & Berndt, R. Optical Probe of Quantum Shot-Noise Reduction at a Single-Atom Contact. *Phys. Rev. Lett.* **105** (2010).

[259] Peters, P.-J. *et al.* Quantum Coherent Multielectron Processes in an Atomic Scale Contact. *Phys. Rev. Lett.* **119**, 066803 (2017).

[260] Willets, K. A. & Van Duyne, R. P. Localized Surface Plasmon Resonance Spectroscopy and Sensing. *Annu. Rev. Phys. Chem.* **58**, 267–297 (2007).

[261] Shi, X., Coca-López, N., Janik, J. & Hartschuh, A. Advances in Tip-Enhanced Near-Field Raman Microscopy Using Nanoantennas. *Chem. Rev.* **117**, 4945–4960 (2017).

[262] Kawata, S., Ichimura, T., Taguchi, A. & Kumamoto, Y. Nano-Raman Scattering Microscopy: Resolution and Enhancement. *Chem. Rev.* **117**, 4983–5001 (2017).

[263] Lee, J. *et al.* Tip-Enhanced Raman Spectromicroscopy of Co(II)-Tetraphenylporphyrin on Au(111): Toward the Chemists' Microscope. *ACS Nano* **11**, 11466–11474 (2017).

[264] Pozzi, E. A. *et al.* Ultrahigh-Vacuum Tip-Enhanced Raman Spectroscopy. *Chem. Rev.* **117**, 4961–4982 (2017).

[265] Weiss, A. & Haran, G. Time-Dependent Single-Molecule Raman Scattering as a Probe of Surface Dynamics. *J. Phys. Chem. B* **105**, 12348–12354 (2001).

[266] Agapov, R. L., Malkovskiy, A. V., Sokolov, A. P. & Foster, M. D. Prolonged Blinking with TERS Probes. *J. Phys. Chem. C* **115**, 8900–8905 (2011).

[267] El-Khoury, P. Z., Hu, D., Apkarian, V. A. & Hess, W. P. Raman Scattering at Plasmonic Junctions Shorted by Conductive Molecular Bridges. *Nano Lett.* **13**, 1858–1861 (2013).

[268] Shiotari, A., Kumagai, T. & Wolf, M. Tip-Enhanced Raman Spectroscopy of Graphene Nanoribbons on Au(111). *J. Phys. Chem. C* **118**, 11806–11812 (2014).

[269] Yazdani, A., Eigler, D. M. & Lang, N. D. Off-Resonance Conduction Through Atomic Wires. *Science* **272**, 1921–1924 (1996).

[270] Limot, L., Kröger, J., Berndt, R., Garcia-Lekue, A. & Hofer, W. A. Atom Transfer and Single-Adatom Contacts. *Phys. Rev. Lett.* **94**, 126102 (2005).

[271] Agraït, N., Yeyati, A. L. & van Ruitenbeek, J. M. Quantum properties of atomic-sized conductors. *Phys. Rep.* **377**, 81–279 (2003).

[272] Cui, L. *et al.* Quantized thermal transport in single-atom junctions. *Science* **355**, 1192–1195 (2017).

[273] Dreher, M. *et al.* Structure and conductance histogram of atomic-sized Au contacts. *Phys. Rev. B* **72**, 075435 (2005).

[274] Rubio-Bollinger, G., Bahn, S. R., Agraït, N., Jacobsen, K. W. & Vieira, S. Mechanical Properties and Formation Mechanisms of a Wire of Single Gold Atoms. *Phys. Rev. Lett.* **87**, 026101 (2001).

[275] Pechou, R., Coratger, R., Ajustron, F. & Beauvillain, J. Cutoff anomalies in light emitted from the tunneling junction of a scanning tunneling microscope in air. *Appl. Phys. Lett.* **72**, 671 (1998).

[276] Schneider, N. L., Johansson, P. & Berndt, R. Hot electron cascades in the scanning tunneling microscope. *Phys. Rev. B* **87**, 045409 (2013).

[277] Ekici, E., Kapitza, P., Bobisch, C. A. & Möller, R. Electron-induced photon emission above the quantum cutoff due to time-energy uncertainty. *Opt. Lett.* **42**, 4585 (2017).

[278] Downes, A., Dumas, P. & Welland, M. E. Measurement of high electron temperatures in single atom metal point contacts by light emission. *Appl. Phys. Lett.* **81**, 1252–1254 (2002).

[279] Hoffmann, G., Berndt, R. & Johansson, P. Two-Electron Photon Emission from Metallic Quantum Wells. *Phys. Rev. Lett.* **90**, 046803 (2003).

[280] Okada, A. *et al.* Anomalous Light Emission from Metal Phthalocyanine Films on Au(111) Activated by Tunneling-Current-Induced Surface Plasmon. *Appl. Phys. Express* **3**, 015201 (2010).

[281] Schneider, N. L., Lü, J. T., Brandbyge, M. & Berndt, R. Light Emission Probing Quantum Shot Noise and Charge Fluctuations at a Biased Molecular Junction. *Phys. Rev. Lett.* **109** (2012).

[282] Buret, M. *et al.* Spontaneous Hot-Electron Light Emission from Electron-Fed Optical Antennas. *Nano Lett.* **15**, 5811–5818 (2015).

[283] Lee, T.-H. & Dickson, R. M. Single-Molecule LEDs from Nanoscale Electroluminescent Junctions. *J. Phys. Chem. B* **107**, 387–7390 (2003).

[284] Xu, F., Holmqvist, C. & Belzig, W. Overbias Light Emission due to Higher-Order Quantum Noise in a Tunnel Junction. *Phys. Rev. Lett.* **113** (2014).

[285] Kaasbjerg, K. & Nitzan, A. Theory of Light Emission from Quantum Noise in Plasmonic Contacts: Above-Threshold Emission from Higher-Order Electron-Plasmon Scattering. *Phys. Rev. Lett.* **114** (2015).

[286] Xu, F., Holmqvist, C., Rastelli, G. & Belzig, W. Dynamical Coulomb blockade theory of plasmon-mediated light emission from a tunnel junction. *Phys. Rev. B* **94**, 245111 (2016).

[287] Lesovik, G. B. Excess quantum noise in 2D ballistic point contacts. *J. Exp. Theor. Phys.* **49**, 592 (1989).

[288] Büttiker, M. Scattering theory of thermal and excess noise in open conductors. *Phys. Rev. Lett.* **65**, 2901–2904 (1990).

[289] Esteban, R., Borisov, A. G., Nordlander, P. & Aizpurua, J. Bridging quantum and classical plasmonics with a quantum-corrected model. *Nat. Commun.* **3**, 825 (2012).

[290] Savage, K. J. *et al.* Revealing the quantum regime in tunnelling plasmonics. *Nature* **491**, 574–577 (2012).

[291] Hohenester, U. Quantum corrected model for plasmonic nanoparticles: A boundary element method implementation. *Phys. Rev. B* **91** (2015).

[292] Esteban, R. *et al.* The Morphology of Narrow Gaps Modifies the Plasmonic Response. *ACS Photonics* **2**, 295–305 (2015).

[293] Zhang, P., Feist, J., Rubio, A., García-González, P. & García-Vidal, F. J. Ab initio nanoplasmonics: The impact of atomic structure. *Phys. Rev. B* **90**, 161407 (2014).

[294] Barbry, M. *et al.* Atomistic Near-Field Nanoplasmonics: Reaching Atomic-Scale Resolution in Nanooptics. *Nano Lett.* **15**, 3410–3419 (2015).

[295] Rossi, T. P., Zugarramurdi, A., Puska, M. J. & Nieminen, R. M. Quantized Evolution of the Plasmonic Response in a Stretched Nanorod. *Phys. Rev. Lett.* **115**, 236804 (2015).

[296] Varas, A., García-González, P., García-Vidal, F. J. & Rubio, A. Anisotropy Effects on the Plasmonic Response of Nanoparticle Dimers. *J. Phys. Chem. Lett.* **6**, 1891–1898 (2015).

[297] Marchesin, F., Koval, P., Barbry, M., Aizpurua, J. & Sánchez-Portal, D. Plasmonic Response of Metallic Nanojunctions Driven by Single Atom Motion: Quantum Transport Revealed in Optics. *ACS Photonics* **3**, 269–277 (2016).

[298] Chen, X. & Jensen, L. Morphology dependent near-field response in atomistic plasmonic nanocavities. *Nanoscale* **10**, 11410–11417 (2018).

[299] Andersen, P. C., Jacobson, M. L. & Rowlen, K. L. Flashy Silver Nanoparticles. *J. Phys. Chem. B* **108**, 2148–2153 (2004).

[300] Parzefall, M. *et al.* Antenna-coupled photon emission from hexagonal boron nitride tunnel junctions. *Nat. Nanotechnol.* **10**, 1058–1063 (2015).

[301] Mikhailova, Y. M., Volkov, P. A. & Fedorov, M. V. Biphoton wave packets in parametric down-conversion: Spectral and temporal structure and degree of entanglement. *Phys. Rev. A* **78**, 062327 (2008).

[302] Clauser, J. F., Horne, M. A., Shimony, A. & Holt, R. A. Proposed Experiment to Test Local Hidden-Variable Theories. *Phys. Rev. Lett.* **23**, 880–884 (1969).

[303] Hong, C. K., Ou, Z. Y. & Mandel, L. Measurement of subpicosecond time intervals between two photons by interference. *Phys. Rev. Lett.* **59**, 2044–2046 (1987).

Acknowledgements

> Aww, this is the greatest nanosecond of my life! No, this one is! No, this one. Wait! That one was... slightly worse. Ah! So far so good on this one!
> — Bender Bending Rodríguez

My PhD studies took 4 years of work and although there were problems to solve and challenges to overcome, this was just a fantastic time of my life. Having already a bit of a perspective I see that during this time I grew not only as a scientist but also as a person. Such a process does not happen in insulation but among people. I was extremely lucky to be surrounded by just the right people and I want to take this opportunity and thank for what you have done for me.

First of all, I would like to thank my thesis director, Prof. Klaus Kern. You accepted me as a PhD student and gave me the opportunity not only to work on this fascinating project but to do it in the outstanding Precision Lab you created. You gave me a lot of freedom, trust and opportunities to develop in many ways. All of that means to me way more than I can express here.

I would like to thank my thesis jury: Prof. Olivier Schneider, Prof. Majed Chergui, Prof. Ernst Meyer and Prof. Sebastian Loth for evaluating my work.

This thesis would not come to live without my daily supervisor, Dr. Klaus Kuhnke. You designed the wonderful *Photon-STM* that gave us a lot of beautiful results. You held my hand at the beginning and gradually let it go, allowing me to explore my ideas, fail and succeed. You have been an excellent teacher of the art and craft of the experiment. You were the most demanding referee, questioning every interpretation of our data I came up with and as your patience has no limit, it brought an understanding after a bunch of iterations. And above all, you are just a great person. *Danke schön!*

I happened to work at the instrument with two amazing postdocs, Dr. Pablo Merino and Dr. Christopher Leon. Pablo, you taught me *how to STM*, helped to design experimental protocols we together realized, structure my ideas and became a good friend. When I was in doubt, you always believed in me and when eventually you left back to Madrid your valuable advice was always accessible within just a few clicks or a phone call. Chris, you taught me to explore the regimes of the experimental phase space nobody has explored before, which brought you to the beautiful discovery of super-bunching, provided a *portal* into the chemist's world and heavily contributed to the improvement of my English. Finally, I'm getting my own *license to speculate!*

I am truly pleased to pass the Photon-STM into the extremely skilled hands of Abhishek Grewal. I always enjoy our long discussions about crazy, more-or-less scientific ideas and when we motivate each other to get better in whatever. I wish you luck, exciting results, a great time at the pink box and a neverending stream of *mango lassi.* For you, the sky is the limit.

I would like to thank Dr. Markus Etzkorn for teaching me everything I know about high frequencies and the everlasting grin on your face. Also, I would like to thank Dr. Christoph Große for showing some hidden, though useful, features of the machine. Special thanks to Dr. Bogdana Borca for the initial introduction to STM and a stream of ideas after an evening coffee.

An experimentalist would not reach far without the support of theoreticians. Thus, I would like to thank Dr. Olle Gunnarsson for the continuous help on our research endeavours. I was always impressed by your understanding of our measurements and how quickly you were able to suggest improvements and provide new ideas. Also, I would like to thank Dr. César González for the calculations on the H_2/Au(111) system.

My time in the Photon-STM group overlapped with visits of two professors who brought a lot of helpful comments and ideas. I would like to thank Prof. Dimas de Oteyza for providing a lot of fun during *heavy-lifting* and Prof. Oğuzhan Gürlü for showing how to do good science with limited resources.

Dr. Guillaume Schull provided valuable insight into the peculiarities of light emission from atomic contacts. *Merci.*

Dr. Manish Garg has been an excellent teacher on ultrafast optics. Your work culture and attitude are deeply inspiring and I try to adapt this approach.

I already mentioned the Precision Lab, which was a fantastic place where I always expected the unexpected thanks to numerous people, especially: Tomasz Michnowicz, Abhishek Grewal, Marcel Pristl, Shai Mangel, Dr. Jacob Senkpiel, Dr. Matthias Muenks, Dr. Christian Dette, Dr. Ivan Pentegov, Tobias Wollandt, Katharina Polyudov and Gennadii Laskin.

I was lucky to be placed in the unforgettable 2W08 office. Our whiteboard was covered with *a pure nonsense* with some Shibas, pulses, cats and graphene in between. Although it was not always an easy place to work in and the headphones were a must, you kept me (in)sane, helped to relax when it was needed and cry laughing when it was necessary. For creating this atmosphere I would like to thank: Tomasz Michnowicz, Abhishek Grewal, Shai Mangel, Dr. Jacob Senkpiel, Marcel Pristl, Dr. Carmen Rubio Verdu, Dr. Christian Dette, Maximilian Uhl, Dr. Ivan Pentegov, Dr. Christoph Große, Dr. Berthold Jaeck and Dr. Verena Schendel.

Apart from the people from our department I have already mentioned, I would like to thank numerous people for all scientific and non-scientific discussions that took place during lunch, coffee breaks and so on: Alessio Scavuzzo, Sven Szilagyi, Piotr Kot, Dr. Sabine Abb, Dr. Diana Hötger, Dr. Robert Drost, Dr. Christian Ast, Prof. Markus Ternes, Prof. Stephan Rauschenbach, Dr. Yuqi Wang, Dr. Bastian Kern, Dr. Peter Jacobson, Dr. Roberto Urcuyo, Dr. Daniel Rosenblatt, Dr. Rico Gutzler, Dr. Sara Barja, Prof. Doris Grumelli, Andreas Topp, Patrick Alexa, Hannah Ochner, Lukas Krumbein, Dr. Sebastian Koslowski, Dr. Lukas Schlipf, Dr. Claudius Morchutt, Dr. Xu Wu, Haonan Huang, Dinesh Pinto, Domenico Paone. Many of you became good friends also outside the work hours.

I would like to thank my fellow PhD representatives, for a year full of fun in a great team: Dr. Pinar Kaya, Rafael Balderas, Dr. Luzia Germann, Werner Dobrautz, Daniel Putzky and Jachym Sykora.

Many people made my way in the Institute as smooth as silk: Sabine Birtel, who is simply an angel, Wolfgang Stiepany, Peter Andler, Marko Memmler, who do miracles right away, the IT department and many more. Also thanks to Anh Eymann for all the help on the EPFL side.

My adventure with physics started in high school. This is why I would like to thank the best teacher I have ever had, Elżbieta Wielińska, for the passion and excitement you managed to transfer to me.

Czas na kilka słów w moim ojczystym języku. Chciałabym bardzo podziękować mojej rodzinie za wsparcie przez całe moje dotychczasowe życie. W szczególności kochanemu Tacie, który zawsze mnie motywował, razem z Mamą, która niestety tych słów nie przeczyta, Irenie, *przyszłej* rodzinie z Mazur i tym których tutaj nie wymieniłam. Wielkie podziękowania dla moich przyjaciół z ukochanego Gdańska, którzy byli w stanie w kilka dni naładować moje baterie na kilka miesięcy pracy w Niemczech.

And finally, someone who has been already mentioned above a few times and is undoubtedly the most important person in this whole endeavour, Tomasz Michnowicz. Thank you for knowing me better than I do, thank you for every dinner that was waiting for me when there was *just one more* measurement to do, thank you for saying the right words in the right moment, thank you for all these lovely little things that make me laugh anytime, thank you for being virtually always as close as the next office desk or box. It was great to understand, lift each other up in the hard times and go through the PhD journey together. I'm more than happy to continue another journey, *our life journey*, by your side.

Stuttgart, February 2019 Anna Rosławska

Curriculum Vitae

Full name	Anna Maria Rosławska
Date of birth	7 September 1990
Nationality	Polish

Education and experience:

2015 -	PhD candidate, Max Planck Institute for Solid State Research, Stuttgart, Germany, Doctoral program in physics, École Polytechnique Fédérale de Lausanne, Lausanne, Switzerland
2013-2014	M.Sc., Nanotechnology, Gdańsk University of Technology, Gdańsk, Poland Master thesis research: Institute of Low Temperature and Structure Research, Polish Academy of Sciences, Wrocław, Poland ERASMUS exchange semester: Chalmers University of Technology, Gothenburg, Sweden grade: excellent
2009-2013	B.Eng., Applied Physics, Gdańsk University of Technology, Gdańsk, Poland Internship: Institute of High Pressure Physics, Polish Academy of Sciences, Warsaw, Poland grade: excellent

List of publications

1. Rosławska, A. *et al.* Four-dimensional imaging of charge dynamics. *in preparation*
2. Rosławska, A. *et al.* Modelling of nanoscale dynamics. *in preparation*
3. Rosławska, A. *et al.* Dynamics of atomic contacts. *in preparation*
4. Leon, C. C.[*], Rosławska, A.[*], Grewal, A., Gunnarsson, O., Kuhnke, K. & Kern, K. Photon super-bunching from a generic tunnel junction. arXiv:1805.10234, *Sci. Adv.* (in press, 2019)
5. Merino, P., Rosławska, A., Leon, C. C., Grewal, A., Große, C., González, C., Kuhnke, K. & Kern, K. A Single Hydrogen Molecule as an Intensity Chopper in an Electrically Driven Plasmonic Nanocavity. *Nano Lett.* **19**, 235-241 (2019)
6. Rosławska, A., Merino, P., Große, C., Leon, C. C., Gunnarsson, O., Etzkorn, M., Kuhnke, K. & Kern, K. Single Charge and Exciton Dynamics Probed by Molecular-Scale-Induced Electroluminescence. *Nano Lett.* **18**, 4001-4007 (2018)
7. Merino, P., Rosławska, A., Große, C., Leon, C. C., Kuhnke, K. & Kern, K. Bimodal exciton-plasmon light sources controlled by local charge carrier injection. *Sci. Adv.* **4**, eaap8349 (2018)
8. Große, C., Merino, P., Rosławska, A., Gunnarsson, O., Kuhnke, K. & Kern, K. Submolecular Electroluminescence Mapping of Organic Semiconductors. *ACS Nano* **11**, 1230-1237 (2017)
9. Kuhnke, K., Große, C., Merino, P., Rosławska, A. & Kern, K. Exzitonen unter dem Mikroskop. *Physik in unserer Zeit* **47**, 6-7 (2016)
10. Merino, P., Große, C., Rosławska, A., Kuhnke, K. & Kern, K. Exciton dynamics of C_{60}-based single-photon emitters explored by Hanbury Brown-Twiss scanning tunnelling microscopy. *Nat. Commun.* **6**, 8461 (2015)

---

[*] Equal contribution

Ce document a été imprimé au Centre d’impression EPFL,
imprimerie climatiquement neutre, certifiée myClimate.